12-15-2014

Slow Wave Structures Integrated with Ferro-Magnetic and Ferro-Electric Thin Films for Smart RF Applications

B M Farid Rahman
University of South Carolina - Columbia

Recommended Citation

Rahman, B. F.(2014). *Slow Wave Structures Integrated with Ferro-Magnetic and Ferro-Electric Thin Films for Smart RF Applications.* (Doctoral dissertation). Retrieved from http://scholarcommons.sc.edu/etd/2937

SLOW WAVE STRUCTURES INTEGRATED WITH FERRO-MAGNETIC AND FERRO-ELECTRIC THIN FILMS FOR SMART RF APPLICATIONS

by

B M Farid Rahman

Bachelor of Science
Bangladesh University of Engineering and Technology, 2008

Master of Engineering
University of South Carolina, 2012

Submitted in Partial Fulfillment of the Requirements

For the Degree of Doctor of Philosophy in

Electrical Engineering

College of Engineering and Computing

University of South Carolina

2014

Accepted by:

Guoan Wang, Major Professor

Tangali S. Sudarshan, Committee Member

Mohammod Ali, Committee Member

Hanqiao Zhang, Committee Member

Lacy Ford, Vice Provost and Dean of Graduate Studies

DEDICATION

Dedicated to my father Md. Atiar Rahman, mother Shamsun Nahar Parul, my lovely wife Shamaita Shithi Shetu and our beloved son Shadhin Rahman for their endless care, encouragement and whole hearted support.

ACKNOWLEDGEMENTS

First of all, I'd like to express my deep appreciation to almighty and many people without whom I couldn't reach to this point of my life. I'd like to thank my advisor Dr. Guoan Wang for accepting me as a student at one of the most critical moments of my life. I appreciate all his time, ideas, and funding to make my Ph. D. experience productive and stimulating. The joy and enthusiasm he has for scientific findings was contagious and motivational for me even during tough times in the Ph.D. pursuit. His door was always open for us for any advice or support and he always encouraged me to think in a broader picture. I will highly miss the conversations with him about the carrier, opportunities and beyond. He has given me the opportunity to work in collaboration with Argonne National Lab and IBM Corporation which was very valuable for my PhD experience. I simply could not wish for a better or friendlier supervisor.

I would like to thank Prof. Tangali S. Sudarshan, Prof. Mohammod Ali, and Dr. Hanqiao Zhang for serving in my Ph.D. committee and managing their precious time and for all the insightful comments and suggestions to make the dissertation a success. It was my great privilege to get Prof. Tangali S. Sudarshan as one of my mentors. I am grateful to him for allowing me to use his very well equipped laboratory throughout my PhD life. I would like to thank my lab mate Yujia Peng, Tengxing Wang and Sam Wang for their continuous and selfless support throughout my PhD life.

I would like to thank Dr. Ralu Divan, a scientist of Argonne National Lab for teaching me the fundamentals of nano fabrication so precisely and taking so much time to help me finish my work. She contacted with anyone possible to help my project. I do appreciate the days she used to arrive in the weekend so that I can accelerate my work. I would like to thank Daniel Rosenmann, Liliana Stan and Leonardo Ocola for all the helps they provided during my Argonne days. I would like thank Essam Mina from IBM Corporation for working in collaboration with me based on which I filed the first patent of my life.

I would like to remember my father Md. Atiar Rahman and my mother Shamsun Nahar Parul for raising me up since my childhood with so much care and love. They were a continuous support for me and more anxious than me for any steps or exams I have taken in my life. I can’t think of to be here without them. I would like thank my elder sister Julfia Parvin Jaba and my brother in law Ismail Hossain for remaining as my guardian throughout my USA life. They came up with help for so many occasions during our good or bad time. I would like to thank my younger sister Zakia Parvin Lima and her husband Kamruzzaman Morol for their love and care since my childhood. I would like thank my father in law Md. Shahid Ullah Bhuiyan and my mother in law Nurjahan Begum for their care and mental support throughout my PhD life.

I would like to remember my loving, supportive, encouraging and patient wife Shamaita Shithi Shetu whose faithful support during the long journey of my Ph.D. is highly appreciated. When I was about to quit after two years of my enrollment, its only she who made me believe I can complete my PhD and helped me with all possible ways to finish my work. I would like to appreciate her lonely struggle with my son during my

Argonne days. I would like to thank her for hard work and mental support to live through our tough days. Finally, I would like to thank the newest addition to my family, my three years old son, Shadhin Rahman. His laugh, running towards me, hug, play time with me were great sources of inspiration to me. I will never forget his excitement while we used to go his day care to pick him up. I would like thank him for so many sacrifices he had to make to help his parents complete their PhD. We would like to live many more days just because of him. Completing my Ph.D. is certainly the finishing of one memorable chapter in my life, but I believe, a new challenging and more rewarding phase are still waiting.

B M Farid Rahman

August 20, 2014

ABSTRACT

Modern communications systems are following a common trend to increase the operational frequency, level of integration and number of frequency bands. Although 90-95% components in a cell phone are passives which take 80% of the total board area. High performance RF passive components play limited role and are desired towards this technological advancement. Slow wave structure is one of the most promising candidates to design compact RF and mm-Wave passive components. Slow wave structures are the specially designed transmission line realized by placing the alternate narrow and wide signal conductors in order to reduce the physical size of the components. This dissertation reports multiband slow wave structures integrated with ferromagnetic and ferroelectric thin films and their RF applications.

A comparative study on different types of coplanar wave-guide (CPW) slow wave structures (SWS) has been demonstrated for the first time. Slow wave structures with various shapes have been investigated and optimized with various signal conductor shapes, ground conductor shapes and pitch of the sections. Novel techniques i.e. the use of the defected ground structure and the different signal conductor length has been implemented to achieve higher slow wave effect with minimum loss. The measured results have shown the reduction of size over 43.47% and 37.54% in the expense of only 0.27dB and 0.102dB insertion loss respectively which can reduce the area of a designed branch line coupler by 68% and 61% accordingly.

Permalloy (Py) is patterned on top of the developed SWS for the first time to further increase the slow wave effect and provide tunable inductance value. High frequency applications of Py are limited by its ferro-magnetic resonance frequency since the inductance value decreases beyond that. Sub-micrometer patterning of Py has increased FMR frequency until 6.3GHz and 3.2GHz by introducing the shape anisotropy. For the SWS with patterned Py, the size of the quarter wavelength has been reduced from 14.86mm to 4.7mm at 2GHz. DC current which is the most convenient and available tuning parameter in a practical circuit board has been used, the developed SWS can function as quarter wave transmission line from 2GHz to 1.80GHz (i.e. 10%).

Lead Zirconium Titanate (PZT) is grown and patterned on top of the section with standard sol-gel method to increase capacitance value. The inter digit capacitor type structure along with PZT thin film has been adopted and results showed capacitance value increment by 36%. An electric field between signal and ground has been applied to change the polarization of the thin film which resulted in a tuning of center frequency by 15% (1.75GHz to 2GHz). In addition, a novel approach has been implemented by integrating both the ferromagnetic and the ferroelectric thin films simultaneously to achieve higher slow wave effect, wider tuning range and smaller variation in Characteristics Impedance. The size of the final structure for a quarter wavelengths has been reduced from 14.86mm to 3.98mm while the center frequency has been tuned from 2GHz to 1.5GHz (i.e. 25%).

Tunable RF applications of the ferro-magnetic thin films are also demonstrated as a DC current band pass filter, tunable noise suppressor and meander line inductor. A well designed frequency tunable band pass filter (BPF) is implemented at 4GHz with

patterned Permalloy. The pass band frequency of a band pass filter has been tuned from 4GHz to 4.02GHz by applying a DC current. The suppression frequency of the developed noise suppressor is tuned from 4.8GHz to 6GHz and 4GHz to 6GHz by changing the aspect ratio of the Py bars and the gap in between them. Moreover, a novel way of tuning the stop band frequency of the noise suppressor by using an external direct current changed the suppression frequency from 6GHz to 4.3GHz. A pass band loss of 1.5%, less than 2° transmitted signal phase distortion, and 3 dB extra return loss of the designed noise suppressor showed the promise the noise suppressors. The increase in the number of turns of a meander line inductor has increased the inductance density from 2565nH/m to 3396nH/m while application of the patterned Py has increased the inductance density from 2565nH/m to 3060nH/m. The tuning of the meander line inductor has been performed by applying DC current until the FMR frequency 4.51GHz.

TABLE OF CONTENTS

LIST OF TABLES

LIST OF FIGURES

LIST OF ABBREVIATIONS

CPW	Coplanar Wave Guide
DC	Direct Current
FMR	Ferro Magnetic Resonance
PY	Permalloy
PZT	Lead Zirconium Titanate
SWS	Slow Wave Structure
VNA	Vector Network Analyzer

CHAPTER 1

INTRODUCTION

The hand-held wireless devices emerge as the most promising next generation electronics. Modern wireless communication technology is following a common trend to increase the operational frequency, degree of integration and multi-functionality. Rapid growth in mobile computing is inspiring for even higher speed data services [1]. High frequency operation has the advantages of high data transfer speed, reduced size and more number of allowable channels for a particular frequency band. The gain and directivity of the transmission antenna of the same size are higher at higher frequency.

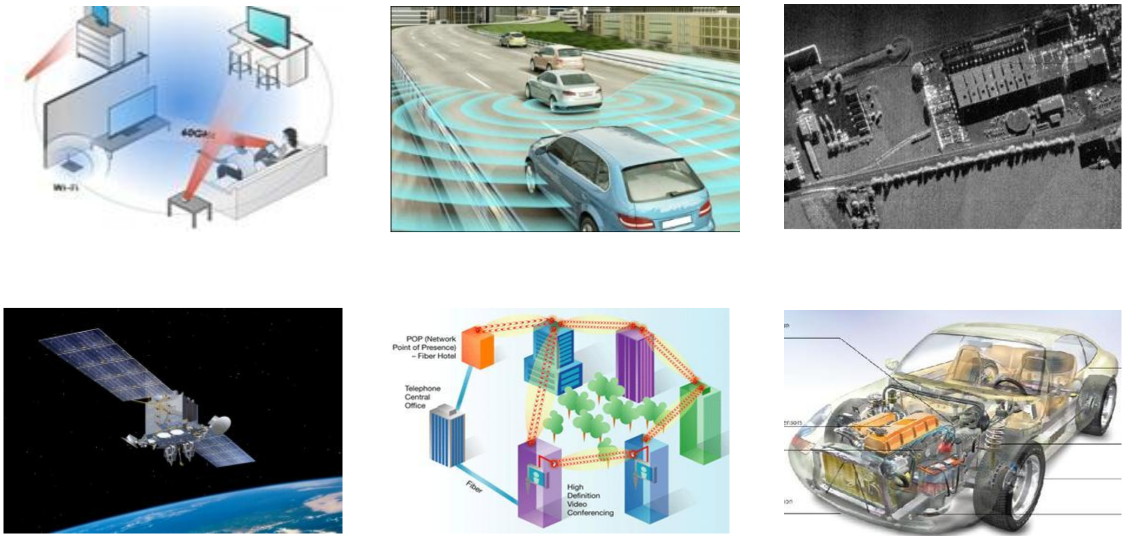

Figure 1.1: High frequency applications of modern communication technology. [123-128]

Most recently wireless communications at high frequency have been developed to enable multi-Gbps wireless communication. Figure 1.1 summarizes applications of 60GHz wireless local area network, 77GHz adaptive cruise control radar, E-band (71-88 81-86, 92-95GHz) point-to-point local area communication link, 94GHz radar imaging, 2.4GHz wireless sensors in automobile, space and military applications.

In a practical wireless system circuit board, a large portion of space is taken by the passive components like high-Q inductors, capacitors, varactors, ceramic filters, matching networks, LC tank circuits (in VCOs), attenuators, power dividers, switches, de-couplers, reference resonators etc. For example, 90–95% of the components in a cell phone are passives which take up to 80% of the total transceiver board area, and costs for 70% of the total amount [1]. Figure 1.2 shows a 2.4GHz transceiver board where large amount of passive components like matching stubs, resistors, capacitors, bends, couplers, power dividers have been identified.

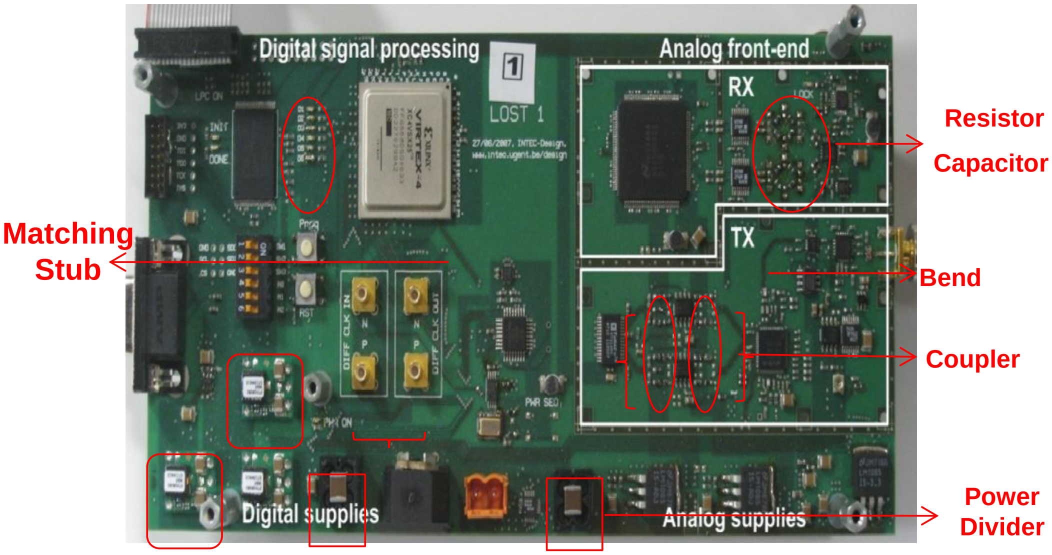

Figure 1.2: 2.4GHz transceiver board showing some of the passive components. [129]

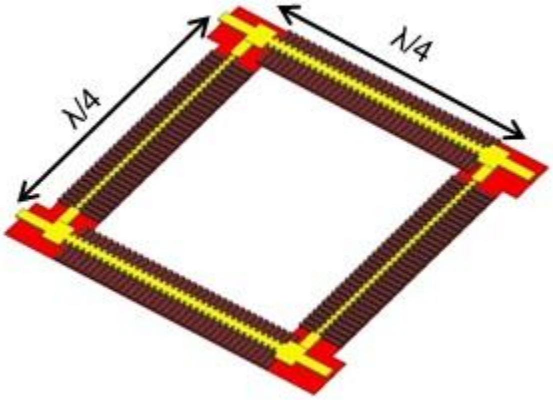

Figure 1.3: Branchline Coupler with four arms where each of them is creating 90^0 phase shift. [7]

Reducing size of the passive components is a key factor in decreasing the cost and size of modern and future wireless devices. The reduction of the space taken up by the passives had been achieved using very small discrete passive components, integrating passive components (either on-chip or off-chip) [2, 3, 4] or implementing novel transceiver architectures in which fewer passives are needed [5, 6]. In this dissertation several novel transmission line solutions to decrease the size of the passive components have been investigated. Small passive components can be designed and implemented with the demonstrated solutions to further decrease the required size of the board area.

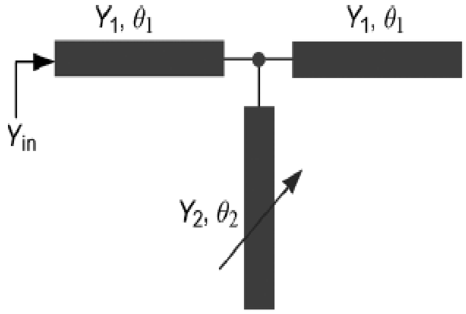

Figure 1.4: Dual band pass filter using defected ground structure and band pass filter using resonator. [131]

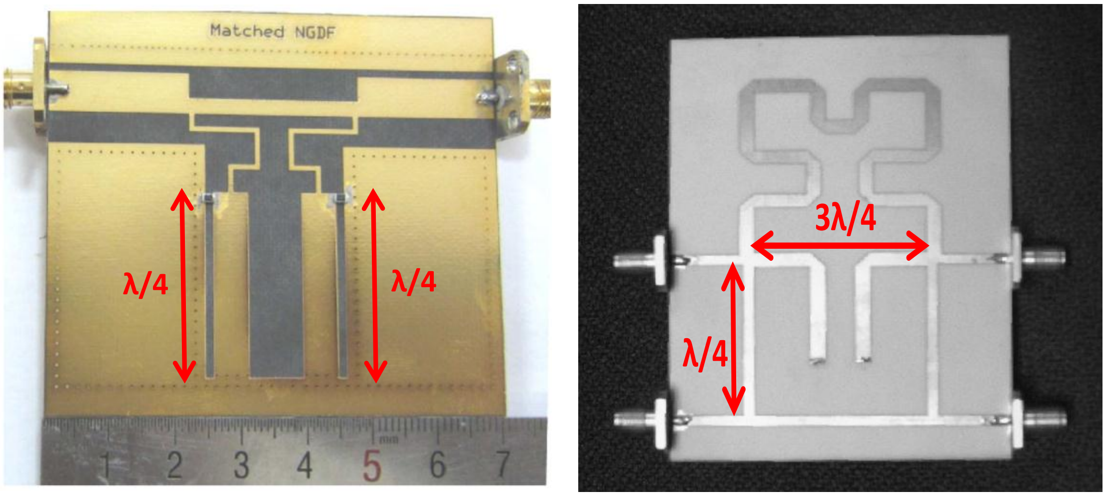

Figure 1.5: Microstrip Line negative group delay filter and rat race coupler. [18, 20]

Transmission line is a key element in designing RF passive components. Passive components largely consist of either one or multiple sections of transmission lines whose length are directly dependent on wavelength. Branch Line Coupler as one of the important passive components [7-12] is a four-port network device with a 90° phase difference between two coupled ports. This device has been widely used in a single antenna Transmitter/Receiver system or signal splitter/combiner. Figure 1.3 shows an image of a Branchline Coupler where each arm constitutes of a transmission line creating a 90^{o} delay i.e. the size of each section is dependent on wavelength or electrical length. Band pass filters have been largely reported using microstrip $\frac{\lambda}{4}$ resonators with open stub inverter [13], using defected ground structure with wide stop band performance [14] and using pseudo-inter digital stepped impedance resonators for WLANs [15]. Filters have demonstrated the idea of using stepped-impedance resonators with new coupling schemes [16], stub-loaded resonators [17] and microstrip negative group delay [18] also. These filters all have one or multiple transmission line sections whose physical sizes depend on the electrical length or the wave length. Rat race coupler is another type of coupler which

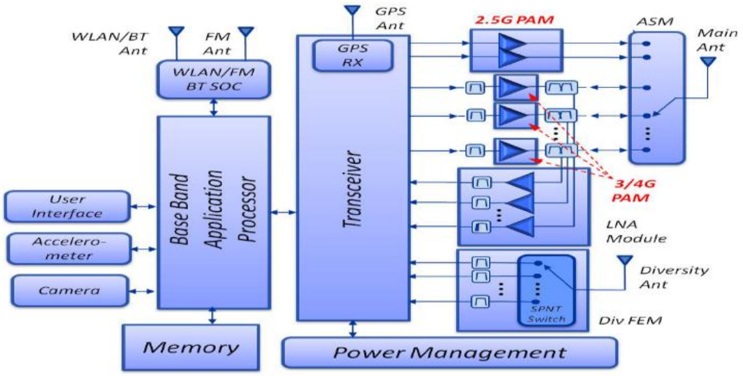

Figure 1.6: Smart mobile phone block diagram based on discrete multiband power amplifier. [38]

is used to sum two in-phase combined signals with essentially no loss or to equally split an input signal with no resultant phase difference between its outputs. Different types of rat race couplers [19-24] primarily consist of four sections: length of the three sections is $\lambda/4$ and the other section is $3\lambda/4$.

Slow wave structure is a specially designed transmission line intended for increasing the inductance and capacitance per unit length thereby decreasing the wavelength which ends up in smaller physical size compared to regular transmission line. A well designed slow wave structure reduces the size of the component while keep the insertion loss as low as possible. Various types of slow wave structures with CMOS fabrication technology [25], discontinuous microstrip lines, multi-layer ground [7] and 3-D steps [26] have been reported so far but they contributed higher insertion loss due to the increased mismatch. To improve the loss, cross-tie periodic structure [27] and homogenously doped semiconductor structure [28] have been demonstrated which generate fabrication issue. Filter applications has used coplanar waveguide SWS with arms [29] and microstrip lines utilized the alternate of a wide and a narrow line in turn to realize SWS [30]. SWSs using inductive and capacitive loaded line [31] as well as

Figure 1.7: Multiband Coupler using 30-180MHz, 330-520MHz and 746MHz-1.3GHz and GPS Antenna using GSM 850, 900, 1800, 1900, 3G, Wi-Fi/WiMAX. [39, 40]

positively and negatively tapered sections [32] have also shown promising results. However, current SWS has limited slow wave effect and fixed operation frequency.

The first goal of this dissertation is to develop transmission line with smaller wavelength using slow wave structure (SWS) which is one of the most promising ways to achieve size reduction of passive components. In this dissertation, novel low loss slow wave structures having different shapes are analyzed and optimized to achieve high slow wave effects. A throughout comparative study considering both signal and ground conductor shape and dimensions are presented in Chapter 2. The methods of using the defected ground structure along with the different section lengths are used for the first time in order to achieve compact SWS with reasonable loss [33].

The growth of mobile internet and multimedia services like video teleconference, social network, mobile video games, web browsing, music download, movie streaming, and broadcast television is tremendous in recent days [34]. A lot of advanced mobile devices including smart phones, netbooks, tablet PCs and data cards have been developed for these purposes. Apart from the enriched features and services available for the users, these mobile devices are required to support higher data rates promised by 3G WCDMA/HSPA, and 4G LTE standards with a backward compatibility to the 2G GSM and 2.5G GPRS/EDGE standards. A combination of frequency bands will have to be supported to reduce the cost and size of the mobile devices [35]. Consequently, the increase in complexity of the mobile devices translates into greater challenges and more stringent requirements on the design of front end passive components, including filters, switches and power amplifiers (PA) [36, 37, 38]. Frequency-agile and multifunctional circuits are highly desirable in communications systems, radars, sensor networks, and biomedical devices also. Tunable elements are the key components in achieving the frequency tunability. Great efforts have been made on developing tunable components such as antennas, filters, matching networks, couplers, dividers and phase shifter etc. Though various tuning techniques have been utilized in achieving frequency tunability including semiconductor varactors [41]-[43], ferroelectric thin films [44]-[46], and RF MEMS [47], [48], those techniques can achieve a reasonable capacitance tuning capability only. The Amorphous ferromagnetic wires have demonstrated the tuning of transmission characteristics by DC current based on giant magneto impedance effect [49-51]. Ferromagnetic thin films have also been actively explored for high-performance microwave devices. RF devices have been done using yttrium iron- garnet (YIG) [52-53] and tuned with external magnetic field but these are difficult to integrate with planar RF/microwave circuit.

Numerous research has been carried out to develop magnetic thin films for high frequency devices, such as inductors [134-141], transformers [142], noise suppressors [57, 59-61], magneto-resistive memory devices [143-144] etc. Different types of soft ferro-magnetic materials like CoPdAlO, CoZrO, CoNbZr, Fe, and CoFeAlO have been used for these purposes. As a ferromagnetic thin film, Permalloy (Py) has high and electrical tunable permeability, low resistivity as well as no stress anisotropy [54-55]; it has been studied in tunable microwave devices with increased and tunable inductance density. Slow wave components [33,70], tunable inductors [64-67] and resonators [68-69] based on permalloy (Py) thin film is becoming very popular due to their low loss, high tuning capability and available for high frequency applications. However, RF applications of Permalloy are highly dependent on its ferro-magnetic resonance (FMR) frequency and inductance density as the inductance value falls below zero and not predictable after that frequency. The ferromagnetic resonance (FMR) frequency of the studied un-patterned Py films falls into the sub-GHz range. However, effective patterning of Py can provide a compromise solution in achieving high FMR frequency with reasonable increment of inductance density. Magnetic properties [71-73] of Py thin film have been investigated. But the analysis of Py thin film properties for the application at microwave and RF components has not been fully studied yet. This dissertation provides a first comprehensive experimental RF study of patterned Py thin film with various dimensions.

The strategy used in this dissertation is to increase the shape anisotropy field of the ferromagnetic materials which in turn increases the FMR frequency while the loss introduced by the Py film is kept to a minimum. Properly patterned ferromagnetic thin films have built-in high shape anisotropy fields and, therefore, provide a self-biasing for high-frequency applications. Micro patterning of ferromagnetic thin film has increased the FMR frequency to 1.3GHz [56]. Py thin film has been patterned in nano-scale range to increase the FMR frequency to 6.3GHz while keeping the loss of the transmission line at a minimum level by reducing the eddy current through it. Micro-patterning of thicker layer of Py showed an FMR frequency of 3.2GHz but the inductance increment has been achieved by a big margin.

Further application of the external magnetic field can take frequency of FMR at higher frequency. Tunability of FMR frequency has been investigated using DC current. Tuning of frequency using DC current has the advantages over applying the external magnetic field as that in previously reports [57, 58]. Both Ampere's fields and Joule heating effects due to the applied DC current contribute to the shift of FMR [59], thus less ampere field is needed for the same amount of FMR shift.

High permittivity value and loss of the ferro-electric thin films has shown the promise to be used at high frequency devices [145]. Different properties of ferro-electric thin films have been utilized to demonstrate their applications in various fields. Polarization reversal and properties related to the reliability of Ferroelectric memories and microsystems' applications have been demonstrated based on the properties of polarization reversal and piezoelectric nonlinearity. In order to increase and tune the capacitance, ferro-electric thin film, Lead Zirconium Titanate (PZT) has been studied in this dissertation. Lead Zirconium Titanate (PZT) has very high dielectric constant near DC as well as its electric polarization is tunable with the application of an electric field. PZT was grown in an efficient, low cost and easily available system i.e. sol-gel method. Polycrystalline structure with a preferred orientation of the thin film has been achieved after the optimization of the growth techniques. A DC voltage has been applied on the well-designed tunable slow wave structure to change the property of the PZT to achieve tunable capacitance value.

A concept of tunable slow wave structure enabled with both nano-patterned ferromagnetic (Permalloy: Py) and ferroelectric (Lead zirconium Titanate: PZT) thin films is presented for the first time in this dissertation. The permittivity (ε_r) of PZT is electrical tunable with DC voltage, and the permeability (μ_r) of Permalloy is electrical tunable with applied DC current, thus simultaneous electric tunable capacitance and inductance capability are provided for the proposed SWSs. It can be used to design various compact multi-band RF passives with reduced size, wide continuous tunable frequency, high linearity, and low signal loss.

In this dissertation, the ferro-magnetic thin film has been further utilized in RF passive components such as noise suppressors, band pass filters and meander line inductors as shown in Chapter 5. Multiband band pass filters (BPFs) are highly needed to handle different frequency bands and reduce the system size and complexity in rapidly developing modern microwave wireless communication systems. Various approaches have been studied and applied to achieve the frequency tunability of BPFs, such as micro-electro-mechanical-systems [74], yttrium iron garnet [75], varactors [76-78], piezoelectric transducers [79] and p-i-n diodes [80] etc. However, micro-electro-mechanical-systems technology will significantly increase the difficulty of fabrication and there are still some fabrication and integration issues. Varactors and p-i-n diodes can achieve the tunability by utilizing capacitance tuning. Piezoelectric transducer is a kind of electromechanical method to achieve the tunability. However, those methods introduce some extra devices, which will significantly increase the size of BPFs and the complexity of fabrication. Yttrium iron garnet is an attractive magnetic material for application in microwave tunable devices, but external magnetic bias field is needed. This dissertation provides a first frequency tunable BPF at 4GHz based on the application of patterned Permalloy (Py) thin film. With only patterned Py thin film deposited on the top of the resonators of the BPF, no extra area and devices is introduced, thus the BPF structure is more compact. The BPF is well designed and DC current can go through from the input to the output so that the center frequency can be tuned with only DC current.

The electromagnetic noise at gigahertz range has been suppressed by the ferromagnetic thin film resonance. Noise suppressors using plain CoPdAlO, CoZrO, CoNbZr [59, 60, and 61] films and Py nano-rod arrays [62] on CPW have been reported earlier. Magnetic composite sheets [63] on microstrip transmission line have been used to suppress noise. CoFeAlO [57] films on top of CPW structure demonstrated LC resonance to attenuate the noise. Furthermore, tunable microstrip structure along with nickel nano-rod arrays and Py film demonstrated noise suppression using an external magnetic field [58]. Here, a novel electrical tunable noise suppressor has been reported using nano patterned Py thin film and tuned by external DC current. It ensures good pass band characteristics, minimum reflection criterion and low differential phase shift as well.

Planar inductors have the applications in MEMS actuators [81], RF ID [82], slow wave structures [33, 70] and different passive components. Researchers are trying to miniaturize the inductive component [83]–[86] as it occupies a large space. Active inductive component [8] by simulating the electrical properties of an inductor achieved very high Q-factor and inductance in a relatively small size with this approach. However, this approach suffers from high power consumption and high noise levels. Among the integrated inductors meander-types or spiral-types [83], [87] are very common, whereas most of the macro-scale inductors are solenoid-types. The solenoid-type geometry has a limitation of micro-fabrication techniques as the coil wrapped around a core is been more difficult using conventional IC processes than the fabrication of meander or spiral-types. Though a spiral type inductor has a relatively high inductance value, it needs a lead wire to connect from the inside end of the coil to the outside. This produces an unnecessary capacitance between the conductor and the lead wire which is very dominant [87-88]. Moreover, it can interfere with the underlying circuit in multichip modules as the direction of flux is perpendicular to the substrate. A meander-type inductor is simple to fabricate and integrate into a big system. A study on meander line inductor has been performed and the patterned ferro magnetic thin film has been applied on top of meander line inductors to increase as well as to tune the inductance density.

In this dissertation, the slow wave structures have been developed and optimized to reduce the size of the various passive components. The slow wave effect is further improved by using the ferro-magnetic and ferro-electric thin films. The structures are also made to work at higher frequencies as well as multiple frequencies by the proper design of the thin films as well as the slow wave structures. The thin films have been integrated on the radio frequency passive components like noise suppressors, filters and meander line inductors.

In Chapter-2, the fundamentals of slow wave structures have been investigated to show the principles of size reduction with t slow wave techniques. Extra losses due to the introduction of slow wave structures have been fully studied and optimized as well as the design and fabrication of the SWS has been followed by the characterizing method. The slow wave structures with various shapes have been demonstrated and the most promising structures have been further optimized to achieve higher slow wave effect with reasonable loss.

In Chapter-3, the ferro-magnetic thin film has been introduced on the slow wave structures to further increase the inductance density and frequency tunable. The necessity of using the ferro-magnetic thin film has been discussed followed by the shortcomings of the ferro-magnetic thin film at radio frequency components. The growth of the ferro-magnetic thin film, Permalloy by DC magnetron sputtering has been discussed. The patterned ferro-magnetic thin film has been implemented on top of the optimized slow wave structures and the measured results showed the inductance increment, reduction of size and tunability in terms of frequency.

In Chapter-4, the ferro-electric thin film has been introduced to improve the slow wave effect by increasing the capacitance density. The necessities and background of the ferro-electric thin film has been described followed by the growth of the ferro-electric thin film which had several issues for co-planar devices. The problems have been addressed to increase the capacitance value by a big margin in a wide range of frequency band. The ferro-electric thin film has been used in a “inter digit capacitor” integrated slow wave structure and the measured results have shown improvement of the slow wave effect as well as the tuning of the operational frequency by a wide range. The ferro-magnetic and ferro-electric thin films have been integrated simultaneously as the ferro-magnetic thin film increases the inductance and the ferro-electric thin film increases the capacitance i.e. the characteristics impedance remains almost same for the structure which is a very important criterion. The measured results have shown the wider tuning range as well as very high slow wave effect.

In Chapter-5, the concept of using the thin films have been implemented on the RF passive components. A comprehensive study has been performed on the patterned Py for evaluating its application on different RF components. A tunable noise suppressor has been presented to absorb the electromagnetic noise of the system and compared with different type of noise suppressors. The suppression peak of the noise suppressor has been changed by using the different type of patterns and the DC current. The ferro-magnetic thin film has been implemented on the meander line inductor to increase as well as tune the inductance density. A tunable band pass filter has been fabricated with both the ferro-magnetic and ferro-electric thin film to show the change of pass band by the application of DC current. In chapter-6, the dissertation has been concluded with a summary, contributions as well as the prospect of the slow wave structures in various radio frequency applications. The future works to be performed in order to improve the performance of the devices is discussed.

CHAPTER 2

SLOW WAVE STRUCTURE

In this chapter, fundamentals of the slow wave structures i.e. the way in which the inductance and capacitance per unit length are increased to reduce the velocity of propagation have been fully investigated. The extra insertion loss due to the slow wave effects has been simulated and measured. SWSs are optimized with better slow wave effect while maintaining the insertion loss at a minimum. The first step towards this optimization is designing various shapes of the signal conductor in the SWS and the results are compared with a regular non-slow wave structure. The defected ground structure which showed the most promising results are further optimized by changing the gap between the ground conductors along the narrow signal section, the width of the wide conductor section and the pitch of different sections. Different lengths of narrow and wide conductor sections are utilized to provide more flexibility on achieving different characteristics impedance.

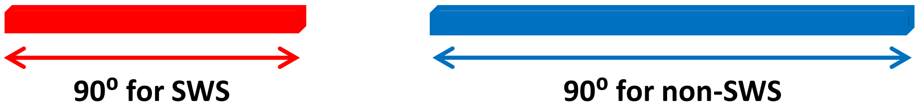

Figure: 2.1 Comparison of the physical length of a regular structure and slow wave structure for the same electrical length.

All the techniques are combined in this dissertation to achieve higher slow effect while keeping the loss at a minimum. This chapter provides a first comprehensive study of various slow wave structures.

2.1 FUNDAMENTALS OF SLOW WAVE STRUCTURES

Slow wave structure is a type of particularly designed transmission line which is smaller in physical length with the same electrical length when compared with a regular transmission line. According to transmission line theory, the wavelength, phase velocity and characteristics impedance are defined from equations (2.1)-(2.3) [89]. The assumption of the simplified transmission theory is valid in the case where both the conductor and dielectric losses are low which can be achieved by optimized design of the component and properly selection of the substrate.

$$Wave\ Length,\ \lambda = \frac{v}{f} \tag{2.1}$$

$$Phase\ Velocity,\ v = \frac{1}{\sqrt{LC}} \tag{2.2}$$

$$Characteristics\ Impedance, Z_0 = \sqrt{\frac{L}{C}} \tag{2.3}$$

Where, the L stands for Inductance per unit length (unit nH/m) and C stands for Capacitance per unit length (unit nF/m). The increment of the L and C value results in lower phase velocity of the signal propagation from equation 2.2. The smaller phase velocity results in smaller electrical wavelength as shown in equation 2.1. The physical length required to achieve a particular phase shift is smaller in a SWS compared to a regular structure. As the propagating signal takes the same time to reach a particular electrical length or delay, the velocity of the signal propagation which is defined by the physical distance traveled in a particular time is smaller in a slow wave structure as clarified in Figure 2.1. Passive components largely consist of either one or multiple sections of transmission lines whose length are fraction of wavelength, thus the physical size of the components based on slow wave structures can be dramatically reduced.

Wireless communication systems consist of many components where each is designed for a specific task. All the components are connected in a sequence to perform a combined task, it is very important to maintain impedance matching in the system. Radio frequency devices are normally designed with 50Ω characteristic impedance, it is critical to keep the characteristics impedance of components the same (e.g., 50Ω) to reduce the mismatch loss from nearby connecting components. The increase of inductance (L) and capacitance (C) with the same ratio using suitable design of SWS can keep the characteristics impedance the same.

In this dissertation, SWSs are realized with an alternated narrow and wide conductor sections as shown in Figure 2.2. The narrow signal conductor sections increase the inductance value with higher distance from the ground while wide conductor sections

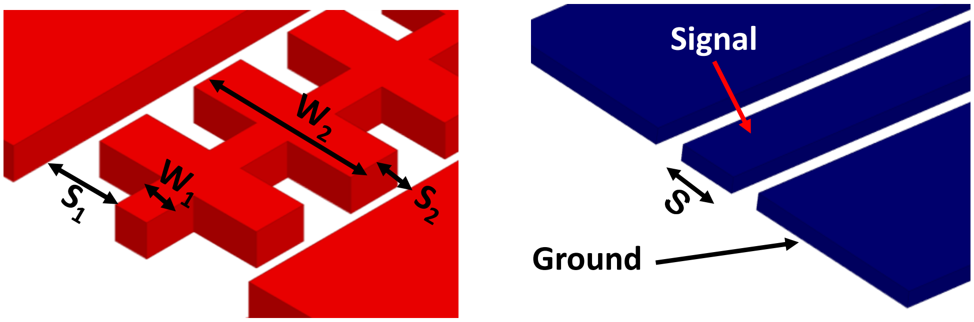

Figure: 2.2 Structures of (a) regular structure and (b) SWS.

increase the capacitance value from smaller distance between signal and ground. The capacitance per unit length, effective dielectric constant and the characteristics Impedance of the co-planar waveguide structure are defined in equations below [90].

$$Capacitance, C_{CPW} = 2\varepsilon_0(\varepsilon_{r1} - 1)\frac{K(k_1)}{K(k_1{}')} + 4\varepsilon_0\frac{K(k_0)}{K(k_0{}')} \quad 2.4$$

$$k_1 = \frac{sinh(\frac{\pi S}{4h_1})}{sinh\{\frac{[\pi(S+2W)]}{4h_1}\}} \quad 2.5$$

$$k_1{}' = \sqrt{1 - k_1{}^2} \quad 2.6$$

$$k_0 = \frac{S}{S+2W} \quad 2.7$$

$$k_0{}' = \sqrt{1 - k_0{}^2} \quad 2.8$$

$$Effective\ Dielectric\ Constant, \varepsilon_{eff} = 1 + \frac{(\varepsilon_{r1}-1)}{2}\frac{K(k_1)}{K(k_1{}')}\frac{K(k_0)}{K(k_0{}')} \quad 2.9$$

$$Characteristics\ Impedance, Z_0 = \frac{30\pi}{\sqrt{\varepsilon_{eff}}}\frac{K(k_0{}')}{K(k_0)} \quad 2.10$$

Wherek_1,$k_1{}'$, k_0 and $k_0{}'$are the moduli of complete elliptic integral.

S is the width of the signal conductor

W is the gap in between signal and ground conductor.

h_1 is height of the substrate.

ε_{r1} is the real dielectric constant of the substrate.

The increment of L and C value at the same rate decreases the size keeping the same characteristics impedance. However, the insertion loss of SWS increases due to the change of the signal and ground conductor shapes, the SWSs need to be fully optimized to keep the loss at a minimum.

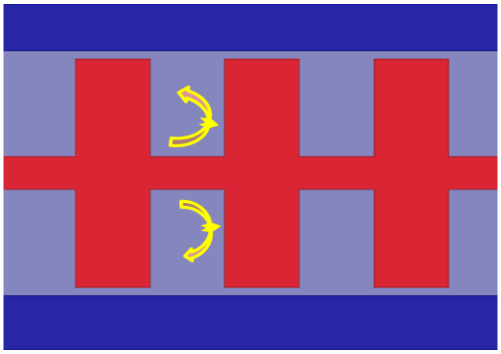

Figure 2.3: Signal reflection from each section contributes to insertion loss.

2.2 LOSS OF SLOW WAVE STRUCTURES

The loss per unit length of a transmission line constitutes of the mismatch loss and attenuation loss. SWSs compose many narrow and wide conductor sections, thus the signal will be reflected from each section as shown in Figure 2.3. The reflection coefficient and the reflection loss are defined by equation 2.11 and 2.12 [89] when the impedance of the narrow section is Z_1 and the impedance of the wide section is Z_2. The total mismatch loss will be the summation of the mismatch loss of each section in the SWS.

$$Reflection\ Coefficient, \Gamma = \frac{Z_2 - Z_1}{Z_2 + Z_1} \qquad 2.11$$

$$Return\ Loss, P_{RL} = -20\, log|\Gamma|\, dB \qquad 2.12$$

The attenuation loss is dependent on the signal conductor resistance, ground conductor resistance and skin effect as shown in equation 2.14-2.19 [89]. The signal and the ground conductor resistance increase with the change of the shape in case of a slow wave structure i.e. the attenuation losses are higher for SWS. High resistivity (10KΩ-cm) Silicon substrate has been chosen to decrease the substrate loss in this dissertation. The dielectric loss is considered to be the same for both slow wave and non-slow wave structure as the same substrate is used.

$$Total\ attenuation, \alpha = \alpha_c + \alpha_d \frac{Neper}{meter} \tag{2.13}$$

$$Attenuation\ due\ to\ conductor, \alpha_c = \frac{R_c + R_g}{2Z_0}\ Neper/meter \tag{2.14}$$

$$Attenuation\ due\ to\ dielectric, \alpha_d = \frac{\pi}{\lambda_0}\frac{\varepsilon_r}{\sqrt{\varepsilon_{eff}}} q \tan\delta_e\ Nepers/meter \tag{2.15}$$

$$Resistance\ of\ signal, R_c = \frac{R_s}{4S(1-{k_0}^2)K^2(k_0)}\left[\pi + \ln\left(\frac{4\pi S}{t}\right) - k_0 \ln\left(\frac{1+k_0}{1-k_0}\right)\right]\frac{\Omega}{m} \tag{2.16}$$

$$Resistance\ of\ ground, R_g = \frac{k_0 R_s}{4S(1-{k_0}^2)K^2(k_0)}\left[\pi + \ln\left(\frac{4\pi(S+2W)}{t}\right) - k_0 \ln\left(\frac{1+k_0}{1-k_0}\right)\right]\frac{\Omega}{m} \tag{2.17}$$

$$Skin\ Effect\ surface\ resistance, R_s = \frac{1}{\delta\sigma}\ Ohm \tag{2.18}$$

$$Skin\ depth, \delta = \sqrt{\frac{2}{\omega\mu\sigma}\ Meters} \tag{2.19}$$

where, σ is the conductivity of the metal in Siemens/meter.

$\omega = 2\pi f$ is the angular frequency.

μ is the permeability.

Though the length of the SW transmission line is decreased, the loss per unit length is higher. The total loss of the transmission line is the factor which needs to be taken care as given by equation 2.20. The structures need to be optimized for component with reduced size while keeping the loss of the total transmission line at a minimum value.

$$Total\ loss\ of\ the\ structure = Loss\ per\ unit\ length\ \times Total\ \ Length \tag{2.20}$$

2.3 DESIGN AND FABRICATION

In this section, Coplanar Waveguide (CPW) slow wave structures with various shapes were designed using standard HFSS at 60GHz. The wave port was used in “port set-up”; bottom surface was assigned as ‘Perfect E’ while other surfaces were kept as

‘Radiation’ to make it similar to our characterization set up. The pitch, shape of the signal and ground conductor was further optimized for the structure with the most promising shapes. The length of the conductor sections was varied for the first time during this optimization process. The S-parameters were extracted from the HFSS and the RLGC parameters were extracted from the S-parameters using the equations in 2.21-2.27 [91]. The equivalent quarter wavelength, characteristics impedance, insertion loss were calculated based on the measured S-parameter and extracted RLGC parameters. Multiple masks were designed with AutoCAD according to the dimension, shape and length derived by the design procedure.

$$\gamma = \frac{1}{l} * \left\{\frac{1-S_{11}{}^{2}+S_{21}{}^{2}}{2S_{21}} \pm K\right\} \tag{2.21}$$

$$K = \frac{(S_{11}{}^{2}-S_{21}{}^{2}+1)^{2}-(2S_{11})^{2^{\frac{1}{2}}}}{(2S_{21})^{2}} \tag{2.22}$$

$$Z^{2} = z_{0}{}^{2}\,\frac{(1+S_{11})^{2}-S_{21}{}^{2}}{(1-S_{11})^{2}-S_{21}{}^{2}} \tag{2.23}$$

$$R = Re\{\gamma Z\} \tag{2.24}$$

$$L = \frac{Im\{\gamma Z\}}{\omega} \tag{2.25}$$

$$G = Re\{\frac{\gamma}{Z}\} \tag{2.26}$$

$$C = \frac{Im\{\frac{\gamma}{Z}\}}{\omega} \tag{2.27}$$

SWSs were fabricated on a high resistivity (10kΩ-cm) silicon substrate using standard optical lithography. The thickness of the metal was measured to be 0.9µm-1 µm after fabrication.

2.4 CHARACTERIZATION USING NOVEL ON WAFER CALIBRATION METHOD

A novel on wafer calibration method was developed for the measurement of RF passive components with R&S VNA. The calibration method employed the HFSS simulation results along with multi-level optimizations to get the nominal values used for on wafer calibration. Multiline TRL (Thru-Reflect-Line) calibration standards fabricated on the same substrate are used with better accuracy. Measured results show that a thru line provides less than 0.015dB insertion loss throughout the frequency range of 1GHz-67GHz. This result is much better compared to the results achieved by conventional SOLT (Short-Open-Load-Thru) calibration and TRL calibration using the available calibration substrates. Using this calibration technique, the phase shift of the thru line shows less than 3° variation at 67GHz which is much lower than 15° achieved by the conventional calibration methods.

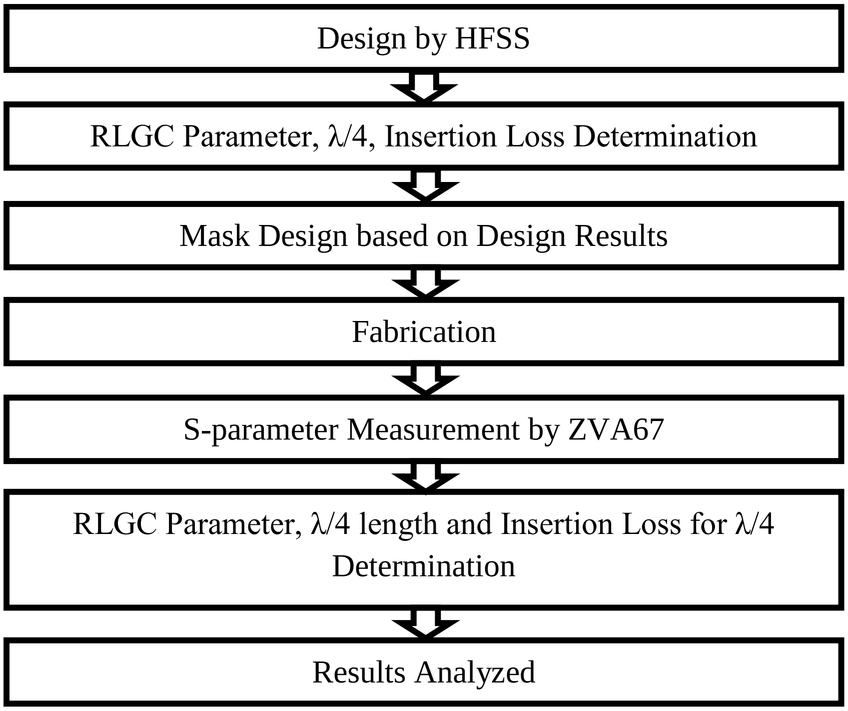

Figure 2.4 Design procedure of slow wave structure analysis.

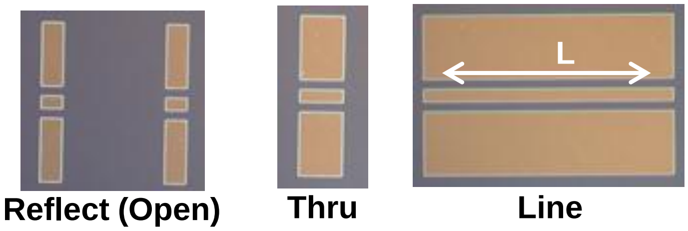

Reflect (Open) Thru Line

Figure 2.5: Fabricated on-wafer calibration standards on real substrate using same metal thickness.

2.4.1 FABRICATION OF CALIBRATION STANDARDS

Multiline TRL calibration standards (Open, Thru, Lines) were fabricated on the same substrate on which real devices had been fabricated with 1µm thick gold (Au) structures. Figure 2.5 shows the fabricated calibration standards used during the TRL calibration. Contact probing pads in the real sample create extra loss in of the measurement with conventional calibration methods. The source of this additional loss is shown in Figure 2.6. The losses from contact pads, cables, connectors and RF probes are de-embedded during the calibration using the proposed calibration method. Figure 2.7 shows R&S vector network analyzer, DUT and RF probes used in the measurement. Four different co-planar transmission lines having the physical length of 478µm, 956µm, 1912µm and 3826µm were used in multiline TRL calibration method.

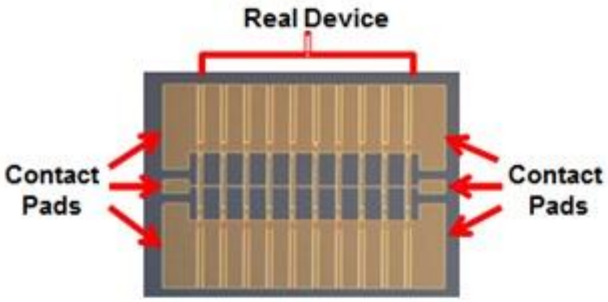

Figure 2.6: Real device along with contact pads at both sides. Loss from these contact pads creates addition loss.

Table 2.1: Frequency range associated with each fabricated calibration standard line

	Phys. Length (μm)	**Elec. Length (μm)**	**Calc. Freq. Range (GHz)**	**Opt. Freq. Range (GHz)**
Line-1	478	1205	1.726-13.81	1.726-10.36
Line-2	956	2410	3.455-27.64	10.36-20.73
Line-3	1912	4821	6.911-55.29	20.73-41.47
Line-4	3824	9648	13.82-110.6	41.47-110.6

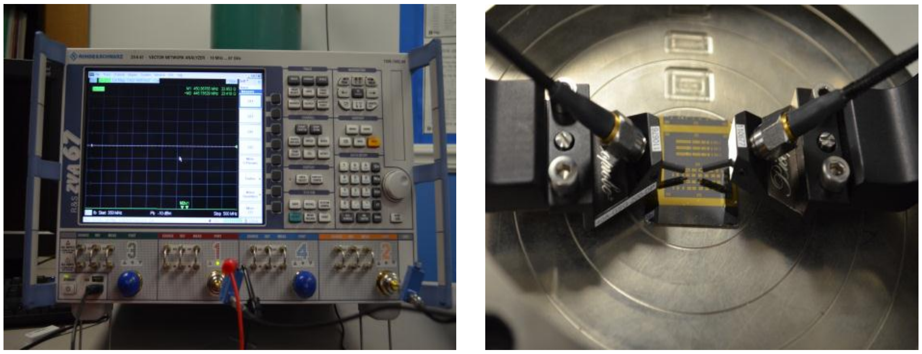

Figure 2.7: (A) (a) R&S vector network analyzer, model # ZVA 67 and (b) Device under test (DUT) and RF probes.

2.4.2 OPTIMIZATION OF FREQUENCY RANGE

The equivalent dielectric constant of the coplanar waveguide (CPW) structure is calculated as 6.36 [90]. The nominal value of the electrical length to be used during the calibration process of R&S VNA is calculated and summarized in Table 2.1. The length of the lines is chosen in such a way that singularity error doesn't occur during the computation of correction data by the network analyzer. For example, if the phase shift created by a certain line is n*180°, the singularity error takes place. In order to avoid the singularity error, the frequency range for a certain line is determined in such a way so

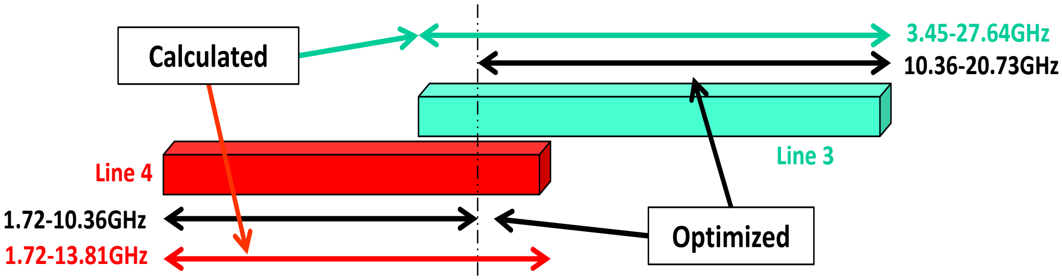

Figure 2.7: (B) Demonstration of frequency optimization in case of overlapping.

that it creates a phase shift of (20°-160°)+n*180°. The following equations are used to calculate the frequency range for a certain line avoiding any singularity error.

$$f\_start = (20° + 0 * 180°)/360° * c/\nabla l \qquad 2.28$$

$$f\_stop = (160° + 0 * 180°)/360° * c/\nabla l \qquad 2.29$$

In case of overlapping the frequency range, the VNA considers a middle point for the optimized line frequency range as shown in Figure 2.7(b). The calculated frequency range of line-4 and line-3 is 1.72GHz-13.81GHz and 3.45GHz-27.64GHz respectively. The R&S vector network analyzer considers the range of the frequencies for line-4 and line-3 as 1.72GHz-10.36GHz and 10.36GHz-20.73GHz respectively. Table 2.1 shows a detailed frequency range description of the four different lines. According to Table I, our proposed calibration method is able to perform the measurement from 1.726GHz-110.6GHz.

2.4.3 SELECTION OF LOSS FACTOR

The value of loss factor {dB/sqrt(GHz)} for each lines is to be inserted at R&S vector network analyzer. The values related to the loss are normally provided by the calibration substrate manufacturing company such as GGB Inc. However, the loss factor values for the fabricated calibration standards in this proposed method is unknown.

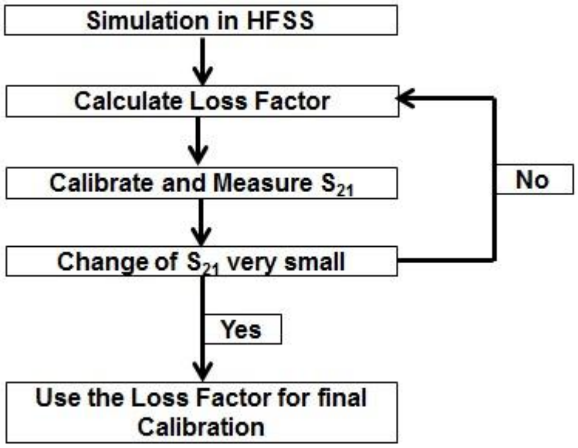

Fig. 2.7: (C) Work flow chart for optimization of loss factor.

Simulation of each calibration standard line using High Frequency Structure Simulator (HFSS 14.0) has been performed to evaluate these values. The simulated loss factor {dB/sqrt (GHz)} values were used during the first round of calibration. The S-parameters of all the four lines were measured based on this calibration. Using measured S-parameter values, the values of loss factors were calculated dividing the insertion loss in dB by the square root of the frequency in GHz. These values were used for the second round of calibration followed by the S-parameters measurement and the loss factor calculation. The change of S_{21} from the previous steps were measured after each steps and compared with a tolerance limit. This process of optimization was continued until the errors or the change of S_{21} in two consecutive steps comes to a minimum limit (e.g. 0.002dB). Fig. 2.7(c) shows the flow chart of the optimization process while Table 2.2 lists all the values of loss factors used during the optimization process. The acceptable values of loss factors were determined in this way and used for the final calibration. The optimization process was used for all the next measurements and not repeated for the next time. The thru line was measured using both the proposed calibration method regular calibration methods like SOLT and TRL by using standard calibration standard, CS-5. The measured results of the thru line were compared to check the validity of the proposed calibration methods.

Table 2.2: Calculated loss factors calculated at the center of frequency range for different lines

Line	**Round-1 dB/sqrt(f)**	**Round-2 dB/sqrt(f)**	**Round-3 dB/sqrt(f)**	**Round-4 dB/sqrt(f)**
Source	Simulation	Round-1 Meas.	Round-2 Meas.	Round-3 Meas.
Line-1	0.0189	0.0225	0.0232	0.0227
Line-2	0.0288	0.0505	0.0473	0.0459
Line-3	0.0541	0.0943	0.0939	0.0934
Line-4	0.1182	0.1916	0.1965	0.1948

2.4.4 VERIFICATION OF CALIBRATION

The same thru line were measured using the three different calibration methods: proposed calibration method, SOLT calibration using CS-5 and TRL calibration using CS-5. Theoretically, the insertion loss and the phase shift measured from a thru line should have been close to zero. The insertion loss measured using the proposed calibration methods were less than 0.015dB for the frequency range of 1GHz-67GHz as shown in Fig. 2.8. The results using the SOLT calibration showed good performance at the lower frequency region but it was not acceptable after 30GHz as the amount of ripples becomes significant. Though the results using TRL calibration with the help of CS-5 was bad result at lower frequencies, it was better than SOLT at higher frequencies.

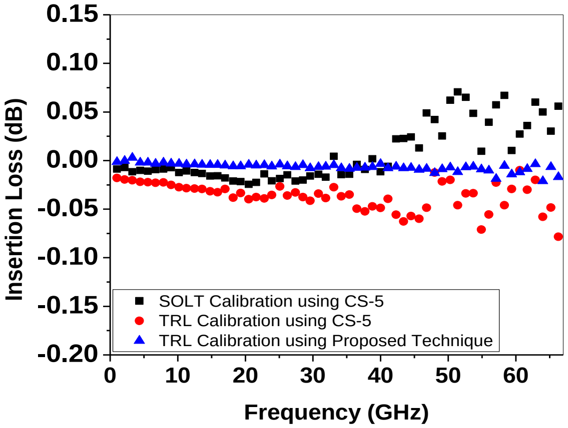

Figure 2.8: Comparison of the insertion loss of a thru line achieved by different calibration techniques.

The phase shift created by the thru line measured using three different techniques are presented at Figure 2.9. A small phase shift change of 3° was shown at 67GHz for the proposed calibration method while phase shift change of around 15° had been resulted from the conventional methods. It clearly verifies the validity and acceptability of our measurement systems over the conventional methods. Though the theoretical calculation allows the operation until 110GHz, the results had been reported until 67GHz as limited by the R&S VNA (model- ZVA67) and RF probes.

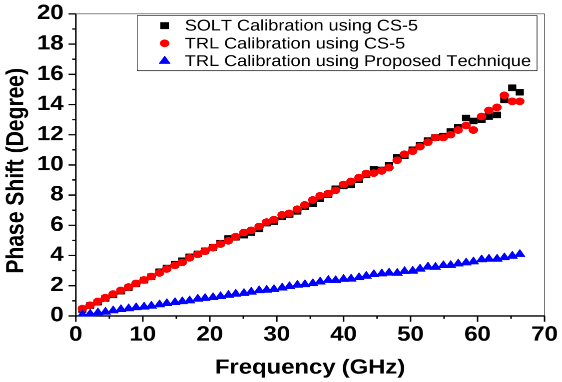

Figure 2.9: Comparison of the phase shift of a thru line achieved by different calibration techniques.

2.4.4 FINAL CHARACTERIZATION OF SWS

The S parameters of the slow wave structures were measured using R&S vector network analyzer after the calibration process had been finalized. The RLGC (resistance, inductance, conductance and capacitance) were extracted using the equations 2.21-2.27 [3]. The equivalent quarter wave length and the loss associated with were calculated and analyzed at 60GHz. A complete flow chart of the work demonstrating different steps is shown in Figure 2.4.

2.5 RESULTS AND DISCUSSION

The goal of the optimization process of SWS is to achieve higher slow wave effect while maintaining the loss as low as possible. Various types of slow wave structures with different shapes had been analyzed at first. The SWS with best result had been further optimized by changing the signal conductor, ground conductor, pitch, section length etc. All the methods were incorporated together to achieve the final optimization. The results for each step are described in the following sections.

2.5.1 RSESULTS: VARIOUS SHAPES OF SWS

A fabricated regular non slow wave CPW structure is presented in Figure 2.10 (A) while step type, zigzag type and defected ground type SWSs are presented in Figure 2.10(B-D). The measured result of regular non slow wave CPW structure has been compared with that of slow wave structures. The inductance and capacitance of a regular non slow wave structure was measured as 412.12nH/m and 0.1638nF/m respectively. The quarter wavelength and the insertion loss associated with that were measured as 506µm

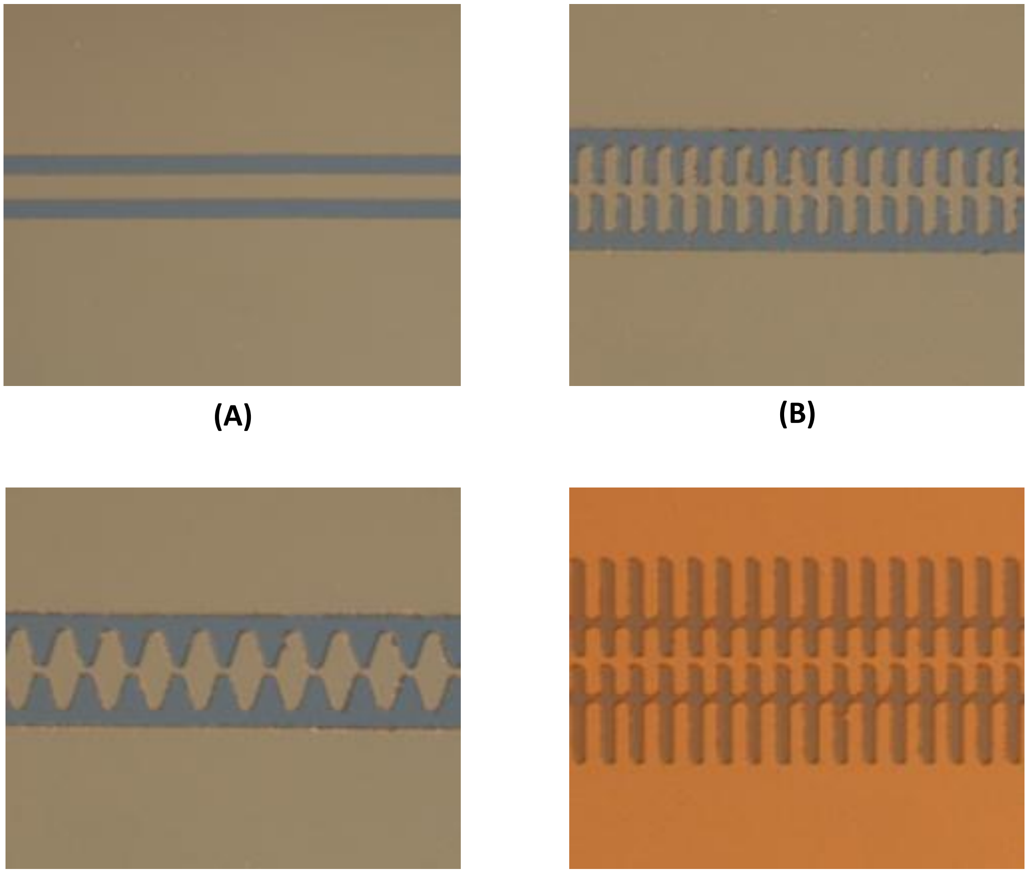

(A) (B)

(C) (D)

Figure 2.10: (A) Regular non-SWS (B) Step type SWS (C) Zigzag type SWS (D) Defected ground type SWS.

and 0.508dB respectively. The step type slow wave structure was introduced with large distance of narrow signal conductor-ground and smaller distance of wide signal conductor-ground to increase L and C value respectively. The increase of the inductance and capacitance value by 34.5% resulted in a quarter wave length of 382μm compared to 506μm for normal structure i.e. 24.5% reduction in length. An additional insertion loss of 0.147dB had been introduced due to the slow wave structure.

One of the sources of the additional insertion loss in step type structure is the mismatch loss between the narrow and wide conductor sections. Taperd line shape has been designed to reduce the loss which was named as zigzag type structure in the dissertation. If the impedances of the narrow and wide conductor sections are Z_1 and Z_2 respectively, a section having an impedance value of $\sqrt{Z_1 Z_2}$ in the middle reduce mismatch loss. The loss is designed to be zero at one frequency and a finite value at other frequencies. The tapered shape between the sections decreases the mismatch loss for a wide frequency range. Moreover, as the portion of the narrow conductor section is minimized, the resistance of the signal conductor is also decreased i.e. the attenuation loss is reduced. The zigzag type structure as shown in Figure 2.10 (C) reduced insertion loss by 0.067dB compared to the step type structure. The length of the inclined portion was 5µm on each side of wide conductor. Less L and C value were found compared to step type structure as the portion of the sections contributing to the L and C is less. The length of λ/4 line is calculated to be 403µm at 60GHz for zigzag shape slow wave structure.

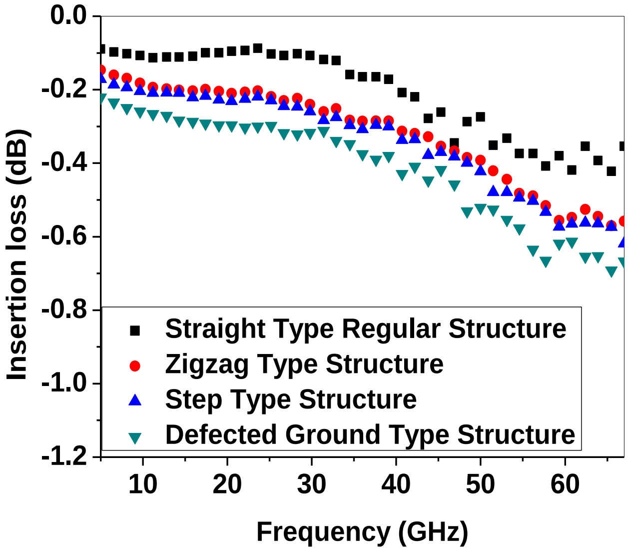

Figure 2.11 Measured insertion loss (dB) of various shaped SWS.

For the designed slow wave structure in the dissertation, reducing the gap between the wide conductor and the ground increases the C value while increasing the gap between the narrow conductor and the ground structure increases L value. The ground conductor of the SWS was accordingly modified to achieve this goal using the defected ground structure. The inductance and capacitance value was increased to 609.88nH/m and 0.2455nF/m for this structure i.e. a quarter wavelength of 340µm at 60GHz. The resistance of the ground conductor was increased due to the change of the ground shape i.e. the attenuation loss is increased to 0.710dB.

Results showed that the defected ground structure is the most promising SWS with the best slow wave effect. The defected ground structures were further optimized in the following sections. The results of the different shaped slow wave structures are listed in Table 2.3.1 while the dimensions of structures are summarized in Table 2.3.2. Here, W_1, W_2, L_1, L_2, S_1 and S_2 represents the width of narrow signal conductor, width of wide signal conductor, length of narrow section, length of wide section, gap from narrow

Table: 2.3.1 Results of various shaped slow wave structures

Structures	**Z_0 (Ω)**	**Freq. (GHz)**	**λ/4 (µm)**	**L (nH/m)**	**C (nF/m)**	**S_{12} for λ/4 (dB)**
Straight	50.17	60	506	412.12	0.1638	0.508
Step	50.89	60	382	554.20	0.2142	0.655
Zigzag	50.06	60	403	520.52	0.2077	0.588
Def. Gnd. type	49.85	60	340	609.88	0.2455	0.710

signal to ground and gap from wide signal to ground respectively.

Table: 2.3.2 Dimensions of various shaped slow wave structures

Structures	**W_1 (μm)**	**W_2 (μm)**	**L_1 (μm)**	**L_2 (μm)**	**S_1 (μm)**	**S_2 (μm)**
Straight	20	20	N/A	N/A	15	15
Step	5	35	5	5	22.5	7.5
Zigzag	3	35	5	5	23.5	7.5
Def. Gnd. type	3	30	5	5	23.5	3

Table: 2.4.1 Results of DGS slow wave structure with different gap from narrow conductor

Structures	**Z_0 (Ω)**	**Freq. (GHz)**	**λ/4 (μm)**	**L (nH/m)**	**C (nF/m)**	**S_{12} for λ/4 (dB)**
Gap 50	49.85	60	340	609.88	.2455	.710
Gap 70	52.77	60	324	677.99	.2434	.765
Gap 90	55.10	60	289	794.09	.2615	.822

Table: 2.4.2 Dimensions of DGS slow wave structure with different gap from narrow conductor

Structures	**W_1 (μm)**	**W_2 (μm)**	**L_1 (μm)**	**L_2 (μm)**	**S_1 (μm)**	**S_2 (μm)**
Gap 50	3	30	5	5	23.5	3
Gap 70	3	30	5	5	33.5	3
Gap 90	2.5	30	5	5	43.75	3

2.5.2 RESULTS: DEFECTED GROUND STRUCTURE – VARIATION OF GAP

The shape of the signal conductor of the defected ground structure was optimized. The gap between the ground and narrow section was varied while the gap between the wide conductor and the ground structure is kept at 3µm. The width of the wide conductor section was fixed at 30µm while the width of the narrow section is kept fixed at3µm to keep the impedance around 50Ω. The detailed dimensions of this section are shown in Table 2.4.2. The gap between the narrow conductor and ground is varied from 23.5µm to 43.75µm and results are listed in Table 2.4.1. The inductance value is increased from

Table: 2.5.1 Results of DGS slow wave structure having different width for wide conductors

Structures	**Z_0 (Ω)**	**Freq. (GHz)**	**λ/4 (µm)**	**L (nH/m)**	**C (nF/m)**	**S_{12} for λ/4 (dB)**
Ws2 30	49.85	60	340	609.88	.2455	.710
Ws2 35	47.49	60	320	617.81	.2739	.755
Ws2 40	46.30	60	314	614.57	.2866	.819

Table: 2.5.2 Dimensions of DGS slow wave structure having different width for wide conductors

Structures	**W_1 (µm)**	**W_2 (µm)**	**L_1 (µm)**	**L_2 (µm)**	**S_1 (µm)**	**S_2 (µm)**
Ws2 30	3	30	5	5	23.5	3
Ws2 35	3.5	35	5	5	23.25	3
Ws2 40	3.5	40	5	5	23.25	3

609.88nH/m to 794.09nH/m while maintaining the capacitance value almost fixed i.e. the size of the quarter wavelength decreased from 340µm to 289µm. The higher gap between the grounds increased the resistance of the ground which resulted in higher insertion loss as per equation 2.17.

2.5.3 RESULTS: DEFECTED GROUND STRUCTURE – VARIATION OF WIDE SECTION WIDTH

The narrow signal conductor portion and distance from the ground are fixed in this section. The gap between the wide signal conductor and the ground is fixed at 3µm while the width of wide signal conductor is changed from 30µm to 40µm. The capacitance value has increased from 0.2455nF/m to 0.2866nF/m as the parasitic capacitance increased with a little variation of the inductance value from 609.88nH/m to 614.57nH/m. The impedance value slightly decreased from 49.85Ω to 46.30Ω which is a

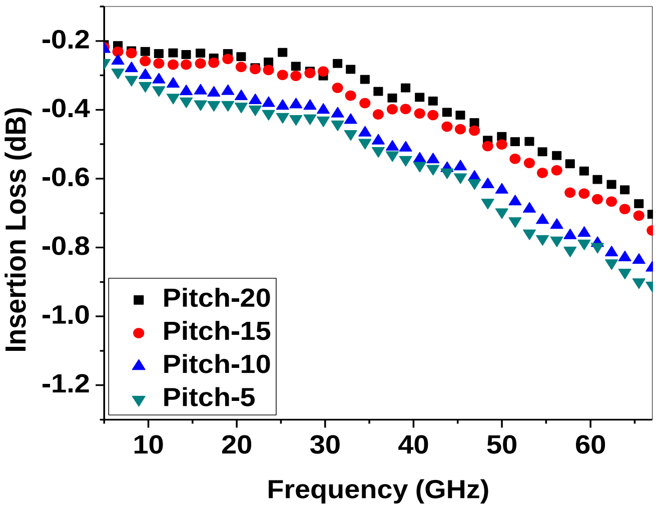

Figure 2.12: Measured insertion losses (dB) of slow wave structures with different pitches.

Table: 2.6.1 Results of various pitched slow wave structures

Structures	**Z_0 (Ω)**	**Freq. (GHz)**	**λ/4 (μm)**	**L (nH/m)**	**C (nF/m)**	**S_{12} for λ/4 (dB)**
Pitch-5	55.10	60	289	794.09	.2615	.822
Pitch-10	53.32	60	325	679.80	.2390	.798
Pitch-15	55.21	60	343	669.99	.2198	.771
Pitch-20	53.56	60	379	625.38	.2180	.724

Table: 2.6.2 Dimensions of various pitched slow wave structures

Structures	**W_1 (μm)**	**W_2 (μm)**	**L_1 (μm)**	**L_2 (μm)**	**S_1 (μm)**	**S_2 (μm)**
Pitch-5	2.5	30	5	5	43.7	3
Pitch-10	3	30	10	10	43.5	3
Pitch-15	3	30	15	15	43.5	3
Pitch-20	3	20	20	20	43.5	3

source of additional loss. The results of characteristics impedance, quarter wavelength, inductance, capacitance and insertion loss are listed in Table 2.5.1 The dimensions of the structures associated with the variation of width sections are listed in Table 2.5.2.

2.5.4 RESULTS: VARIATION OF PITCH

The effect of the pitch of the signal conductor sections is investigated in this section. The width of the signal conductors and the gap from the signal to ground is kept fixed. The length of the narrow and wide section is increased by the same value i.e. the

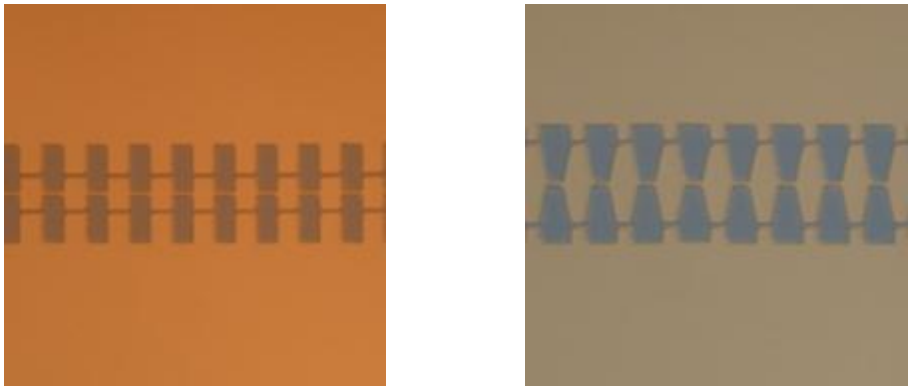

(a) (b)

Figure 2.13: Shapes of (a) optimized defected ground with step type signal structure (b) optimized defected ground with zigzag type signal structure.

pitch of the sections are varied. The notation of the pitch-5 stands for the section length of 5μm for each narrow and wide section. The dimensions of the structures for this process are listed in Table 2.6.2 and the results are listed in Table 2.6.2. A quarter wavelength of 289μm and 379μm has been calculated for the pitch-5 and pitch-10 section. The smaller sections i.e. higher pitched devices showed the higher inductance and capacitance as the parasitic values are higher. It results in higher loss as observed from the data. The excess loss originates from the mismatch loss of more sections. The insertion loss for different SWSs having different pitches has been presented at Figure 2.14.

2.5.5 RESULTS: FINAL OPTIMIZATION

The defected ground type slow wave structure was finally optimized by considering all the options like width of wide conductor, gap ibetween narrow conductor and ground, pitch of the sections. The step type and zigzag type structures have been considered as the signal conductor structure. A novel technique of using different section length was used which gives the design flexibility of characteristics impedance value.

Table: 2.7.1 Results of various shaped slow wave structures

Structures	**Z_0 (Ω)**	**Freq. (GHz)**	**λ/4 (µm)**	**L (nH/m)**	**C (nF/m)**	**S_{12} for λ/4 (dB)**
Straight	50.17	60	506	412.12	.1638	0.508
Opt. DGN Step type	50.38	60	286	701.69	.2764	0.778
Opt. DGN. Zigzag type	50.30	60	316	688.80	.2718	0.610

Table: 2.7.2 Dimensions of various shaped slow wave structures

Structures	**W_1 (µm)**	**W_2 (µm)**	**L_1 (µm)**	**L_2 (µm)**	**S_1 (µm)**	**S_2 (µm)**
Straight	20	20	N/A	N/A	15	15
Opt DGN Step type	4	60	12.5	10	43	3
Opt. DGN. Zigzag type	4	60	12	10	43	3

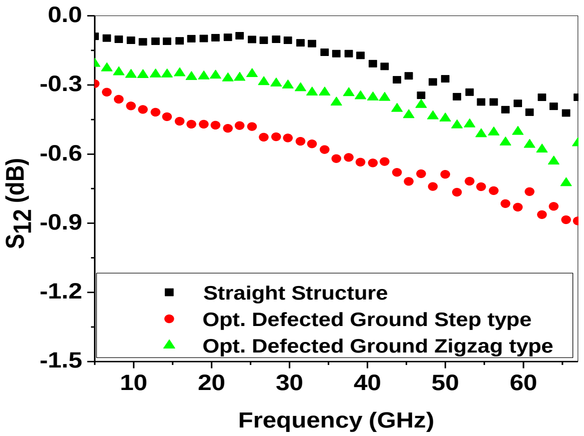

Figure 2.14: Measured insertion loss (dB) of slow wave structures with different.

The characteristic impedance is very important in terms of reflection loss. Two optimized structures i.e. optimized defected ground step and zigzag type structures are presented in Figure 2.13. The detailed results and the dimensions of the final optimized structures are listed in Table. 2.7.1 and 2.7.2. The insertion loss of the regular non slow wave structure and optimized defected ground structures has been presented at Figure 2.14. Optimized defected ground step type structures decreased the quarter wavelength by 43.47% in the expense of 0.27dB loss at 60GHz which can save around 68% area of a Branch Line Coupler. Optimized defected ground zigzag type structures decreased the quarter wavelength by 37.54% while the insertion loss is increased by 0.102dB only which can save around 61% area in a Branch Line Coupler.

CHAPTER 3

FERRO-MAGNETIC THIN FILM INTEGRATION FOR INDUCTNACE TUNING

In the previous chapter, slow wave structures have been optimized using microwave theory and techniques. The width of the narrow section and the gap between the wide section and ground has to be smaller to achieve higher slow wave effect, which generate fabrication constraints. In this chapter, Permalloy (Py) thin film has been employed on the top of the narrow section to improve slow wave effect and demonstrate frequency tuning. The fundamentals of the inductance, the ferro-magnetic thin film and the selection criterion of the Py have been clarified. The Py thin film was grown by DC magnetron sputtering and patterned. Selective patterning of Permalloy of different thickness in nano-meter and micro-meter scale has permitted the operation at very high frequency; moreover, increased the inductance value. Frequency tunable SWSs integrated with patterned Py were designed, fabricated and characterized. This chapter presents the improvement of the slow wave effect and the frequency tuning by the use of thick ferro-magnetic material patterned in a special way.

3.1 INDUCTANCE

Inductance of a coplanar two wire line can be defined as [146]:

$$Inductance, L = \frac{\mu_0 \mu_r}{\pi} cosh^{-1}\left(\frac{d}{w}\right) \qquad 3.1$$

Where, permeability of the core material, $\mu = \mu_0 \mu_r$

μ_r is the relative permeability of the core material,

μ_0 is the permeability of air,

d is the gap in between two wires,

w is the width of the traces,

As shown in Equation 3.1, when w and d are constant, inductance value (L) depends on permeability only i.e. larger inductance with higher permeability and thereby better slow wave effect. Moreover, different inductance value can be achieved with varied permeability. Thus choosing a material with high adjustable permeability value is very critical for a compact and tunable slow wave component.

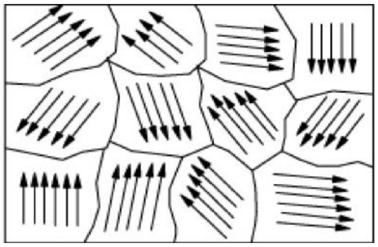

Figure 3.1: Small magnetic domains [132].

3.2 FERRO-MAGNETIC THIN FILM

The relative orientation of the spins of two electrons is responsible for electronic exchange force. This electronic exchange force produces strong interactions which results in parallel alignment of atomic moments. The alignment of the atomic moments is the distinguishing factors among ferromagnetic, paramagnetic and diamagnetic materials. Ferromagnetic materials possess parallel alignment of atomic moments which results in large net magnetization along a particular direction unlike paramagnetic and diamagnetic materials even in absence of an external magnetic field.

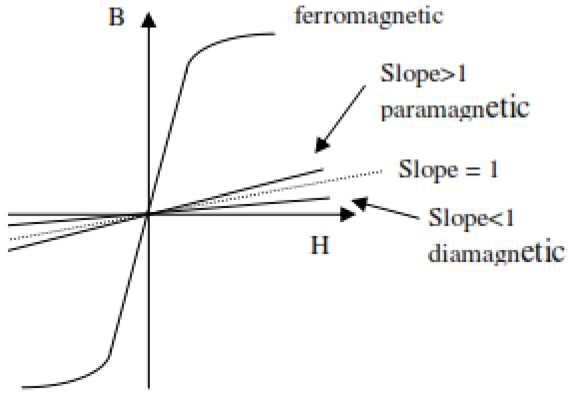

Figure 3.2: B-H Curve showing the difference between ferro, para and diamagnetic material. [133]

According to a theory postulated in 1907 and experimentally verified in 1930, magnetic domain is the called the small sub divisions in a ferromagnetic material as shown in Figure 3.1. They are by default magnetized to saturation but the magnetization direction varies from one domain to another. As a result, the total vector sum of all the magnetization is nearly zero [92]. Magnetic anisotropy is the property of a magnetic material to get directionally dependent. Thus, a magnetically isotropic material doesn’t orient the magnetic moment along any preferred direction. Easy axis is called the direction of spontaneous magnetization which is favored energetically. The magnetically anisotropic materials spontaneously align themselves along the easy axis [92]. There are mainly three types of anisotropy: magneto crystalline anisotropy, stress anisotropy and shape anisotropy.

3.2.1 MAGNETO CRYSTALLINE ANISOTROPY

Magneto crystalline anisotropy is an intrinsic property of a ferromagnetic material which doesn't depend on the grain size and shape. The ferro-magnetic material has the inherent property of magneto crystalline anisotropy which the diamagnetic and paramagnetic material doesn't possess. As the goal of the dissertation is to increase the inductance value by using magnetic thin film, the ferro-magnetic material has to be chosen.

3.2.2 STRESS ANISOTROPY

Magnetostriction is a phenomenon related to spin-orbit coupling which arises from the shape change of the orbitals. In case of stress anisotropy, a previously demagnetized crystal experiences a strain and therefore changes its dimension in presence of magnetization i.e. the material property is changed permanently. The stress anisotropy has to be avoided in case the material is to be used multiple times. That's why choosing a ferro-magnetic material with a very low stress anisotropy value is very important.

3.2.3 SHAPE ANISOTROPY

Shape anisotropy is the only anisotropy which can be introduced after the growth of the ferro-magnetic thin film. It is directly related to the shape of the ferro-magnetic

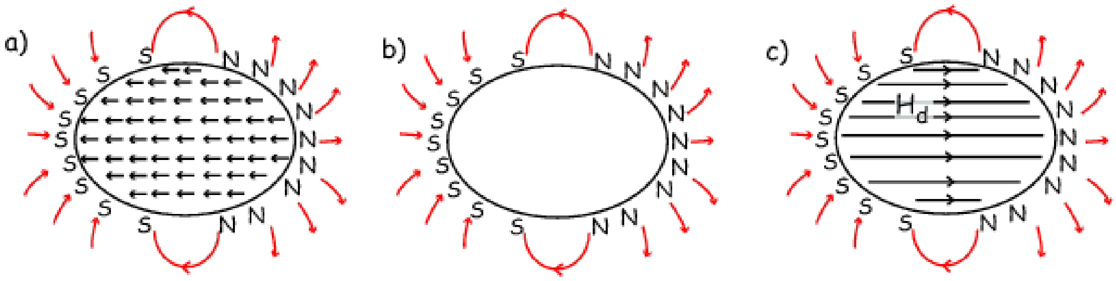

Figure 3.3: a) Internal magnetizations within a ferromagnetic sphere emerging from magneto crystalline anisotropy. b) Generation of an identical external field from a series of surface monopoles. c) The internal "demagnetizing" field resulting from the surface monopoles. [93, 130]

material. As the ferro-magnetic material has the inherent net magnetic moment along a certain direction even in absence of an external magnet, the magnetized body produces magnetic charges or poles at the surface due to the internal magnetization.The magnetic charges or poles can be identified as the north and south pole as shown in Figure 3.3. The surface charges generate external magnetic fields from the surface monopoles whose direction is from the north pole to south pole. The external magnetic field creates an internal demagnetizing field due to the continuation of the externally generated magnetic field which is called the demagnetizing field as it acts in opposition to the magnetization that produces it. The total net magnetic anisotropy of the ferro magnetic material can be defined as, $H_{ani}=H_{mag} - H_{demag}$, where H_{mag} is the inherently present magnetic anisotropy and H_{demag} is demagnetizing field created by the magnetized body. Less net magnetic anisotropy results in case of higher demagnetizing field. The net magnetic anisotropy field has to be increased as the inductance per unit length increases with magnetic anisotropy i.e. demagnetizing field has to be decreased. One of the ways to decrease the demagnetizing field is to separate the north and south pole by a big margin along the easy axis. The demagnetizing field decreases as the external magnetic field created along the easy axis can't reach from north pole to south pole. Increase of the aspect ratio along the easy axis of magnetization can serve this purpose. In a long shaped rectangular object, the demagnetizing field will be less compared to a short object. In this dissertation, the ferromagnetic thin film has been patterned to create the anisotropy i.e. shape anisotropy [93].

3.3 PERMALLOY

The ferromagnetic material, Permalloy is a nickel-iron magnetic alloy with a composition of 80% nickel and 20% iron. Py has very high magnetic permeability of around 170-650 near DC [94] though permeability value strongly depends on the thickness, material quality, deposition method etc. Py has low coercively, significant anisotropic magneto resistance and near zero magnetostriction i.e. less chance of stress anisotropy. As the magnetic property is not expected to change permanently for any magnetization, Py is expected to show stable application. Electrical resistivity of Py can vary as much as 5% depending on the strength and the direction of an applied magnetic field i.e. impedance mismatch is very low [95]. The slope of the B-H curve which represents the permeability is very high and changeable in case of Py as it is a ferromagnetic material. Permalloy changes the rate of the change of magnetic flux density with the application of the external magnetic field i.e. it has the potential to represent different inductance value. Tuning of the inductance value is possible using the external DC current as it can generate the external magnetic field.

3.4 FERROMAGNETIC RESONANCE

Landau Lifshitz Gilbert (LLG) equation describes the damped motion of a magnetic moment about the direction of an external magnetic field.

$$\frac{d\vec{M}}{dt} = -\mu_0\gamma\vec{M}\ X\ \vec{H}_e + \frac{\alpha}{M}(\vec{M}\ X\ \frac{d\vec{M}}{dt}) \qquad 3.2$$

If a varying force which is perpendicular to demagnetizing field ($\vec{H}_e$) is applied on the magnetic moment, it can make it precess about the equilibrium direction. If this force has a frequency similar to the precessional frequency of $\vec{M}$, a maximum of energy absorption by the ferromagnetic sample is observed in the plot of S_{21} as a crest which is called ferromagnetic resonance (FMR). The value of inductance contributed by the ferro-magnetic thin film becomes less than zero after the FMR frequency; moreover, the value of L becomes unpredictable [64]. Thus the FMR frequency of the ferro-magnetic thin film should be as high as possible to allow the operation at high frequency range.

Frequency of ferromagnetic resonance can be calculated by Kittel's formula [96].

$$f_r = \frac{\gamma}{2\pi}\sqrt{(H_{Bias} + H_{Ani} + (Ny - Nz)4\pi Ms)(H_{Bias} + H_{Ani} + (Nx - Nz)4\pi Ms)} \qquad 3.3$$

where H_{Bias} is applied external bias field,

H_{Ani}=Inherent anisotropy field of the magnetic material,

M_s=Saturation magnetization,

$(Ny - Nz)4\pi Ms$ and $(Nx - Nz)4\pi Ms$ are the contributions to magnetic anisotropy due to the shape,

N_x, N_y, N_z are demagnetizing factors along different directions,

γ=gyromagnetic ratio.

The saturation magnetization, inherent anisotropy and gyromagnetic ratio are fixed for a particular ferro-magnetic thin film while external magnetic bias field can be created by any permanent magnet or DC current. Demagnetizing factors depends on the dimensions of the Py patterns. The Py thin film needs to be patterned to increase the shape anisotropy field by increasing $(\mathrm{Ny} - \mathrm{Nz})4\pi\mathrm{Ms}$ and $(\mathrm{Nx} - \mathrm{Nz})4\pi\mathrm{Ms}$.

3.5 CONCEPT OF PATTERNING: FERROMAGNETIC RESONANCE

Because of high demagnetizing field, the net anisotropy field is very low in ferro-magnetic thin film when no external magnetic field is applied. The ferro-magnetic resonance frequency of Py falls in sub-gigahertz region without patterning and external bias field. The external magnetic field applied along the easy axis of magnetization can increase the FMR frequency by increasing the anisotropy field as per Kittel's law [96], however a large magnet is not feasible in a practical circuit board. In this dissertation, the shape anisotropy has been introduced by patterning Py with high aspect ratio along the easy axis of magnetization. Figure 3.4 shows SEM photo of fabricated CPW with nano-patterned Py. The dimensions of the fabricated nano patterned Py bars were $10\mu\mathrm{m} \times 150\mathrm{nm}$, $10\mu\mathrm{m} \times 250\mathrm{nm}$ and $10\mu\mathrm{m} \times 500\mathrm{nm}$ while the thickness and gap in between Py bars were kept fixed at 100nm.

For the dimensions of $10\mu\mathrm{m} \times 150\mathrm{nm}$, the demagnetization coefficients are approximated as N_y=.0013[96] and N_z=.0069, N_x=.9918[97]. For Permalloy, the

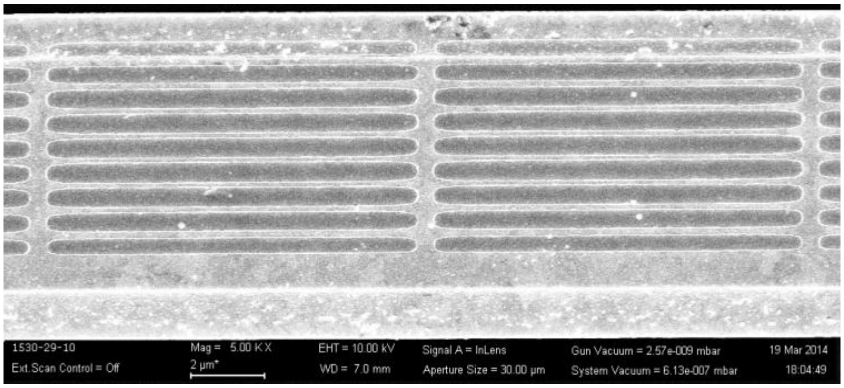

Figure 3.4: SEM photo of nano-patterned Py.

saturation magnetization, $4\pi M_s$ is 9KG and gyromagnetic ratio, γ is 176GHz/T [98]. By fitting the results into Kittel's equation, an anisotropy field of 45.75KA/m has been estimated which results in a FMR at 6.3GHz. Theoretical calculation and OOMMF (object oriented micro magnetic framework) simulation as shown in Figure 3.5 hints the FMR frequency should be around 13.5GHz. Better patterning and quality of Py can be a solution for the low FMR frequency.

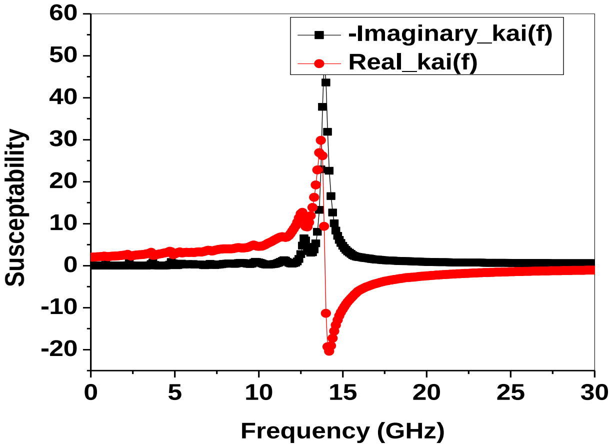

Figure 3.5: OOMMF simulated susceptibility results for patterned Py (10µm × 150nm).

3.5.1 CONCEPT OF PATTERNING: MAGNETIC ANISOTROPY

The value of inductance per unit length highly depends on total magnetic anisotropy along the easy axis. Permalloy has inherent high magneto crystalline anisotropy but the demagnetizing field created by the external magnetization reduces the total magnetic anisotropy. Py was patterned with high aspect ratios where the long axis

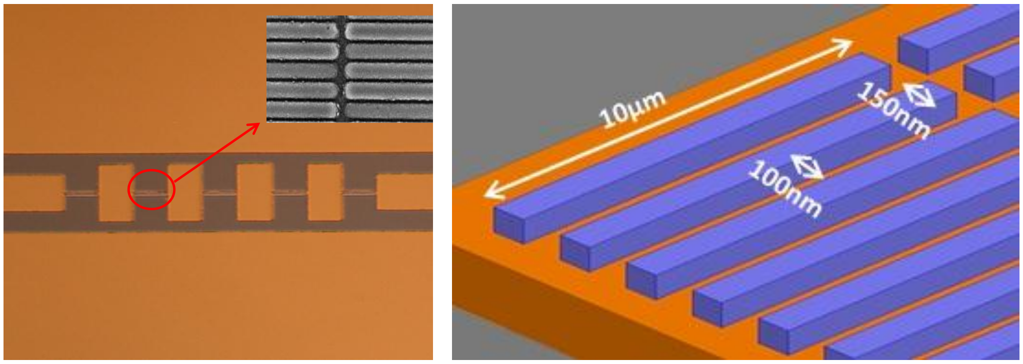

Figure 3.6: Photo of permalloy enabled SWS (left) and sub micro meter patterned Py (right).

was aligned along the easy axis which decreased the demagnetizing field resulting in higher anisotropic field and hence high magnetic field density.

3.6 FABRICATION

Two type devices were fabricated e.g. device A and device B. Device A was fabricated with 100nm thick nano-patterned Py while device B was fabricated with micro-patterned Py with a thickness of 100nm and 200nm. For device A, simple slow wave structure was fabricated with the following dimensions:

Total length of the device, L is 450µm,

Width of the narrow conductor section, W_1 is 5µm,

Width of the wide conductor section, W_2 is 110µm,

Length of the narrow conductor section, L_1 is 50µm,

Length of the wide conductor section, L_2 is 50µm,

Gap in between ground conductors, G is 150µm,

Thickness of the metal, t is 1µm.

High resistivity (100kΩ-cm) Si substrate was used to decrease substrate loss. Standard optical lithography was used to pattern the thick metal structure on top of the Si

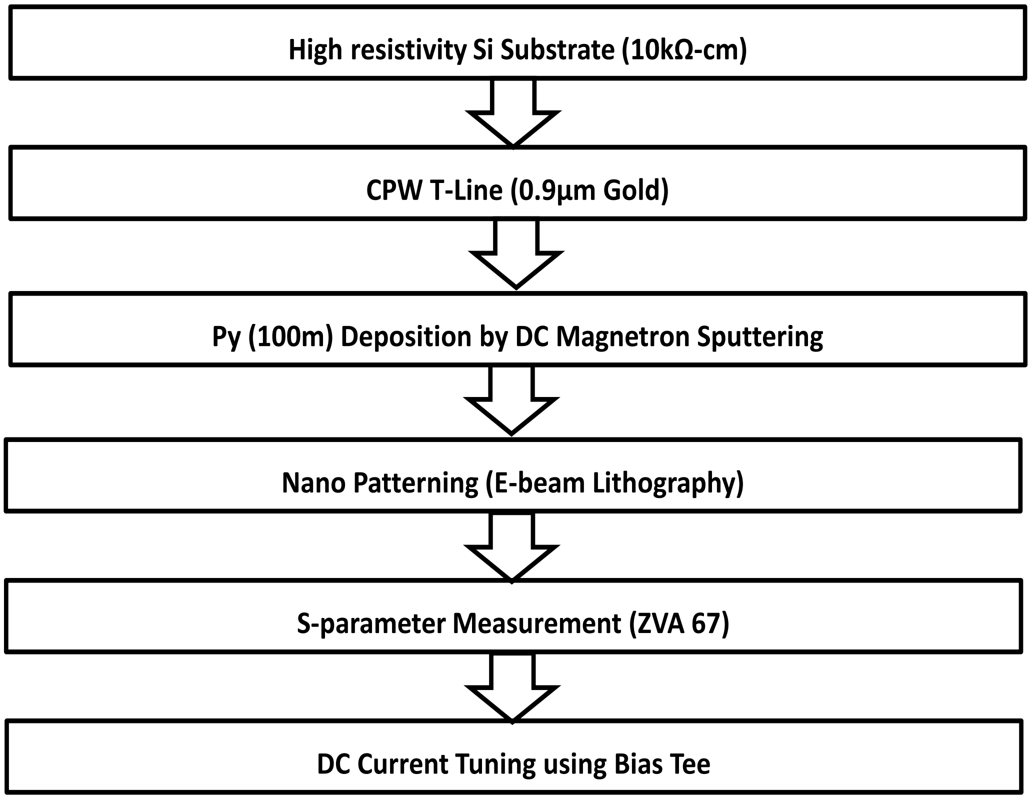

Figure 3.7: Design flow chart of tunable slow wave structure.

substrate and 100nm thick Py film was deposited on top of the narrow signal conductor portion (responsible for L value) only using DC magnetron sputtering. Sub micrometer patterning of Py was performed using E-beam lithography whose dimensions are provided below:

Length of the Py bar, l is10µm,

Width of the Py bar, w is 150nm,

Gap in between Py bars, g is 100nm,

Thickness of the Py bar, t is 100nm,

Figure 3.6 shows a complete picture of the fabricated tunable slow wave structure and Figure 3.7 summarizes a complete work flow chart for this section.

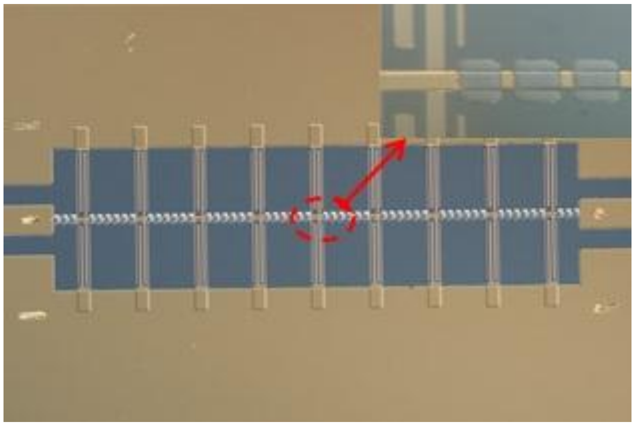

Figure 3.8: Microscope photo of device B.

For device B, CPW slow wave structure was fabricated on high resistivity (10kΩ-cm) Si substrate. The dimensions of the device B is as follows:

Total length of the device, L is 936µm,

Width of the narrow conductor section, W_1 is 7µm,

Width of the wide conductor section, W_2 is 280µm,

Length of the narrow conductor section, L_1 is 84µm,

Length of the wide conductor section, L_2 is 20µm,

Gap in between ground conductors, G is 300µm,

Thickness of the metal, t is 1µm.

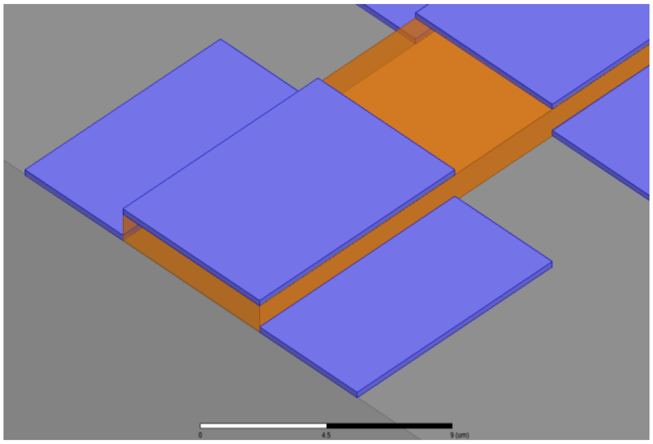

Figure 3.9: Schematic of Py patterning beside the signal conductor

The wide conductor section created an interdigitated capacitor (IDC) with the width and the gap of the IDC line was 5µm and 3µm respectively. The thickness of the Py was kept at 100nm and 200nm respectively while the dimension of the micro patterned Py bar was 10µm×17µm. A 5nm of Cr was used as an adhesion layer of Py on Gold. In case of 200nm thick Py, an intermediate layer of 5nm Cr was used in between two 100nm thick Py. Py was used not only on top of the metal but also beside the narrow section as shown in Figure 3.9 to increase the magnetic flux linkage. The initial plan was to cover the total signal line using Py thin film to increase the inductance by a big margin but this was not possible as the thickness of Py (200nm) was lower than metal (1µm).

The metal thickness was not reduced to less than 1µm to keep the conductor loss minimum. As the Py was deposited using DC sputtering and Cr was deposited using E-

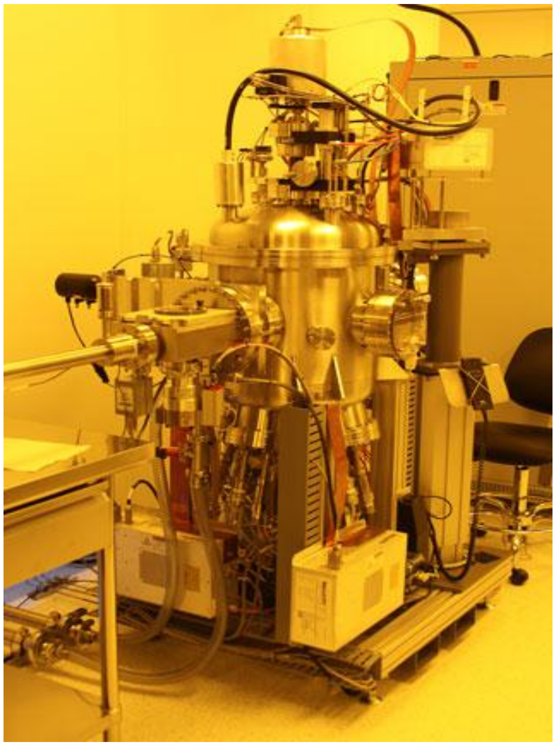

Figure 3.10: Lesker CMS-18 sputtering system.

beam evaporator, the sample had to change the system using load line for every layer of either Py or Cr. A total time of 5 hours was taken to deposit 5nm Cr, 100nm Py, 5nm Cr and 100nm Py i.e. 200nm of Py. That's the reason Py could not be made thick enough to cover the side wall. Figure 3.8 shows a complete structure of micro-patterned Py tunable slow wave structure.

3.7 PERMALLOY THIN FILM DEPOSITION

The Py thin film was deposited in a Lesker CMS-18 sputtering system with a base pressure of around 2 x 10^{-8} Torr. The substrate was rotated at 20rpm during deposition to maintain a uniform thickness of the thin film throughout the sample. The temperature of the sputtering furnace was kept around 300K while a continuous flow of Ar gas was maintained at a pressure 2.1mT. A 3" thick, 99.95% purified Py target (Ni80/Fe20, Williams Advanced Materials) was used for deposition by a DC magnetron gun in confocal geometry with a sample-target distance of 7" and the deposition rate of Py was determined to be 0.023nm/s. No external magnetic field was applied during deposition to orient the magnetic moments along a particular direction as the target was to create the shape anisotropy by patterning.

3.8 CHARACTERIZATION

The S parameters were measured using R&S vector network analyzer ZVA67. The GSG probes with a pitch of 200μm were used to contact the device during measurement as shown in Figure 3.11. The DC current was applied using bias tees to tune inductance value and thereby the center frequency as the experimental setup is demonstrated in Figure 3.12. The application of the DC current created the magnetic field along the hard axis which changed the net magnetic moment along the easy axis. The change in net magnetic moment resulted in a different magnetic anisotropy value i.e. inductance was changed. The DC current applied on the signal conductor also increased the temperature of the devices. The temperature increment results in joule heating effect which also contributes to the tuning of Permalloy property. Optimized multiline TRL (thru-reflect-line) calibration as described in Chapter 2 was used to de-embed the loss from cables, connectors and RF probes. The RLGC (resistance-inductance-conductance-capacitance) parameters were extracted using the equations 2.21-2.27. The FMR frequency for Device A and Device B was determined to be 6.3GHz and 3.2GHz respectively.

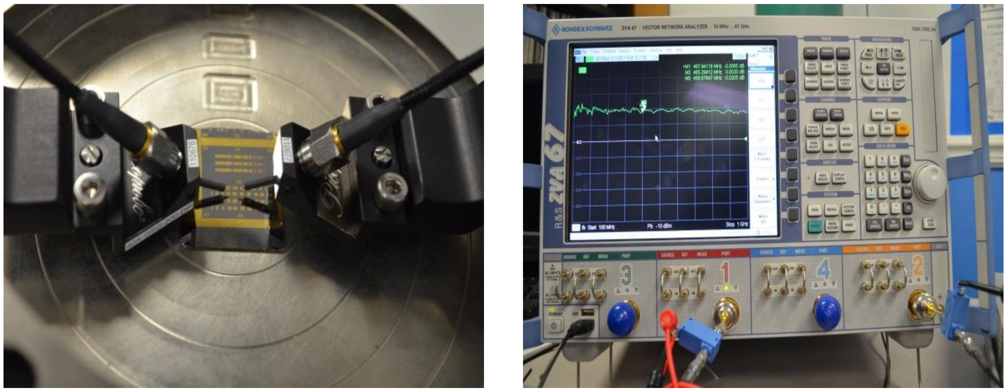

Figure 3.11: Measurement setup showing probes and VNA with the bias-tee.

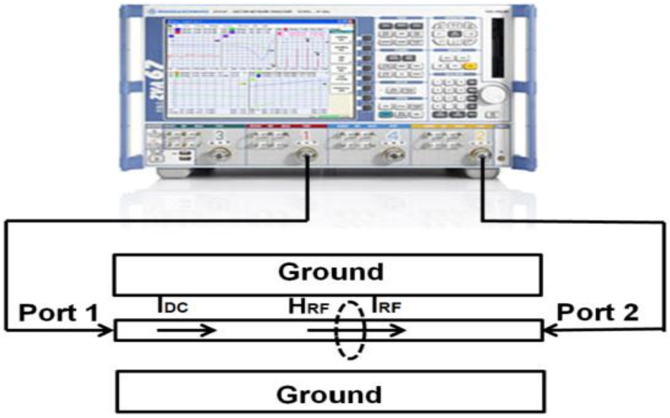

Figure 3.12: Experimental setup for inductance tuning.

The quarter wavelength value, the insertion loss and phase shift were calculated for 4GHz and 2GHz as the operation was limited by FMR frequency. An equivalent quarter wavelength at 4GHz and 2GHz was determined for the slow wave structure without any thin film. The frequency at which that particular physical length created a 90° delay was determined and termed as the center frequency. The results of regular non-slow wave structure were compared with Py enabled tunable slow wave structure with DC current application.

3.9 RESULTS AND DISCUSSIONS

For device A, an FMR frequency of 6.3GHz was observed from the plot of S_{21} as shown in Figure 3.13. The extracted L and C value of regular and tunable SWS at different bias currents is summarized in Table 3.1 and Table 3.2. The results have been shown from 2GHz to 5GHz as the inductance value decreases after 6.3GHz. The

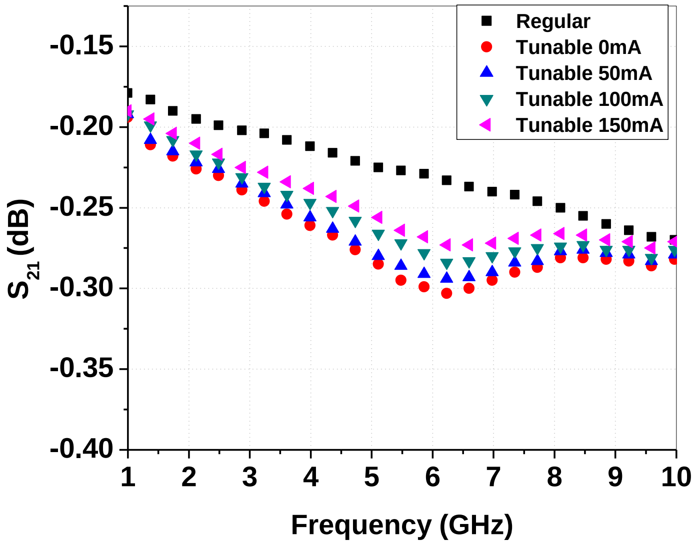

Figure 3.13: S_{21} comparison of nano-patterned Py tunable slow wave structure with different DC current and regular CPW.

Table 3.1: Inductance values of regular and tunable SWS at different external DC current.

Frequency (GHZ)	**2**	**2.5**	**3**	**3.5**	**4**	**4.5**	**5**
Regular (nH/m)	897	887	882	879	879	879	877
Tunable at 0mA (nH/m)	993	983	981	972	961	957	949
Tunable at 50mA (nH/m)	979	967	965	956	947	941	935
Tunable at 100mA (nH/m)	955	943	940	931	920	914	908
Tunable at 150mA (nH/m)	944	933	929	918	909	903	898

Table 3.2: Capacitance values of regular and tunable SWS at different external DC current

Frequency (GHZ)	**2**	**2.5**	**3**	**3.5**	**4**	**4.5**	**5**
Regular (pF/m)	252	252	252	252	251	252	252
Tunable at 0mA (pF/m)	255	254	254	252	252	251	251
Tunable at 50mA (pF/m)	253	252	252	252	251	250	251
Tunable at 100mA (pF/m)	252	252	250	252	250	250	250
Tunable at 150mA (pF/m)	251	251	250	251	250	249	249

insertion loss of the SWS was increased by 0.04dB due to the introduction of Py which is very low. At 4GHz, the L value increased from 879nH/m to 961nH/m by 100nm thick nano-patterned Py while the C value was almost fixed at 0.251nF/m. The introduction of 150mA of DC current decreased the L value from 961nH/m to 909nH/m. The equivalent quarter wavelength of the simple slow wave structure without any thin film was

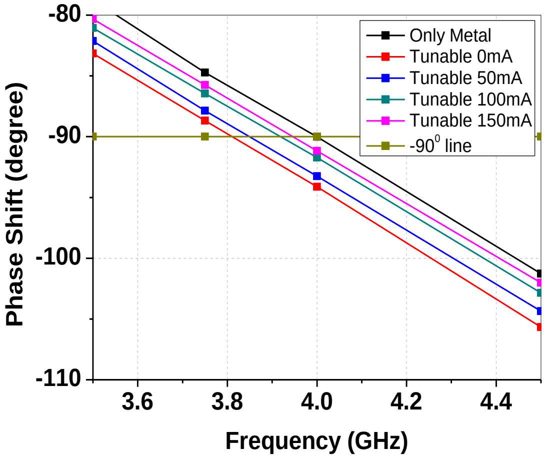

Figure 3.14: Measured phase shift of regular and nano-patterned tunable SWS at different external DC current.

calculated as 4.186mm at 4GHz. Figure 3.14 demonstrates the phase shift created by a 4.186mm long slow wave structure using Py and different DC current.

The phase shift was changed from 95^0 to 92^0 with 150mA DC current as the inductance value changes. Without any thin film, the 4.186mm long slow wave structure created 90^o phase shift at 4GHz. The same line created a 90^o phase shift at 3.81GHz in presence of Py i.e. center frequency was changed from 4GHz to 3.81GHz. Application of 150mA DC current tuned the frequency to 3.95GHz. The suitable selection of DC current can result in any center frequency in between 3.81GHz to 4GHz. The results testify the promise of the device as tunable SWS. Figure 3.15 shows the impedance of the structures with different bias current which shows the potential to be used at impedance matching network.

The magnetic anisotropy of the thin film which is main deciding factor of FMR frequency and inductance value can be changed because of two reasons: Ampere's field along the hard axis of magnetization and Joule heating effect.

From Kittel's law, the total magnetic anisotropy can be approximated from three sources: inherent anisotropy of the ferromagnetic thin film, shape anisotropy and the external bias anisotropy. The total anisotropy would increase if the external magnetic field would have been applied along the easy axis. As the direction of the Ampere's field created by the DC current is along the hard axis in this experiment, DC current i.e. external magnetic field decreases the magnetic anisotropy.

$$f_r = \frac{\gamma}{2\pi}\sqrt{(H_{Bias} + H_{Ani} + (Ny - Nz)4\pi Ms)(H_{Bias} + H_{Ani} + (Nx - Nz)4\pi Ms)}$$

The external magnetic field can be generated by many ways where the use of permanent magnet is the most popular in the field of magnetic materials. In this dissertation, the external magnetic field was generated by the DC current which the most feasible options in a practical circuit board. The maximum Ampere's field for the DC current application can be approximated by the equation below:

$$H_{dc} = \frac{I}{2w} \text{ [99], [100]} \qquad 3.4$$

where I is the applied dc current,

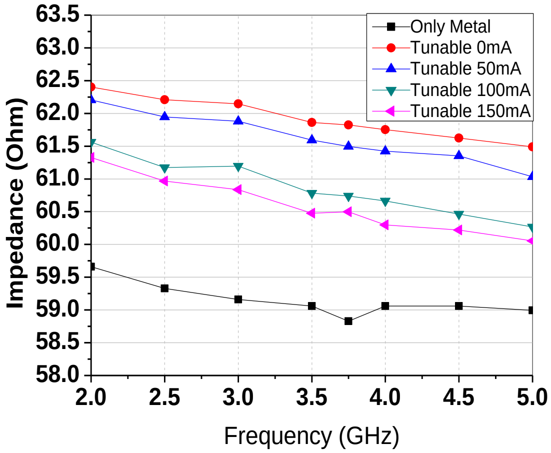

Figure 3.15: Measured impedance of regular and nano-patterned tunable SWS at different external DC current.

w is the width of the central line of the CPW.

This approximation should be very good for Ampere's field across the sample as the 90% of this magnetic field will be interacting with the material.

The value of ampere's field can be calculated as, $H_{dc} = \frac{I}{2w} = \frac{150mA}{2\times 5\mu m} = \frac{15KA}{m}$.

In section 3.5.1, a magnetic anisotropy of 45.75KA/m has been calculated for the nano-patterns used in this dissertation without the application of DC current. The external magnetic field created by 150mA DC current is a significant value compared to the inherent and shape anisotropy i.e. the external magnetic field is a significant reason for the change in magnetic anisotropy. The change in different DC current results in different Ampere's field which changes the net magnetic moment of the ferro-magnetic thin film i.e. the magnetic anisotropy changes. Thus the tuning of the inductance value was achieved using the external magnetic field.

Joule heating effect can be another source for the magnetic anisotropy change. Due to the application of DC current, the heat was generated which was calculated from the resistance change of the Gold transmission line [101]. The increase in temperature due to the Joule heating effect decreased the saturation magnetization, $M_{s.}$ Total magnetic anisotropy decreases with the decrease in saturation magnetization. Moreover, thermal effects like domain reconfiguration [102], and domain wall depinnning [103] can induce domain and tilt the magnetization away from the easy axis which contributes to FMR frequency shift [54].

Resistance of the structure can be defined as, $R = R_0[1 + \alpha(T - T_0)]$ *3.5*

Where R is the resistance at the final temperature, T,

R_0 is the resitance at initial temperature, T_0

α is the temperature co-efficient of the Au which is 3.4× $10^{-3}/degree$

The resitance of the device-A at initial temperature was initially measured as 8Ω while that resistance was increased to 8.5Ω at 250mA. If the initial temperature of the device is considered as 27° C, the final temperature of the device is calculated as 45°C using equation 3.5.

The saturation magnetization of the ferro-magnetic material can be defined as :

$$M_s(T) = M_0[1-(\frac{T}{T_c})^{1.5}] \tag{3.6}$$

Where $M_s(T)$ is the saturation magnetization at final temperature, T

T_c is the curie temperature which is 450°C for Py.

The saturation magnetization of the Py at final temperature is calculated as .9683M_0 i.e. 3.16% change. The effect of the small change in saturation magnetization at total

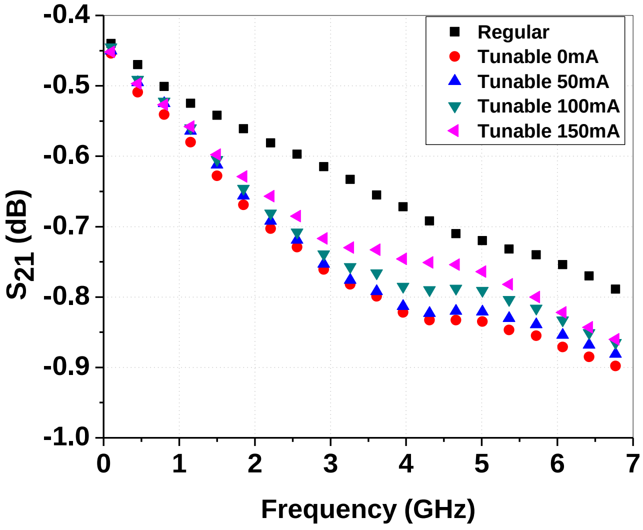

Figure 3.16: Measured S_{21} of 200nm thick Py tunable slow wave structure with different DC current.

magnetic anisotropy is very small as it is one of the three components contributing to magnetic anisotropy. The highest change in the saturation magnetization among all the experments performed in this dissertation was calculated as 5.33% which is also negligible. It can be concluded that the change of the magnetic anisotropy as well as the FMR frequency in this dissertaion is due to the external magnetic field mainly, not because of the Joule heating effect.

For device B, the 100nm and 200nm thick Py was used for the same device and Py dimensions as described in the previous section. The FMR frequency for 100nm thick Py was observed at 3.6GHz. The results for device B were characterized and analyzed at a center frequency of 2GHz which is smaller than the FMR frequency. Table 3.3 summarizes the value of inductance for 100nm thick Py enabled slow wave structure for different DC current applications. At 2GHz, the value of inductance per unit length increased from 1067.2nH/m to 1162.7nH/m for the introduction of 100nm thick micro-patterned Py which was decreased to 1138.5nH/m by the application 50mA of DC

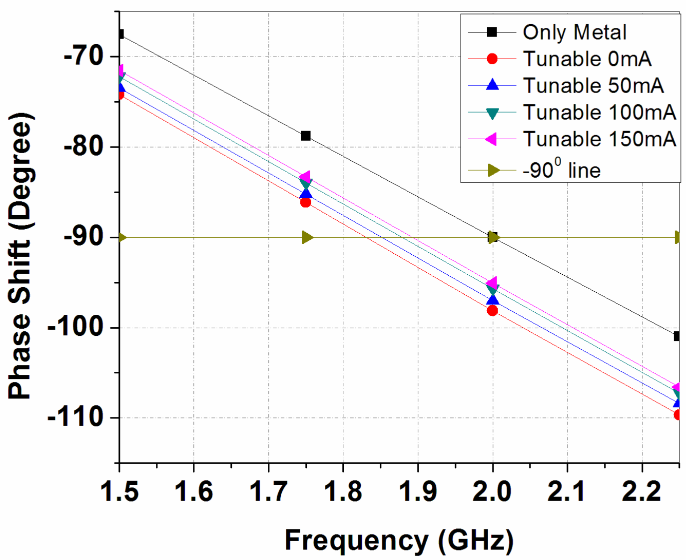

Figure 3.17: Measured phase shift of 100nm thick micro patterned Py tunable SWS.

Table 3.3: Values of Inductance for the device without and with 100nm Py under different DC bias current

Frequency (GHZ)	**1**	**1.25**	**1.5**	**1.75**	**2**	**2.25**	**2.5**
Regular (nH/m)	1071.7	1066.1	1061.9	1066.5	1067.2	1065.2	1065.2
Tunable at 0mA (nH/m)	1199.3	1184.5	1172.8	1167.8	1162.7	1151.5	1144.9
Tunable at 50mA (nH/m)	1183.4	1167.5	1151.3	1144.8	1138.5	1127.5	1120.8
Tunable at 100mA (nH/m)	1132.0	1122.6	1113.9	1112.3	1109.2	1104.2	1101.4
Tunable at 150mA (nH/m)	1103.9	1108.7	1094.3	1095.1	1094.2	1090.4	1089.4

Table 3.4: Values of Inductance for the device without and with 200nm Py under different DC bias current

Freq. (GHZ)	**1**	**1.25**	**1.5**	**1.75**	**2**	**2.25**	**2.5**
Regular (nH/m)	1071.7	1066.1	1061.9	1066.5	1067.2	1065.2	1065.2
Tunable at 0mA (nH/m)	1256.2	1244.9	1229.1	1211.6	1193.0	1162.3	1140.0
Tunable at 50mA (nH/m)	1237.8	1228.3	1212.9	1196.4	1180.7	1152.3	1131.0
Tunable at 100mA (nH/m)	1213.0	1202.6	1187.5	1169.4	1151.5	1123.4	1103.7
Tunable at 150mA (nH/m)	1171.0	1161.2	1145.3	1130.4	1117.2	1099.2	1088.3

current. The decrease of inductance value is because of the decrease in anisotropy field due to external magnetic anisotropy. The application of different DC current value resulted in different inductance value as summarized in Table 3.3 while the capacitance value was almost fixed throughout the experiments.

The equivalent quarter wavelength for the slow wave structure in device B was calculated as 4.97mm at 2GHz. The phase shift created by an equivalent λ/4 slow wave structure was calculated and analyzed. The 4.97mm long, 100nm thick Py enabled slow

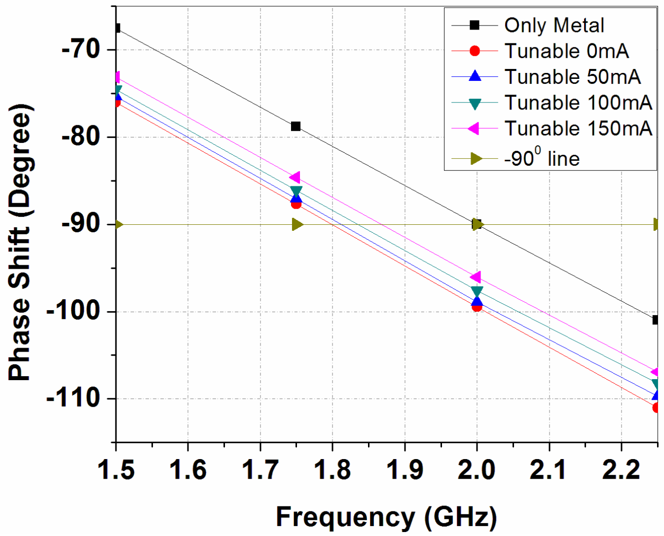

Figure 3.18: Measured phase shift of 200nm thick micro patterned Py tunable SWS.

wave structure demonstrated a 90° phase shift at 1.84GHz which was tuned to any value in between 1.84GHz to 2GHz by suitable selection of DC current. Figure 3.17 shows the phase shift created by a 4.97mm long tunable slow wave structure with different DC current.

The S-parameters of the 200nm thick Py enable slow wave structure is presented at Figure 3.16. The FMR frequency was observed at 3.2GHz which is decreased due to increase in eddy current loss and shape anisotropy in the ferro-magnetic thin film. The thicker Py increased the inductance value from 1067.2nH/m to 1193nH/m. The inductance increment was higher than the 100nm thick Py structure due to increase of the magnetic material per unit volume while the capacitance value was also almost fixed. With the application of 50mA, 100mA and 150mA DC current, the inductance value changed to 1180.7nH/m, 1151.5nH/m and 1117.2nH/m. Application of 200nm thick micro patterned Py on top of equivalent 4.97mm long slow wave structure changed the center frequency from 1.80GHz to 2GHz as shown in Figure 3.18. Suitable selection of DC current can result in any center frequency in between the frequency range. The insertion loss due to the introduction of ferro-magnetic thin film is less than 0.3dB throughout the dissertation. The use of patterned Py in place of continuous thin film decreased the eddy current through it which kept the insertion loss at a very low value.

3.10 SUMMARY

Nano-patterned Py enabled slow wave structure demonstrated an FMR frequency of 6.3GHz and increased the inductance density from 879nH/m to 961nH/m (i.e. 9.3 %.). At 4GHz, the simple slow wave structure decreased the equivalent quarter wavelength from 7.43mm to 4.19mm while the ferro magnetic thin film decreased the size from 4.19mm to 4.01mm. The tuning of the center frequency from 3.81GHz to 4GHz was achieved by applying 150mA DC current.

The 200nm thick micro-patterned Py increased the inductance density from 1067.2nH/m to 1193nH/m (i.e. 13%) while FMR frequency was reduced to 3.2GHz. The well designed slow wave structure decreased the equivalent length from 14.86mm to 4.97mm at 2GHz which was reduced further to 4.70mm using Py. The tunable slow wave structure showed the tuning of the frequency by any value in between 1.80GHz to 2GHz (i.e. 10%) using DC current.

CHAPTER 4

FERRO-ELECTRIC THIN FILM INTEGRATION FOR CAPACITANCE TUNING

In the previous chapter, the ferro-magnetic thin film was integrated to increase and tune the inductance value only. The capacitance of SWS needs to be increased to keep the characteristics impedance the same with improved slow wave effect and frequency tuning range. In this chapter, the ferro-electric thin film, Lead Zirconium Titanate (PZT) has been integrated in the slow wave structure. The fundamental concepts of capacitance in a co-planar waveguide structure have been discussed followed by the ferro-electric thin film property. As the PZT is normally used in the vertical structures, several issues e.g. adhesion and the lattice mismatching were observed during the implementation of PZT in the co-planar devices which were solved by using a non-conducting intermediate layer of silicon di-oxide. The growth of the ferro-electric thin film has been described with all the necessary conditions. Due to the thermal mismatch of the different layers, an optimization was necessary to achieve a well crystallized thin film with no cracks; crystallization steps have been modified to achieve the goal. The crystallization, phase and orientation of the ferro-magnetic thin film have been confirmed by X-ray diffraction. The ferroelectric thin film has been selectively etched from the sample to fabricate the PZT tunable slow wave structure. The measured results have shown the increment and tuning of the capacitance. In this chapter, both the ferro-magnetic and ferro-electric thin films have been integrated simultaneously to demonstrate wider tuning range and higher slow wave effect while keeping the characteristics impedance almost same.

4.1 CAPACITANCE

The capacitance of a coplanar wave guide transmission line is given by the following formula [90]:

$$C = 2\varepsilon_0(\varepsilon_{r1} - 1)\frac{K(k_1)}{K(k_1{}')} + 4\varepsilon_0\frac{K(k_0)}{K(k_0{}')} \qquad 4.1$$

$$k_1 = \frac{sinh(\frac{\pi S}{4h_1})}{sinh\{\frac{[\pi(S+2W)]}{4h_1}\}} \qquad 4.2$$

$$k_1{}' = \sqrt{1 - k_1{}^2} \qquad 4.3$$

$$k_0 = \frac{S}{S+2W} \qquad 4.4$$

$$k_0{}' = \sqrt{1 - k_0{}^2} \qquad 4.5$$

where k_1, $\mathrm{k}_1{}'$, k_0 and $\mathrm{k}_0{}'$are the modulus of complete elliptic integral,

S is the width of the signal conductor,

W is the gap in between signal and ground conductor.

h_1 is height of the substrate.

ε_{r1} is the real dielectric constant of the substrate.

ε_0 is the dielectric constant in free space.

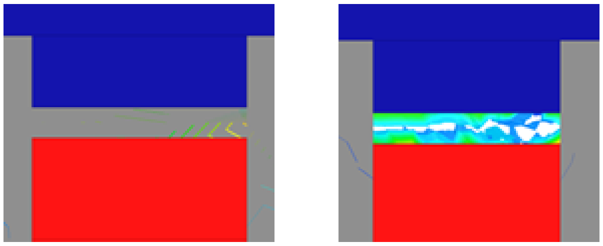

Figure 4.1: Simulated electric field with and without ferro-electric thin film.

All the parameters except the relative di-electric constant are dependent on device dimensions i.e. a material with high and changeable dielectric constant is necessary to implement a compact and tunable slow wave structure.

4.2 FERRO-ELECTRIC THIN FILM

The property of spontaneous electric polarization that can be changed by the application of an external electric field is called the ferro-electricity [104, 105]. Ferroelectric materials possess a polarization even in absence of an electric field which makes it different from the dielectric and para-electric materials. The dielectric constant of the ferro-electric material is very high as the electric field passes through

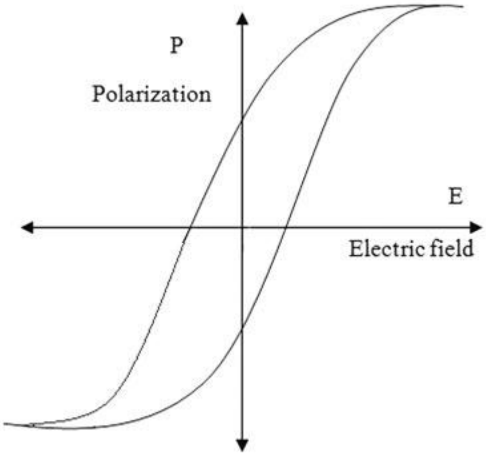

Figure 4.2: Polarization curve of a typical ferro electric material. [106]

them more easily. They demonstrate the ferro-electricity only below a certain temperature (Curie temperature, T_c) which is well above the room temperature. The polarization curve of a ferro-electric material has a very high and changeable slope i.e. high and tunable dielectric constant is expected. The electric field can be generated by applying a particular voltage, V in between a fixed distance, d.

$$E = \frac{V}{d} \tag{4.2}$$

If the gap in between the signal and ground is kept fixed, electric field changes with the applied voltage. The change in electric field results in different polarization which changes the dielectric constant value i.e. different capacitance value. Thus, the ferro-electric thin film has the potential to improve the slow wave effect by increasing the C value and make the device workable at different frequencies by changing the thin film property with the help of electric field. There are many ferro-electric materials like Barium Strontium Titanate (BST), Lead Zirconium Titanate (PZT), Barium Titanate, Lead Titanate etc.

4.3 PZT (LEAD ZIRCONIUM TITANATE)

Lead Zirconium Titanate (PZT) is a ferroelectric, intermetallic, inorganic compound which changes the electric polarization with the application of an electric field. The chemical formula of PZT is $Pb[Zr_xTi_{1-x}]O_3$ ($0 \leq x \leq 1$) and dielectric constant is extremely large when x=0.52 [107]. Higher number of allowable domain states is mainly responsible for the increased piezoelectric response and polarizing efficiency near x=0.52. At morphotropic phase boundary, all the 6 possible domain states from the tetragonal phase and the 8 possible domain states from the rhombohedral phase are equally favorable energetically [108]. Dielectric constant of PZT can be as high as 980 near DC [109] and this value depends on the thickness of the film, crystal orientation, material composition, frequency etc.

4.4 GROWTH OF LEAD ZIRCONIUM TITANATE

There are several methods to grow the ferro-electric thin film, PZT: Chemical Vapor Deposition (CVD), Molecular Beam Epitaxy (MBE), Sol-gel Chemical Method and Sputtering etc. In this dissertation, the sol gel method was used to grow the PZT thin film as it is the most convenient and less expensive method. In sol-gel method, the solution was prepared first followed by the growth of an intermediate layer as needed. The PZT solution was spun over the sample and rotated at a very high speed to make a uniform layer. Two stages of temperature treatment are required: pyrolysis and crystallization.

4.4.1 SOLUTION PREPARATION

A 1.169ml Zirconium (IV) propoxide solution was added into 10ml 2-methoxyethanol (2-MOE) and the solution was stirred for 30 minutes. A 1.731ml of Titanium (IV) isopropoxide was added into the solution then and stirred for another 30 minutes. A 3.359gm of Lead (II) acetate trihydrate was added into the solution and stirred for 1 hour at 150^{o}C. Heating and stirring was very important for the solubility of the different chemicals. Hot plate was turned off and solution was stirred for 2 more hours without any heating to make the solution ready. This ratio of chemical solution was intended for a PZT thin film thickness of 100nm. In order to increase the thickness, the ratio of the solvent (2-MOE) will have to be decreased. The solution was kept in a dark bottle so that the light can't cause any decomposition. If the solution is not precipitated, it can be used for several times. It's better to heat and stir the solution to increase the solubility in case it is made long time ago.

4.4.2 GROWTH OF SiO_2

In case of sol gel PZT growth, the most common practice is to use $LaNiO_3$ (LNO) or Platinum (Pt) as an intermediate layer between the PZT and the substrate. It helps to grow a good quality PZT thin film as the crystal orientation of LNO or Pt matches mostly with that of PZT. All the applications which used LNO or Pt are the vertical devices where higher conductivity of LNO and Pt adds further advantages of low loss. The intended tunable slow wave structure in this dissertation is a coplanar device where higher conductivity of LNO and Pt will short the signal and ground conductor which will reflect back the original signal. This shortcoming restricted the use of LNO or Pt as an

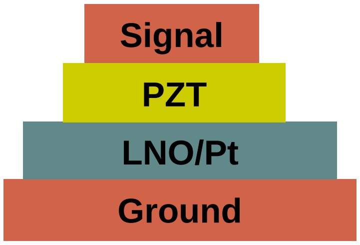

Figure 4.3: Conventional growth of PZT thin film on top of conducting LNO or Pt.

Figure 4.4: Growth of PZT on non-conducting SiO_2 for coplanar devices.

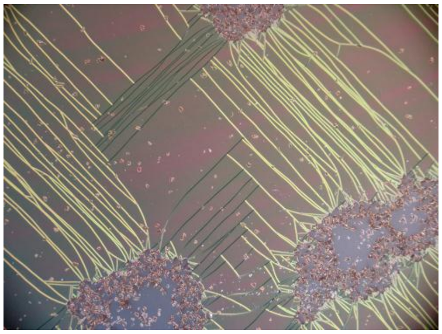

Figure 4.5: Adhesion problem of PZT on direct silicon substrate.

intermediate layer in between Si and PZT. Attempts were taken to grow the PZT on top Si directly, however, due to poor adhesion between Si and PZT an additional SiO_2 layer had to be grown. SiO_2 was grown by rapid thermal annealing (RTA) process where the temperature was kept at 1000°C for 10min. The thickness of SiO_2 was measured using Filmetrics and found to be approximately 15nm-20nm. The outcome was improved while maintaining the insulating characteristics.

4.4.3 CRYSTALLIZATION OF PZT

The solution was spun over the sample and rotated at 6000rpm for 1min where high rotating speed helped the thin film to grow uniformly. The sample was kept inside

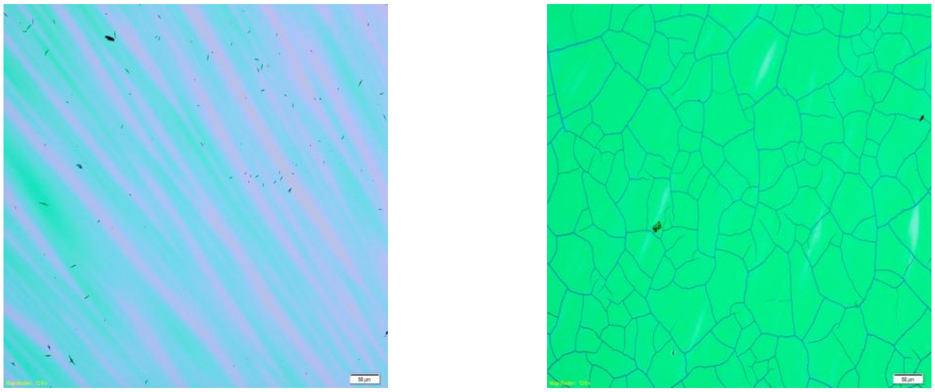

Before Crystallization After Crystallization

Figure: 4.6 Image showing the cracks on PZT thin film.

the oxidation chamber at 300°C for 20min which is called the pyrolysis; the step where moisture comes out of the thin film before crystallization. The temperature of the furnace was taken to 650°C for crystallization after pyrolysis. During the crystallization process, the continuous flow of O_2 gas was maintained; approximately 20 bubbles per minutes. If the flow of O_2 was too high, temperature would not go up; the thin film would not be crystallized. On the other hand if the flow of the O_2 was too low, the required PZT{$Pb[Zr_xTi_{1-x}]O_3$} would not be formed as it would be more conducting which is unexpected. After the crystallization at 650°C, some cracks were found on the thin film as shown in Figure 4.6 which occurred due to mismatch of the constituent materials, e.g. the thermal co-efficient of PZT, SiO_2 and Si are 11×10^{-6} /°C, 5×10^{-7} /°C, 2.6×10^{-6} /°C respectively. As apparent, PZT expands 4 times more than Si and 20 times more than SiO_2 which resulted in cracks. The sudden increase of temperature is responsible for the cracks. Therefore, the temperature was decreased to 500°C that showed no cracks. However, the XRD spectrum showed the material was not crystallized as shown in Figure

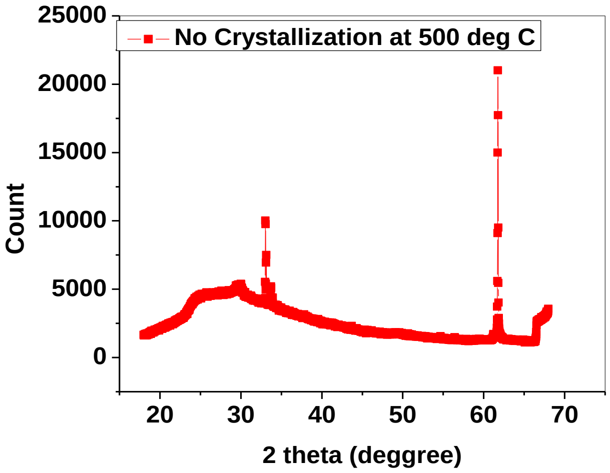

Figure 4.7: X-ray diffraction of PZT thin film after crystalizing at 500°C.

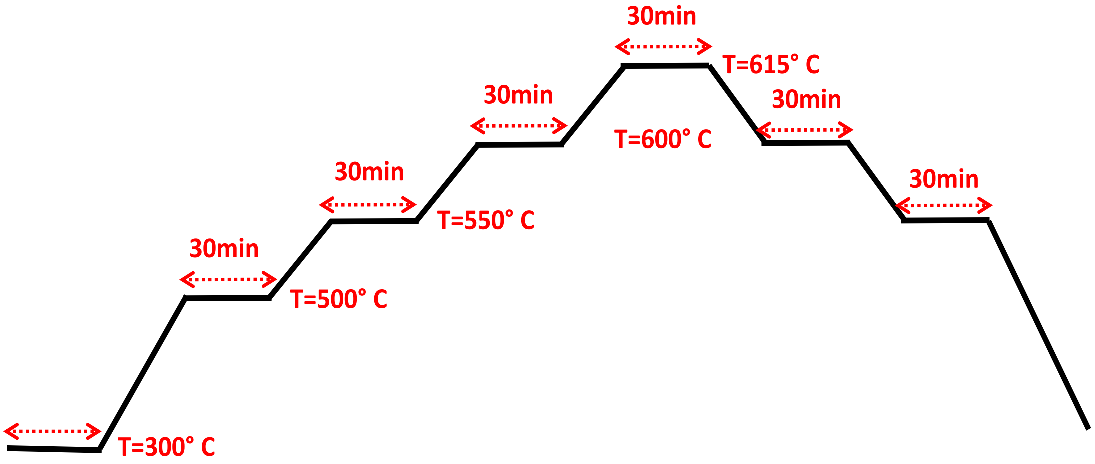

Figure 4.8: The temperature profile during the crystallization of PZT.

4.7[110,111].

The temperature was varied step by step to achieve the crystallization while maintaining no cracks. The temperatures were set at 500^{o}C, 550^{o}C, 615^{o}C, 550^{o}C, 500^{o}C, 300^{o}C and 0^{o}C while a wait time of 30 minutes were maintained after achieving each temperature step. Finally the sample was let to cool down over night after setting the temperature at 0^{o}C. The gradual treatment of heat during the crystallization process ended up with a sample having no cracks as shown in Figure 4.11.

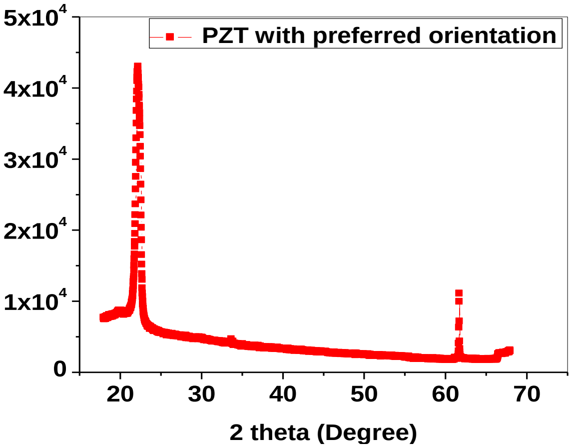

Figure 4.9: X-ray diffraction of PZT thin film after crystalizing at 615^{o}C.

X-ray diffraction (XRD) analysis was performed to reveal the crystallographic structure of the films and their preferred orientation. The XRD pattern of the PZT shown in Figure 4.9 illustrates that the PZT thin film was crystallized in the perovskite phase, and no pyrochlore phase was detected. Moreover, the presence of the strong peak at 22.4^o indicates that the film has a (100) preferential orientation. Perovskite is the type of orientation which shows ferro-electricity property whereas pyrochlore phase doesn't show the ferro-electricity; moreover pyrochlore phase is conducting in nature. As per composition, the PZT grown by the sol-gel method was approximately $Pb[Zr_{0.65}Ti_{0.35}]O_{3.}$

4.5 PZT ENABLED TUNABLE SLOW WAVE STRUCTURE

The ferro-electric thin film, PZT was used along with simple slow wave structure to make a compact tunable slow wave structure. The higher dielectric constant of PZT increased the capacitance value i.e. slow wave effect is improved. Moreover, the electric field created by DC voltage was applied across the PZT to change the property of the thin film which changed the capacitance value while keeping the inductance same. The change of capacitance value demonstrates the function of the device at multiple frequencies.

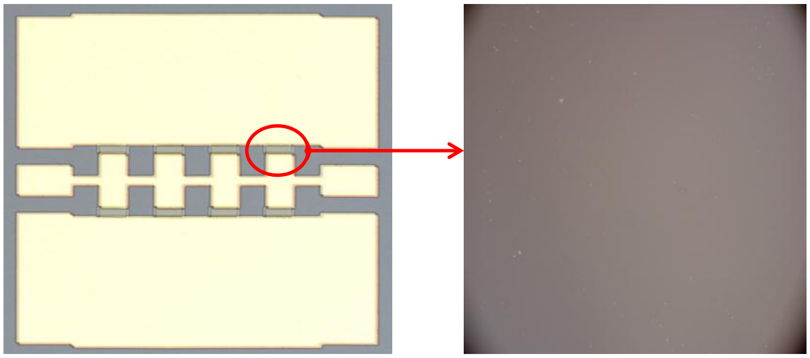

Figure 4.10: Tunable SWS enabled with PZT and zoom in view of PZT film.

4.6 FABRICATION AND EXPERIMENTAL SETUP

PZT thin film was grown on high resistivity Si Substrate keeping SiO_2 as an intermediate layer. PZT was selectively etched and kept between wide signal conductor and ground only. The solution of BHF: HCl: NH_4Cl:H20 (1:2:4:40) was used to etch the thin film and the etch rate was determined to be 60nm/minute [112]. Simple SWS of 0.9µm-1µm thick Gold (Au) was fabricated using optical lithography as shown in Figure 4.10. The dimensions of slow wave structure are as follows:

Total length of the device, L is 450µm,

Width of the narrow conductor section, W_1 is 5µm,

Width of the wide conductor section, W_2 is 10µm,

Length of the narrow conductor section, L_1 is 50µm,

Length of the wide conductor section, L_2 is 50µm,

Gap in between ground conductors, G is 150µm,

Thickness of the metal, t is 1µm

Dimension of the PZT thin film was measured to be as 50µm × 25µm × 110nm.

SOLT calibration was performed to de-embed the losses from cables, connectors

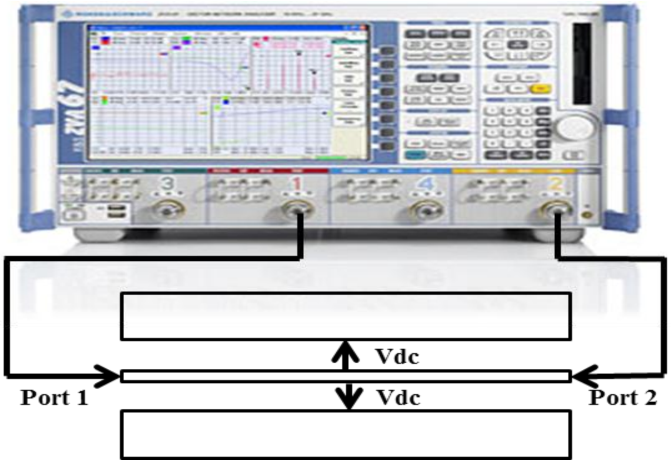

Figure 4.11 Measurement set up showing the external DC voltage application.

Table: 4.1 Inductance values of regular and tunable SWS at different external DC voltage

Frequency (GHZ)	2	2.5	3	3.5	4	4.5	5
Regular (nH/m)	897	887	882	879	879	879	877
Tunable at 0V (nH/m)	907	898	890	890	891	892	890
Tunable at 10V (nH/m)	904	893	888	887	890	889	885
Tunable at 20V (nH/m)	904	891	885	885	888	888	884

Table: 4.2 Capacitance values of regular and tunable SWS at different external DC voltage

Frequency (GHZ)	2	2.5	3	3.5	4	4.5	5
Regular (pF/m)	252	252	252	252	251	252	252
Tunable at 0V (pF/m)	269	267	266	264	262	261	260
Tunable at 10V (pF/m)	260	259	258	257	255	254	254
Tunable at 20V (pF/m)	257	256	256	254	253	253	253

and probes. External DC voltage using bias-tee was applied across the signal and ground conductors. As the electric field created by DC voltage applies across the PZT thin film, it polarizes the thin film and changes the capacitance value.

4.7 RESULTS AND DISCUSSION: PZT ENABLED TUNABLE SWS-SET 1

The inductance and capacitance value of regular and PZT tunable slow wave structure is summarized in Table 4.1 and 4.2 respectively. A very small change of inductance is noticeable due to the introduction of the PZT as it is not ferromagnetic material; moreover the application of DC voltage didn’t change the inductance value either. In Figure 4.13, the phase shift of regular and tunable SWS at different bias voltage is demonstrated. A simple slow wave

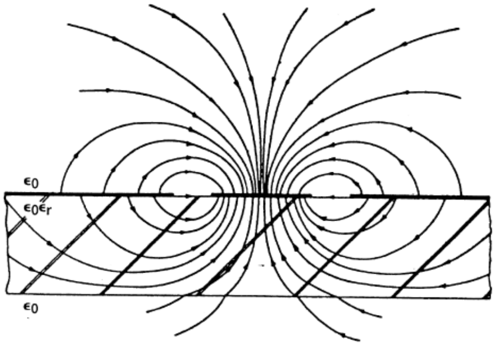

Figure 4.12: Electric field distribution in a CPW transmission line [90].

structure reduced the quarter wavelength size from 7.43mm to 4.19mm at 4GHz without any thin film. The application of PZT shifted the center frequency of an equivalent 4.19mm long line from 4GHz to 3.90GHz by increasing the capacitance value from 251nF/m to 262nF/m which shows the promise of this structure as tunable slow wave element. However, the capacitance increment achieved by this structure is only 4.38% while the frequency tuning range was limited to only 2.5%.

The small change in the capacitance value or frequency tuning can be a result of several factors. PZT was a little bit over etched during patterning by wet etching;

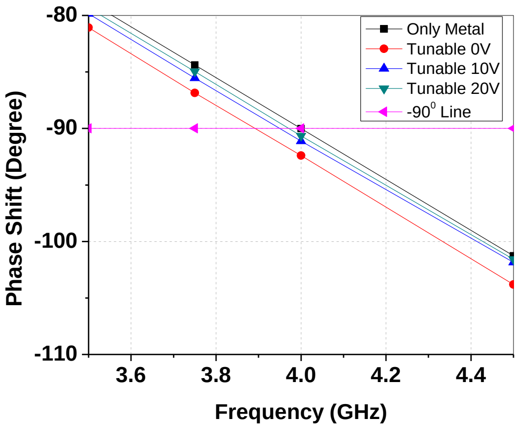

Figure 4.13: Measured phase shift of regular and PZT tunable SWS with different DC voltage.

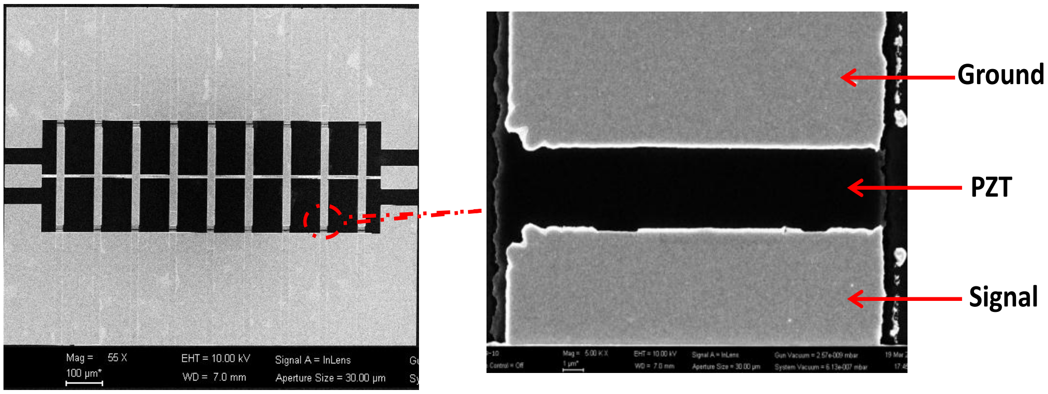

Figure 4.14: SEM photo of SWS with reduced gap between wide signal and ground (left) and zoom in view (right).

polycrystalline PZT material can be an issue also. Electric field required to reach the saturation is approximately 40KV/mm; however, the applied electric field due to this designed structure was 1KV/mm as 20V DC was applied across 20µm gap. Moreover, in case of a CPW transmission line, most of the electric field goes through the air as shown in Figure 4.12.

4.7.2 RESULTS AND DISCUSSION: PZT ENABLED TUNABLE SWS-SET 2

As the large gap between the wide signal conductor and ground was the main reason to achieve low capacitance value and small tuning range, another set of PZT tunable slow wave structure has been introduced as shown in Figure 4.14. The total length of the SWS was 936µm while the length and width of the narrow section was 84µm and 7µm respectively. The length of the wide section was kept as 20µm while the width is varied according to the requirement. The gap between the wide signal conductor and extended ground was kept as 1µm. A thinner (100nm) metal has been used at the edge to fabricate the small gap between two metals (wide signal and ground) and the PZT is kept below the wide section responsible for capacitance. The goal of this design was to

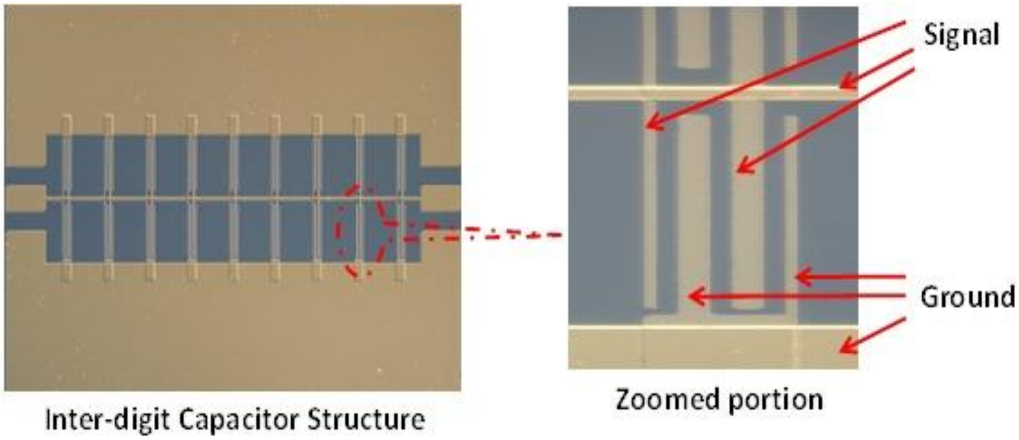

Figure 4.15: Microscope photo of SWS employing interdigitated capacitor structure at wide sections.

increase the linkage of E-field between signal and ground. This effort resulted in 7% increment in capacitance value which is better than 4.38% achieved by the previous set of structures.

4.7.3 RESULTS AND DISCUSSION: PZT ENABLED TUNABLE SWS-SET-3

The wide section which contributes to capacitance value was changed in third set of structures to increase the capacitance by a big margin. The length and width of the

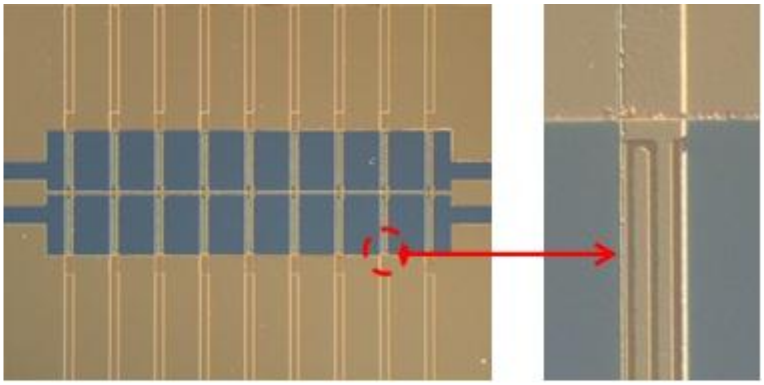

Figure 4.16: Microscope photo of PZT tunable SWS employing interdigitated capacitor structure with PZT beneath the metal and zoom in view (right).

Table 4.3: Capacitance values of SWS CPW with PZT under different DC voltage

Frequency (GHZ)	**1**	**1.25**	**1.5**	**1.75**	**2**	**2.25**	**2.5**
Regular (nF/m)	.608	.603	.596	.593	.591	.589	.588
Tunable at 0V (nF/m)	.976	.912	.858	.824	.817	.804	.801
Tunable at 2V (nF/m)	.854	.836	.818	.815	.797	.799	.784
Tunable at 5V (nF/m)	.778	.780	.771	.763	.764	.760	.756
Tunable at 10V (pF/m)	.678	.677	.677	.672	.678	.679	.678
Tunable at 15V (nF/m)	.662	.662	.663	.663	.665	.664	.663

narrow section was 70µm and 7µm respectively while the total length of the wide section was 20µm. This wide section was modified as Interdigitated Capacitor (IDC) where the width of the signal and ground was 5µm and the gap between them was 3µm. Figure 4.15 shows the IDC structure where more E-field reaches from the signal to ground conductor i.e. capacitance is increased by a big margin. Moreover, more E-field will pass through the PZT to tune the frequency of the structure during the application of DC voltage.

The ferro-electric thin film PZT was grown by sol-gel method and selectively etched to keep below the wide section only in a SWS utilizing interdigitated capacitor as shown in Figure 4.16. Table 4.3 summarizes the capacitance value per unit length from 1GHz to 2.5GHz as the micro-patterned Py allowed the operation until the 3.2GHz by ferro-magnetic resonance. The capacitance per unit length increased from 0.591nF/m to 0.817nF/m by the application of PZT which was changed further by different DC voltage as shown in Table 4.4. The capacitance is defined by the change of the electric charge for a corresponding change in voltage. The change of voltage also takes place very fast as the frequency goes higher. The electric charge can’t respond as quickly as the voltage is changed which results in low capacitance value at higher frequency as evident from the list. The quarter wave length of a transmission was reduced from 14.86mm to 4.97mm at 2GHz using slow wave methods without any thin film which was further reduced to 4.23mm by applying the thin film.

The frequency, at which a 4.97mm long slow wave structure creates a 90° phase shift, is termed as center frequency. The center frequency was shifted from 2GHz to 1.75GHz with the introduction of PZT as the ferro-electric thin film increases capacitance. The application of different DC voltage changed the property of the thin film i.e. different capacitance value was measured. The center frequency was tuned to any value between 1.75GHz to 2GHz by suitable selection of DC voltage. The ferro-electric thin film enabled slow wave structure demonstrated slow wave improvement and wider tuning of frequency.

Table 4.4: Capacitance values and equivalent quarter wave length of SWS with PZT under different DC voltage

Structures	**C (pF/m)**	**λ/4 (mm)**
SWS with no PZT	591	4.97
PZT tunable SWS at 0V	817	4.23
PZT tunable SWS at 2V	797	4.28
PZT tunable SWS at 5V	764	4.37
PZT tunable SWS at 10V	678	4.64
PZT tunable SWS at 15V	665	4.69

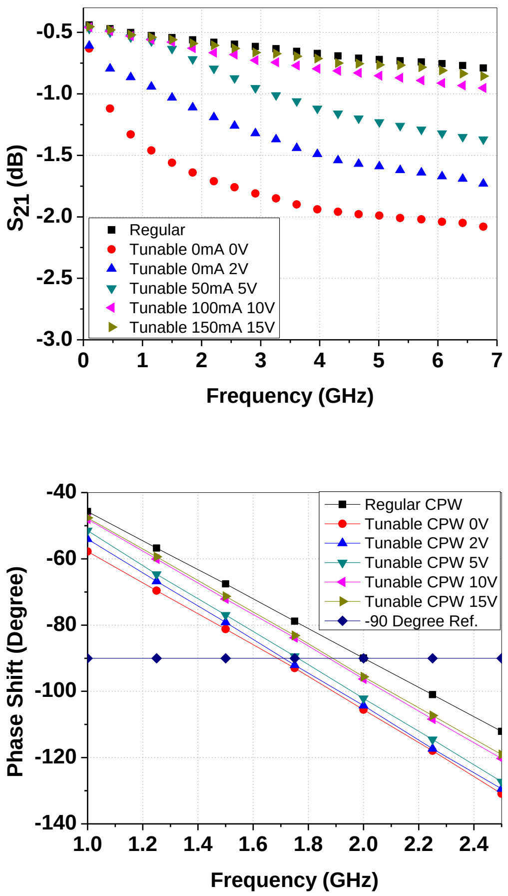

Figure 4.17: Measured S-parameter (top) and phase shift (bottom) of PZT enabled slow wave structures under different DC voltages.

4.8 BOTH PERMALLOY AND PZT ENABLED SLOW WAVE STRUCTURE

The tunability of SWS was demonstrated by using Py and PZT separately in the previous sections where Py has changed the L value and PZT has changed the C value. Characteristics impedance of the structure was also changed from the reference value which can be addressed by tuning both L and C value simultaneously thereby decreasing the mismatch loss of the total circuit board. Moreover, the slow wave factor and frequency tuning range will be even higher.

4.9 FABRICATION AND MEASUREMENT SETUP

Two different sets of Py and PZT tunable slow wave structures were fabricated e.g. SET-1 and SET-2. The PZT and metal were patterned the same way as described in previous section. The ferro magnetic thin film, Py was deposited on top of narrow portioned signal line using DC magnetron sputtering. Py was patterned in the sub micrometer range by E-beam lithography and micrometer range by optical lithography. The devices were measured and results were evaluated in the same way as described in previous section. Two separate power sources have been used here in order to tune both L and C. One current source is connected in between two signal probes and made it work as a current source which applied the current through the signal conductor thereby changing the L value. Another voltage source was connected in between the signal and ground probe of the same port which applied DC voltage across the PZT and tuned the C value. Figure 4.18 shows a simultaneous demonstration of DC voltage and DC current application in the SWS. Implementation of both the DC current and DC voltage is performed simultaneously for the first time.

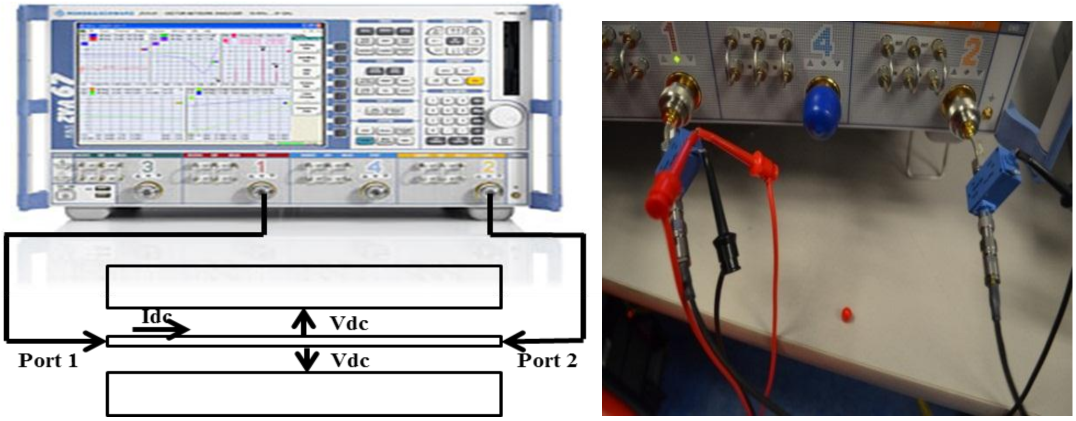

Figure 4.18: Measurement set up and bias tee connection showing the application of both external DC voltage and DC current.

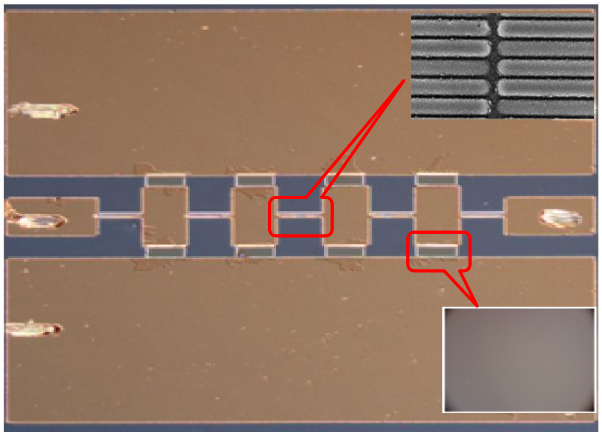

Figure 4.19: Fabricated CPW structure with thin films and the zoom-in view of patterned Py (upper inset) and PZT (lower inset).

4.10 RESULTS AND DISCUSSIONS: SET-1

For SET-1, simple SWS with a total length of 450µm was fabricated. The length of narrow and wide conductor section was 50µm each while the width of the narrow and signal conductors was 5µm and 110µm. The gap in between two ground conductors was kept at 150µm. The dimension of the Py bars was 10µm×150nm×100nm while the gap in between the Py bars was 100nm. The nano patterning of Py showed an FMR frequency of 6.3GHz. The PZT was etched and kept in between the wide portioned signal conductor

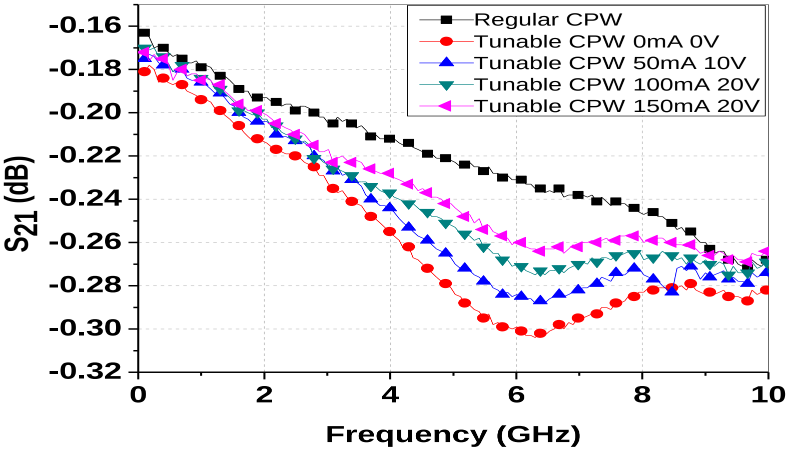

Figure 4.20: Measured S-parameter of tunable transmission line under different DC bias currents.

Table: 4.5 Inductance values of regular and tunable SWS under different external DC current and voltage

Frequency (GHZ)	**2**	**2.5**	**3**	**3.5**	**4**	**4.5**	**5**
Regular L (nH/m)	897	887	882	879	879	879	877
Tunable L at 0mA 0V(nH/m)	993	983	981	972	961	957	949
Tunable L at 150mA 20V(nH/m)	944	933	929	918	909	903	898
Tunable L at 100mA 20V(nH/m)	955	943	940	931	920	914	908
Tunable L at 50mA 10V(nH/m)	979	967	965	956	947	941	935

Table: 4.6 Capacitance values of regular and tunable SWS at different external DC current and Voltage

Frequency (GHZ)	**2**	**2.5**	**3**	**3.5**	**4**	**4.5**	**5**
Regular C (pF/m)	252	252	252	252	251	252	252
Tunable C at 0mA (pF/m)	265	264	264	262	262	261	261
Tunable C at 150mA 20V(pF/m)	257	256	256	254	253	251	249
Tunable C at 1000mA 20V(pF/m)	257	256	256	255	253	251	249
Tunable C at 50mA 10V(pF/m)	260	259	258	257	255	252	250

and ground only. The approximate shape of the PZT after etching was 50μm × 25μm while the thickness of the PZT was measured to be around 110nm by Dektak surface profilometer. A total image of the tunable SWS is presented at Figure 4.19.

The measured S-parameters as shown in Figure 4.20 demonstrate an FMR frequency of 6.3GHz. The measured inductance and capacitance value of regular and tunable SWS for different conditions are summarized in Table 4.5 and 4.6. Figure 4.21 shows the phase shift and impedance of the tunable SWS at different conditions.

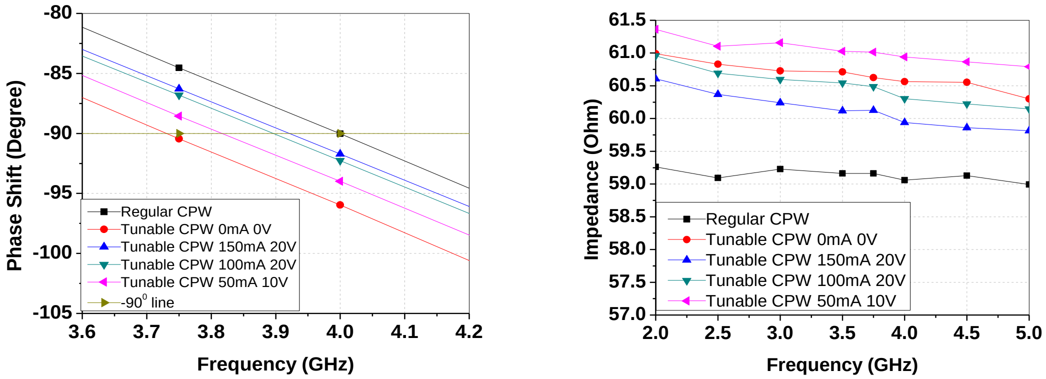

Figure 4.21: Phase shift and impedance of both Py and PZT tunable SWS with applied DC voltage and DC current.

Increment of both L and C value is noticeable as two separate thin films have been used. Inductance is increased from 879nH/m to 961nH/m which C is increased from 251pF/m to 262pF/m at 4GHz due to the introduction of thin films only. Using the slow wave methods, the size of a quarter wavelength line is reduced from 7.43mm to 4.19mm. That means an equivalent 4.19mm long transmission line creates a 90^{o} phase shift at 4GHz; the center frequency is shifted from 4GHz to 3.73GHz by using both Py and PZT. Simultaneous introduction of 150mA DC current and 20V DC voltage shifted the frequency to 3.94GHz as both L and C decreases with the increase of current and voltage. Suitable selection of current and voltage can result in any frequency in between 3.73GHz to 4GHz.

The implemented transmission line can also be used to design impedance matching network also as shown in Figure 4.21. Different selection of DC current and DC voltage can result in wide variety impedance value. The higher tuning range of L and C value can provide wider tuning range of impedance in an impedance matching network. Table 4.7 summarizes all the values of inductance, capacitance, characteristics impedance, equivalent quarter wavelength frequency for selected DC bias conditions.

Table 4.7: Summary of results for Py and PZT tunable SWS (Set-1)

Structure	**V_{DC} (V)**	**I_{DC} (mA)**	**L nH/m)**	**C (pF/m)**	**Z_0 (Ω)**	**Freq. (GHz)**
Regular CPW	0	0	897	253	59.5	4
Tunable CPW	0	0	961	262	60.5	3.75
Tunable CPW	10	50	947	258	60.6	3.8
Tunable CPW	20	100	920	254	60.3	3.9

4.10.2 RESULTS AND DISCUSSIONS: SET-2

For SET-2, the 200nm thick micro patterned Py was used on top narrow portioned signal conductor. The width and length of the narrow signal section was 7μm and 84μm while the length of wide signal conductor was 20μm. The dimension of the micro patterned Py was 10μm × 17μm which ensured the operation until 3.2GHz. In case of wide conductor section, the same interdigitated capacitor (IDC) structure was used as described in the previous chapters. Figure 4.22 shows a complete tunable slow wave

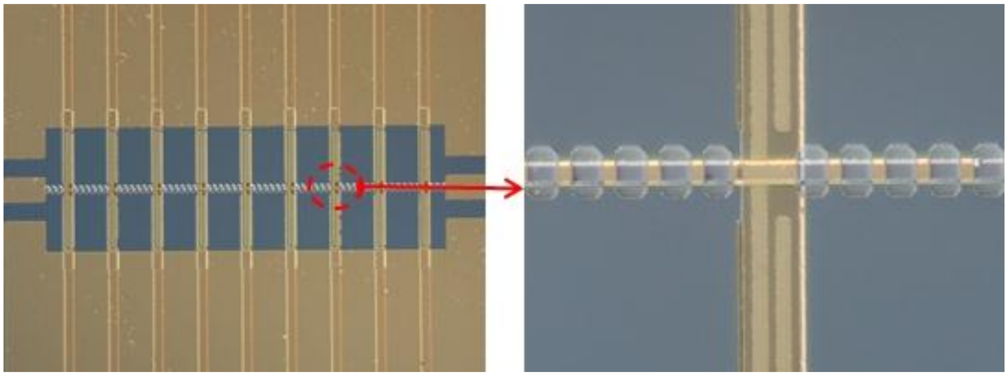

Figure 4.22: Microscope photo of tunable slow wave structure with both Py and PZT for SET-2.

Table 4.8: Summary of results for Py and PZT tunable SWS (Set-2)

Structure	**L** (nH/m)	**C** (nF/m)	Z_0 (Ohm)	**λ/4** (mm)
Regular CPW	1067.2	0.591	42.48	4.98
Tunable at 0mA 0V	1209.7	0.816	38.49	3.98
Tunable at 0mA 2V	1203.1	0.798	38.83	4.03
Tunable at 50mA 5V	1169.3	0.764	39.12	4.18
Tunable at 100mA 10V	1139.5	0.678	40.99	4.50
Tunable at 200mA 15V	1118.0	0.664	40.62	4.63

structure employing both micro-patterned Py and PZT.

The measured S-parameters of the Py and PZT tunable slow wave structure demonstrate an FMR frequency of 3.2GHz as shown in Figure 4.23. The inductance per unit length increased from 1067.2nH/m to 1209.7nH/m and the capacitance per unit length increased from 0.591nF/m to 0.816nF/m at 2GHz. The equivalent quarter wavelength was reduced from 14.86mm to 4.97mm using slow wave methods which are further decreased to 3.98mm using two different thin films. All the calculations are made based on the equivalent length of 4.97mm and the frequency at which this equivalent length creates a 90° phase shift is termed as center frequency. The introduction of the Py and PZT thin films reduced the center frequency to 1.5GHz. The suitable selection of DC voltage and current can result in any center frequency between 1.5GHz to 2GHz (i.e. 25% tuning). The characteristics impedance value was fixed between 38.49Ω to 42.48Ω for the introduction of the thin film and DC sources.

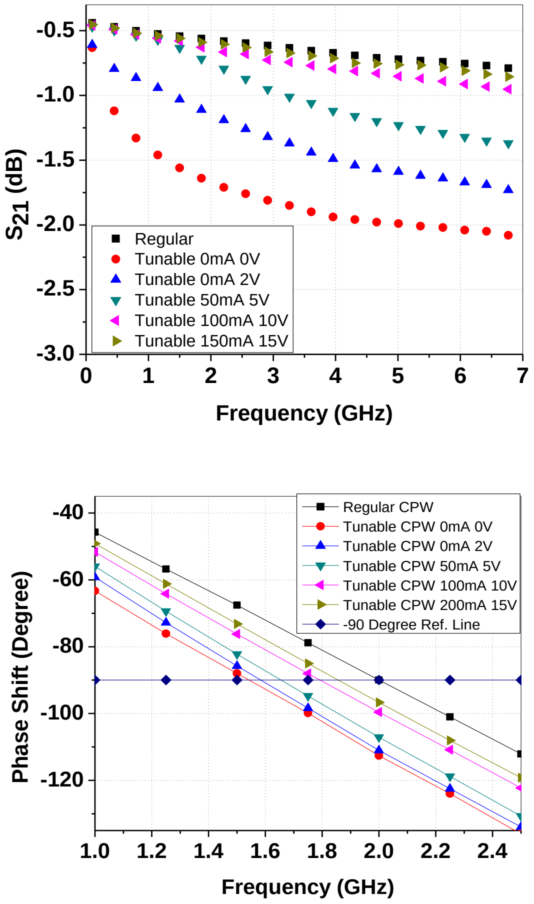

Figure 4.23: Measured S-parameter and phase shift of tunable slow wave structure with both Py and PZT for SET-2.

4.11 SUMARRY

In this chapter, the slow wave effect and frequency tuning of the PZT tunable slow wave structure have been investigated and demonstrated using three sets of tunable structures. The simple slow wave structure using PZT between large signal-ground gap showed an increment of capacitance by 4.38% and frequency tuning by 2.5%. With the help of microwave theory and techniques, the equivalent quarter wavelength was decreased from 7.43mm to 4.19mm at 2GHz while the PZT decreased the size further from 4.19mm to 4.11mm. The capacitance increment by 7% was achieved decreasing the gap in between signal and ground to 1µm. The IDC type structure showed a big increment of capacitance value to 36% which tuned the center frequency by 15% (2GHz-1.7GHz). These slow structures decreased the equivalent quarter wavelength from 14.86mm to 4.23mm using slow wave techniques and PZT.

Finally, the two sets of slow wave structure are implemented with both the Py and PZT. For the first set of results, an inductance increment of 9.32%, capacitance increment of 4.38% and a frequency tuning of 6.75% (4GHz to 3.73GHz) has been achieved. In terms of the size, it reduced the quarter wavelength from 7.43mm to 4.20mm by microwave techniques and 4.20mm to 3.93mm by the thin films. Final set of tunable slow wave structure utilizing thick micro patterned Py and PZT with IDC increased the inductance and capacitance density by 13.3% and 36%. It represented a frequency tuning of 25% (2GHz to 1.5GHz) where both the DC current and DC voltage is used simultaneously to change the property of the ferro-magnetic and ferro-electric thin film. For a particular frequency, the equivalent quarter wavelength is reduced from 14.86mm to 4.97mm and 4.97mm to 3.98mm by microwave techniques and thin films respectively. Throughout the experiments, the characteristics impedance of the structure is kept fixed between 38.49Ω to 42.48Ω which is very essential from design perspective.

CHAPTER 5

APPLICATION OF THE THIN FILMS IN RADIO FREQUENCY COMPONENTS

In this chapter, the ferro-magnetic thin film has been implemented in various passive components which were one of the main motivations of this dissertation. The ferro-magnetic thin film has been first utilized to suppress the electromagnetic noise of the system. The frequency of the suppression peak has been tuned to different frequencies changing the Permalloy shape and the DC current applied. The results of the noise suppressor have been compared and analyzed with the conventional noise suppressors. In the next section, a detailed study of the Permalloy patterning has been presented to evaluate the use of Py in microwave devices. The width, gap, length and thickness of the Py have been changed to observe their effect on FMR frequency and inductance density which are the deciding factors in microwave applications. A tunable band pass filter has been implemented with both Py and PZT where the pass band frequency is tuned by the ferro-magnetic thin film. The design of the filter has been modified to make it compatible for thin film application. The tunable meander line inductor with various turns has also been designed, fabricated and characterized. Py has been deposited and patterned on top of the meander line inductor to increase the inductance density until 4.9GHz. Inductance density of the meander line inductor has been tuned by applying different DC bias current.

5.1 DC CURRENT TUNABLE NOISE SUPPRESSOR

One of the main problems towards the modern technological advancement is the electromagnetic noise. A noise suppressor is a transmission line that passes the signal in the designed frequency range and stops the higher order noise harmonics. Py exhibits ferro magnetic resonance (FMR) which can be used to absorb noise. However, introduction of Py affects pass band characteristics and return loss. A well designed noise suppressor should have minimum loss at the pass band, a tunable stop band, very low reflected signal and the least phase shift of transmitted signal. Figure 5.1 demonstrates the simple function of a noise suppressor. The noise suppressor demonstrated in this dissertation has the unique properties of using nano-patterned Py thin film. It has made been made to absorb noise at 6GHz without the application of any external magnetic field. Moreover, the patterned Py results in less L increment which ensure less mismatch

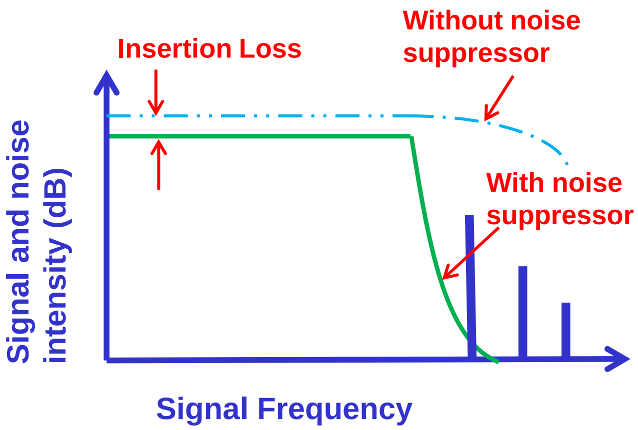

Figure: 5.1: Function of a noise suppressor.

loss compared to conventional noise suppressors. Eddy current slows through the thin film which results in higher pass band loss. Here, less eddy current flow is ensured to minimize the pass band loss.

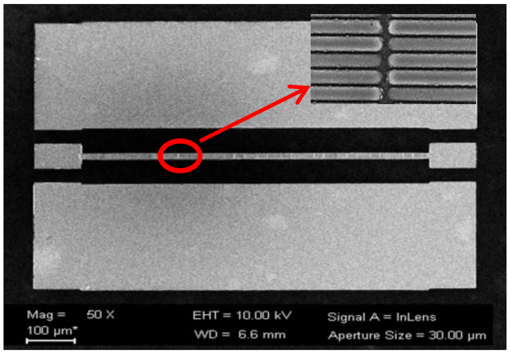

Figure: 5.2: SEM photo of a fabricated noise suppressor. Inset shows patterned Py. Length of the Py bars is 10µm. Width and gap in between Py bars are varied. CPW length, width of signal line and signal-ground gap are 750µm, 5µm and 72.5µm, respectively. Scale bar is different for inset image.

5.1.1 FABRICATION AND EXPERIMENT: NOISE SUPPRESSOR

The noise suppressors were fabricated using gold structures on top of a high resistivity (10 kΩ-cm) silicon substrate with 0.9µm Au. Py (100nm) was then deposited on top of the signal line using DC magnetron sputtering. Chromium of 5–10nm was used as an adhesion layer between Au and Py. Using e-beam lithography, Py with different widths and gaps was patterned across the center line of CPW. Figure 5.2 shows a complete noise suppressor with patterned Py. The S-parameters were measured with a ZVA67 network analyzer in the frequency range of 0.1-10 GHz. DC current was applied using bias tee in between two RF probes as shown in Figure 3.11 and 3.12. Standard SOLT calibration was used to de-embed the losses from cables, connectors and RF probes. All the dimensions of both metal and Py was provided in the Figure 5.2.

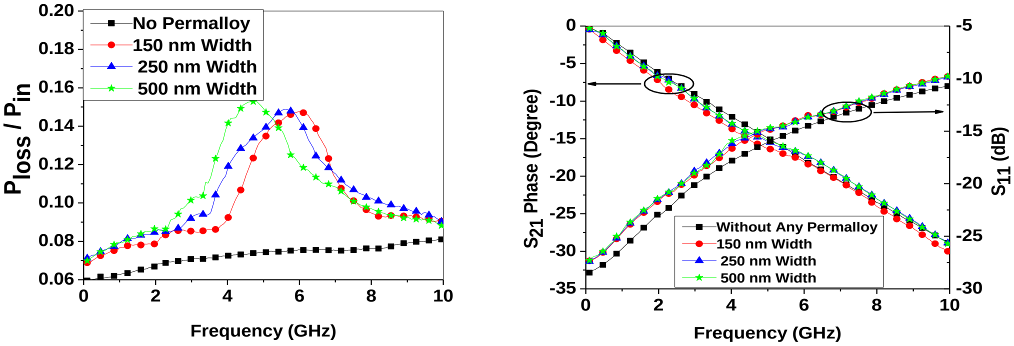

Figure 5.3: Power loss (P_{loss}/P_{in}) [a] as well as S_{21} Phase (degree) and S_{11} (dB) [b] of regular structure and noise suppressors of different aspect ratios. Length and Gap in between Py bars are 10µm and 100nm, respectively. CPW length, width of signal line and signal-ground gap are 750µm, 5µm and 72.5µm, respectively.

5.1.2 RESULTS AND DISCUSSION: NOISE SUPPRESSOR

The power loss in Figure 5.3(a) calculated from the measured S-parameters $(\frac{P_{loss}}{P_{in}} = 1 - (|S_{21}|^2 + |S_{11}|^2))$ as well as S_{21} (Phase) and S_{11} (dB) Figure 3.13(b) are presented. A demagnetizing field from a device containing the highest aspect ratio produces an easy axis of magnetization along the long axis, and thus higher FMR frequency is achieved. Power loss of around 15% for the noise at different frequencies has been reported in Figure 5.3(a). Pass band loss of 1.5%, signal distortion of less than 2^0 and additional return loss of only 2dB is generated by the introduction of Py.

The power loss of a noise suppressor depends on both the length of the CPW structure and the thickness of the ferromagnetic material. A comparison of approximately calculated P_{loss} per mm for various CPW structures is summarized at Table 5.1. Lower power loss (~19.4%) is reported in this section, this is because the thickness of Py is much smaller compared with the earlier results. Significant increase of P_{loss} with thicker ferromagnetic material is achievable as shown in Table 5.2. Use of longer length and thicker ferromagnetic material in our demonstrated noise suppressor can achieve higher

Table: 5.1 Comparison of P_{loss} for different CPW noise suppressors

T-Line Length (mm)	**Material and Thickness (nm)**	**Reported Loss**	**Ins. Loss Calc. (per mm)**	**P_{loss} Calc. (per mm)**	**Ref.**
15	CoNbZr (1µm)	3 dB	.2 dB	4.5 %	[61]
	CoZrO (1µm)	4 dB	.266 dB	5.9 %	
	CoPdAlO (2µm)	17 dB	1.13 dB	22.9 %	
15	CoFeAlO (1µm)	20 dB	1.33 dB	26.37 %	[57]
15	CoFeAlO (100nm)	5 dB	.33 dB	7.31 %	
15	CoNbZr (1µm)	30 dB	2 dB	36.9 %	[60]
15	CoNbZr (2µm)	50 dB	3.33 dB	53.5 %	
15	CoPdAlO (2µm)	55 dB	3.66 dB	56.94 %	
17	CoNbZr (100nm)	2.5 %	.00646 dB	.148 %	[113]
17	CoNbZr (1µm)	15 %	.042 dB	1.00 %	
.75	NiFe (100nm)	15 %	.941 dB	19.4 %	Our

Table: 5.2 Variation of P_{loss} with thickness of ferromagnetic materials

Change of Thickness	**Change of Loss**	**Material**	**Ref.**
100nm to 1µm	8% to 40 %	CoNbZr	[61]
100nm to 1µm	7.31% to 26.31%	CoFeAlO	[57]
1µm to 2µm	36.9 % to 53.5 %	CoNbZr	[60]
100nm to 1µm	2.5% to 15%	CoNbZr	[113]

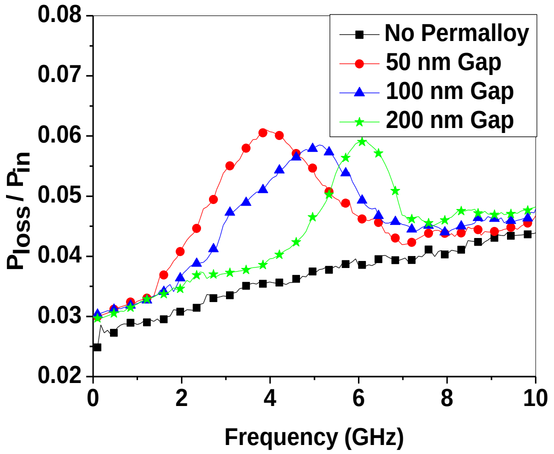

Figure 5.4: Power loss (P_{loss}/P_{in}) of regular structure and noise suppressors with different gap in between Py bars is shown. Length, width and ground-signal gap of CPW are 500µm, 10µm and 50µm, respectively. Dimension of Py bar is 10µm X 250nm.

noise suppression. Inductance per unit meter is changed by only 8%. This ensures low phase variation as well as minimum reflection loss compared to conventional noise suppressors. Patterned ferromagnetic material keeps the eddy current through it at minimum level to enhance pass band characteristics.

The effect of gaps between the Py bars is investigated while keeping the dimension of Py structures fixed. Power loss [Figure 5.4] is depicting the change of stop band frequency with the gaps between bars. The magnetized shape produces magnetic charges at the surface. This surface charge distribution acts as a source of a magnetic field, defined as demagnetizing field (H_D). It works in opposition to the magnetization that produces it. With the increase of gap, the demagnetizing field decreases which in turn increases the shape Anisotropy field. The increase of Anisotropy field increases FMR frequency as per Kittel’s equation.

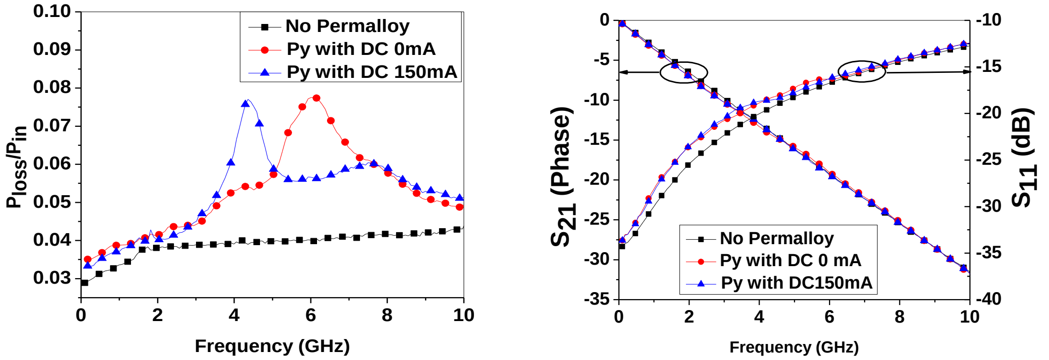

Figure 5.5: Power loss (P_{loss}/P_{in}) [a] as well as S_{21} Phase (degree) and S_{11} (dB) [b] of regular structure and noise suppressors with different DC bias current. Dimension of Py bars is 10µm X 150nm while gap in between them is 100nm.Length, width and ground-signal gap of CPW are 750µm, 10µm and 72.5µm, respectively.

Finally, suppress band tuning is demonstrated by applying external DC current from 0mA to 150mA along the signal line. The magnetic field generated here is working along the hard axis. By introducing 150mA DC current, the noise suppression frequency is changed from 6GHz to 4.3GHz as shown in Figure 5.5(a) while the pass band loss is also negligible. Tuning of attenuation dip by using DC current has two advantages over applying external magnetic field as previously reported. Since Ampere's fields and Joule heating effects due to the applied DC current contribute to the shift of FMR, less ampere field is needed for the same amount of FMR shift. Furthermore, it is more convenient to apply DC current than external magnetic field in a practical circuit board. The introduction of Py and DC current results in 2^0 differential phase shift and 3dB extra return loss [Figure 5.5b]. This shows the promise of our noise suppressor.

5.1.2 CONCLUSION: NOISE SUPPRESSOR

A tunable noise suppressor at gigahertz frequency is designed, implemented and demonstrated. The stop band frequency of the designed noise suppressor is tuned by

1.21GHz with different aspect ratios of Py patterns, and 1.9GHz tuning has been achieved with different gaps in between Py patterns. Most convenient and efficient external tuning by applied DC current has shown 1.7GHz tuning range of the noise suppression frequency. Compared with the structure without Permalloy patterns, the designed noise suppressor shows better performance with 1.5% of additional pass band loss, 2^0 phase variation and 3dB more return loss.

5.2 A COMPREHENSIVE STUDY OF PERMALLOY PATTERNING FOR RF APPLICATIONS

Permalloy has been patterned on coplanar waveguide (CPW) structures with different width, gap and thickness. FMR frequency and inductance density are extracted from the measured s-parameters. A 60nm thick permalloy has been patterned with a dimension of 440nm×10μm while the gap between the Py bars is varied from 130-300nm, results show an increment of FMR frequency from 4.5 to 5GHz with larger gap due to less coupling, and reduction of inductance density from 642nH/m to 627nH/m. Permalloy is also patterned and investigated with the same gap between patterns while their width varied from 440 to 470nm, measured results have shown that the inductance density increases from 633nH/m to 645nH/m and FMR frequency reduces from 4.80 to 4.60GHz. Permalloy with different thickness (60-200nm) is also studied, a significant increase in inductance density (13.5%) has been achieved with thicker film but the FMR frequency reduces with increasing eddy current loss. In addition, DC current effect on the inductance density and FMR frequency has been studied. This section also provides a

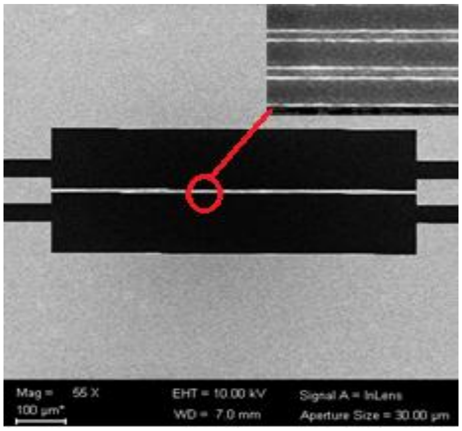

Figure 5.6: Structure showing nano-patterning of 70nm Py enabled transmission line.

new way to increase the inductance density by changing configuration and location of Permalloy patterns. The insertion loss due to the introduction of Py is less than 0.05dB.

5.2.1 FABRICATION AND EXPERIMENT: PERMALLOY STUDY

A simple coplanar wave guide (CPW) transmission line was fabricated on top of high resistivity (10kΩ-cm) Silicon substrate. The reason of choosing the high-R substrate was to reduce the dielectric loss. The thickness of the Gold (Au) structures is kept at 1µm. The ferro-magnetic thin film, Py with different thickness (60-200nm) was deposited on top of the fabricated CPW structure using DC magnetron sputtering. The Ar gas pressure of the deposition chamber was 2.1mT and temperature was 300K. The deposition rate was measured to be around 0.023nm/s. 5nm Chromium was used as an adhesion layer between Au and Py. No external magnet was used during this deposition process. The Py was patterned with different dimensions in the nano-meter range using E-beam lithography in order to introduce shape anisotropy. Figure 5.6 shows a CPW structure with nano-patterned Py. Py was also deposited with different thickness while keeping the dimension fixed at 10µm× 17µm.

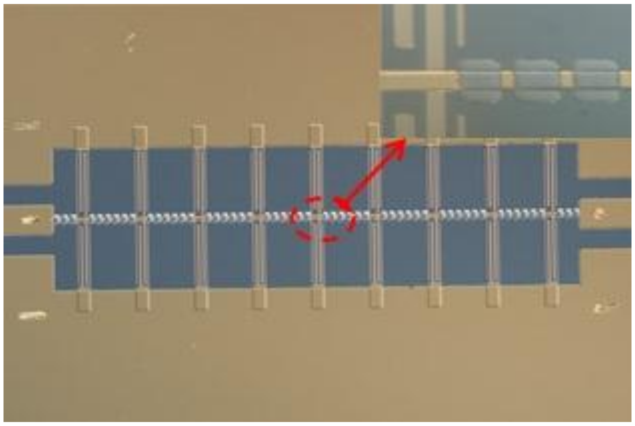

Figure 5.7: Structure showing micro patterning for thick Py inside the red circle.

Figure 5.7 shows a slow wave structure (SWS) having patterned Py with a thickness of 100nm and 200nm. The motivation for choosing the SWS was to decrease the size. Finally, the S parameters were measured with a Rhode & Schwarz ZVA67 network analyzer and the FMR frequency was analyzed. In order to de-embed the losses coming from cables, connectors and probes, standard SOLT calibration is performed. Equations were used to extract inductance density of the prospective RF components. A DC current was applied along the signal line using bias tee in order to tune the inductance density and FMR frequency of the patterned ferro-magnetic thin films.

5.2.2 RESULTS AND DISCUSSIONS: PERMALLOY STUDY

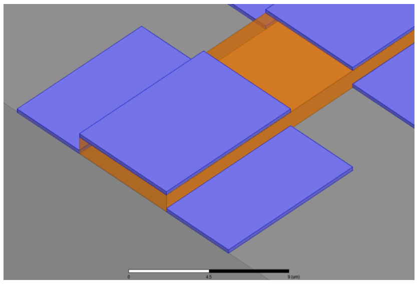

Figure 5.8: Py patterned beside the signal line

Table 5.3: Inductance per unit length and FMR frequency for different gap in between the Py bars

Structure	Width of Py bar (nm)	Inductance (nH/m)	FMR (GHz)
Only Metal	N/A	615	N/A
Gap 300nm	440	627	4.97
Gap 223nm	440	633	4.79
Gap 130nm	444	642	4.51

Table 5.4: Inductance per unit length and FMR frequency for different width of Py bars

Structure	Gap (nm)	L (nH/m)	FMR (GHz)
Only Metal	N/A	615	0
Width 440nm	223	633	4.79
Width 470nm	230	645	4.60

Table 5.5: Inductance per unit length and FMR frequency for different thickness of Py bars. The dimension for 60nm thick Py is 440nmX10µm while the dimensions for 100nm and 200nm Py are same as 17µmX10µm

Thickness of Py	Inductance increment (nH/m)	FMR (GHz)
60nm	4.87%	4.60GHz
100nm	9.03%	3.6GHz
200nm	13.5%	3.2GHz

Table 5.3 shows the inductance density and the FMR frequency of the different Py patterns for different gap in between the Py bars. Its shows the inductance density

increases with decreasing gap as the magnetic material per unit volume is increased. But it ended up with a reduction of the FMR frequency from 4.97GHz to 4.51GHz. This reduction of FMR frequency is responsible for the coupling introduced from nearby Py bars. Table 5.4 shows the properties of the patterns having different widths while the gap in between them is kept fixed. It shows an increment of Inductance density and decrement of FMR frequency with the increase of the width. The increase of width decreased the aspect ratio which in turn increases the demagnetizing field acting along the easy axis of magnetization i.e. FMR frequency is reduced.

The inductance density is increased with the thickness of thin film as well as the distribution. Figure 5.8 shows a way where Py is distributed between signal and ground line. It increases the inductance density from 4.87% to 9.03% (100nm) and 13.5% (200nm). But the FMR is decreased as the eddy current loss is increased due to thickness ferro magnetic material. A non-conducting layer of AlN in between Py layers could decrease the FMR frequency.

A DC current which is most feasible in a practical circuit board is applied along the signal line of the passive component in order to tune the L value and FMR frequency.

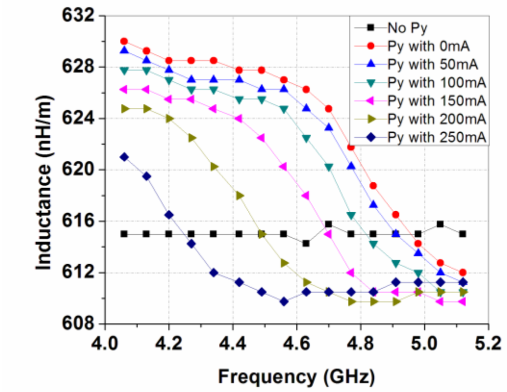

Figure 5.9: Extracted inductances of SWS with Py patterns under different DC current.

The external magnetic field created by this DC current applies along the hard axis of the magnetic moment. It changes the inductance density value and FMR frequency as shown in Figure 5.9. The hard axis magnetization decreases the magnetization along the easy axis, i.e. the shape anisotropy is decreased. This decreases both the L value and FMR frequency.

5.2.2 CONCLUSION: PERMALLOY STUDY

A complete study of the patterned Py is presented with different widths, gaps and thickness. The inductance density and FMR frequency which is the main factors in radio frequency applications are investigated with practical results. The effect of DC current application on patterned Py is also shown in order to tune the radio frequency components. This section provides a solution to the high frequency, tunable, low loss passive component utilizing the ferro magnetic thin films.

5.3 TUNABLE RF BANDPASS FILTER WITH NANO-PATTERNED PERMALLOY

A well designed and fabricated coplanar waveguide (CPW) center frequency tunable bandpass filter (BPF) at 4GHz enabled with patterned Permalloy (Py) thin film has been demonstrated. The tunable BPF can be tuned with only DC current without any external magnetic bias field. Electromagnetic band gap resonators structure BPF is adopted so that external DC current can be applied to the input and output of the filter for tuning of Py permeability. Special configurations of resonators with multiple narrow parallel sections have been considered for larger inductance tunability. 70nm thickness Py thin film patterned as bars with the dimension of 10μm×444nm is deposited to the top

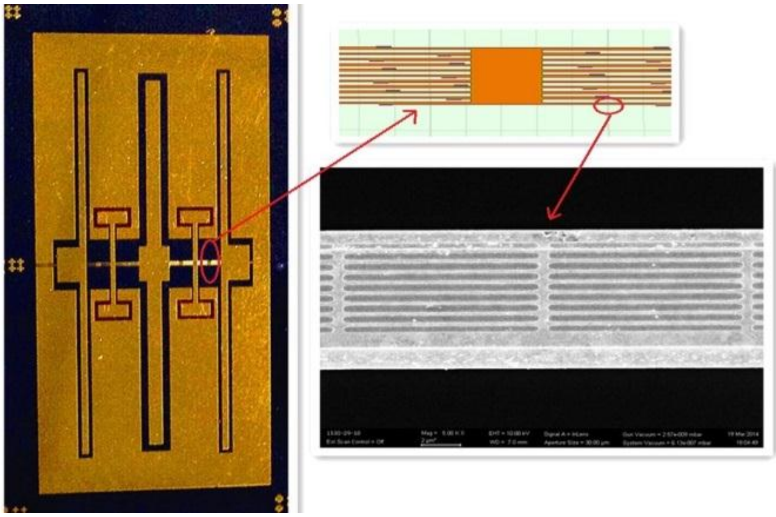

Figure 5.10: Microscope photo of band pass filter (left) and zoom in view of parallel narrow sections with patterned Py thin film.

of the multiple narrow parallel sections without any extra area and components being introduced. The measurement results show that the center frequency could be tuned from 4GHz to 4.02GHz when the DC current was applied from 0mA to 400mA.

5.3.1 FABRICATION AND EXPERIMENT: BAND PASS FILTER

The tunable BPF was fabricated on high resistivity (10kΩ-cm) silicon substrate to reduce the dielectric loss. The metal was gold (Au) and the thickness was kept 1μm. Electromagnetic band gap (EBG) resonators structure BPF [114, 115] is adopted which is based on several considerations. First, compared with conventional inductor direct coupling CPW band pass filter [116], EBG structure is more compact, the size of which is reduced by 60.5% since the length of EBG resonator is far smaller than the conventional half wavelength resonator. Due to the reduction of the length of the resonators, the total amount of patterned Py bars deposited on the top of the resonators is greatly reduced, so the fabrication time and complexity is significantly decreased. Second, from the equivalent circuit of EBG resonator, the inductance of the BPF is

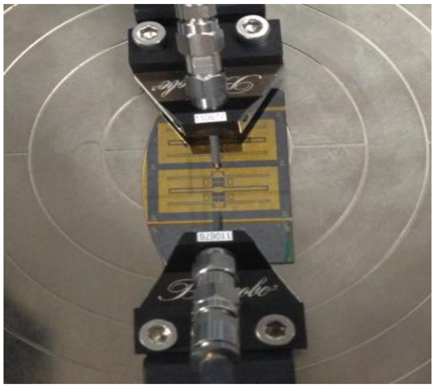

Figure 5.11: Device under test on the probe station.

mainly contributed by the central resonating CPW sections with the electrical length of θ_{21} [35]. Thus when patterned Py thin film is deposited on the top of those resonating sections, the inductance of the BPF is affected maximally so that larger inductance tunability can be acquired. Third, unlike the normal capacitive-coupled resonators structures, EBG resonator BPF can provides a direct path for DC current from the input to the output. DC current can be applied directly at the two ends of the BPF to tune the center frequency with the magnetic field generated towards the hard axis of magnetic moment. In order to make sure all the DC current can only go through and concentrate on EBG resonators with Py thin film on it, all the inductive-coupled CPW stubs have been replaced with open CPW stubs by adding quarter-wavelength CPW lines.

Multiple narrow parallel sections have been configured for central resonating sections of EBG resonators with the width of each section being 7µm. The maximum Ampere's fields generated by DC currents can be estimated with Ampere's law $\mathrm{H_{dc}} = \mathrm{I}/2\mathrm{w}$, where I is the DC current, w is the width of each narrow section. From the equation, the smaller the width of the section is, the larger the Ampere's field towards the hard axis of magnetic moment is generated; thus more tunability is acquired.

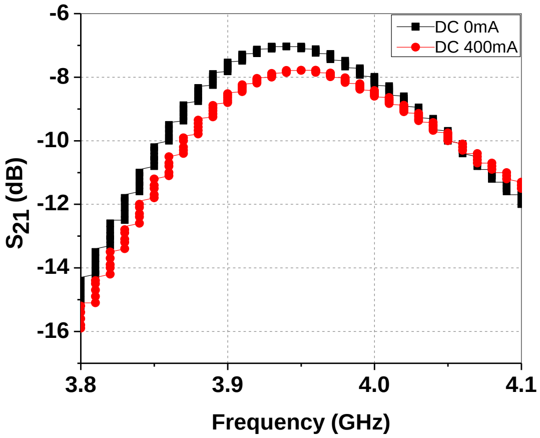

Figure 5.12: Measured S_{21} under different DC current applied.

The Py thin film was deposited on the top of each narrow section of fabricated EBG resonators of the tunable BPF using DC magnetron sputtering and liftoff procedure. The thickness of Py thin film was 70nm. The ferromagnetic (FMR) frequency of Py thin film should be larger than the BPF working frequency; thus Py thin film was patterned as slim bars in the nano-meter range with the dimension of 10μm×444nm using E-beam lithography to introduce shape anisotropy to increase anisotropy field H_{ani} so that FMR frequency can be increased according to Kittel equation.

$$f_r=\frac{\gamma}{2\pi}\sqrt{(H_{bias}+H_{ani}+(N_y-N_z)4\pi M_s)(H_{bias}+H_{ani}+(N_x-N_z)4\pi M_s)}$$

where γ is the gyromagnetic ratio, H_{bias} is the bias field, N_x, N_y and N_z are demagnetization coefficients, and $4\pi M_s$ is the saturation magnetization. The FMR frequency has been increased up to 6GHz. The S parameters are measured with a Rhode & Schwarz ZVA67 network. Standard SOLT calibration is performed to de-embed the influence coming from cables, connectors, bias tees and probes. DC current is applied with the use of bias tee along with the cable to the input and output of the tunable BPF to tune the center frequency.

5.3.2 RESULTS AND DISCUSSIONS: BAND PASS FILTER

Figure 5.12 shows the center frequency shift of the tunable BPF. The center frequency is 4GHz when there is no DC current being applied. As the DC current is increased to 400mA, the center frequency moves to 4.02GHz. DC current can generate an external magnetic field along the direction of hard axis of magnetic moment, which can rotate M perpendicular to the wire axis and decrease the anisotropy field which can rotate M parallel to the wire axis so that permeability of Py thin film is decreased consequently and the total inductor of the BPF is decreased, resulting in the increment of the center frequency of BPF. Different tunable range can also be achieved with selective pattern conFigureurations and thickness of Py thin film.

The insertion loss of the tunable filter is large up to 6.5dB. The Py thin film can introduce some loss due to the eddy current going through it even though we use discontinuous patterned Py thin film and eddy current has been decreased largely. Another part of the loss comes from the radiation loss. Due to the displacement of CPW short stubs by CPW open stubs, the electric field in the gaps between CPW open stubs and ground radiate to the air so radiation loss is introduced. Impedance mismatch also contributes to the total insertion loss. There is a 0.5dB increment of insertion loss when 400mA DC current is applied. Due to the existence of the metal resistance, when DC current is applied, the temperature of the metal will increase, which in turn augments the metal resistance so that extra insertion loss is introduced.

5.3.3 CONCLUSIONS: BAND PASS FILTER

A patterned Permalloy thin film enabled coplanar waveguide tunable band pass filter has been designed and fabricated. The Permalloy thin film is patterned as slim bars and is deposited on the top of the EBG resonators of the band pass filter. Special configuration of parallel narrow sections of EBG resonators has been utilized to acquire a larger tenability. The center frequency of the band pass filter is tuned only by DC current applied to the input and out- put of the band pass filter. Frequency shift from 4GHz to 4.02GHz is obtained when DC current is increased from 0mA to 400mA, respectively.

5.4 TUNABLE RF INDUCTORS USING NANO PATTERNED PERMALLOY THIN FILM

In this section, tunable RF meanderline inductors are designed and implemented with nanoscale patterned Permalloy thin film for high and variable inductance density. FMR frequency of Permalloy film is increased by creating its shape anisotropy field through nanoscale patterning. High resistivity Si substrate is adopted to decrease the substrate loss. Inductor is implemented with a 60nm thick Permalloy deposited on the top of meander line, permalloy film is patterned with dimension of 440nm×10μm to increase the shape anisotropy field which in turn increases the FMR frequency. Compared to a meanderline inductor, the inductance density has been increased by 20% by using patterned permalloy.

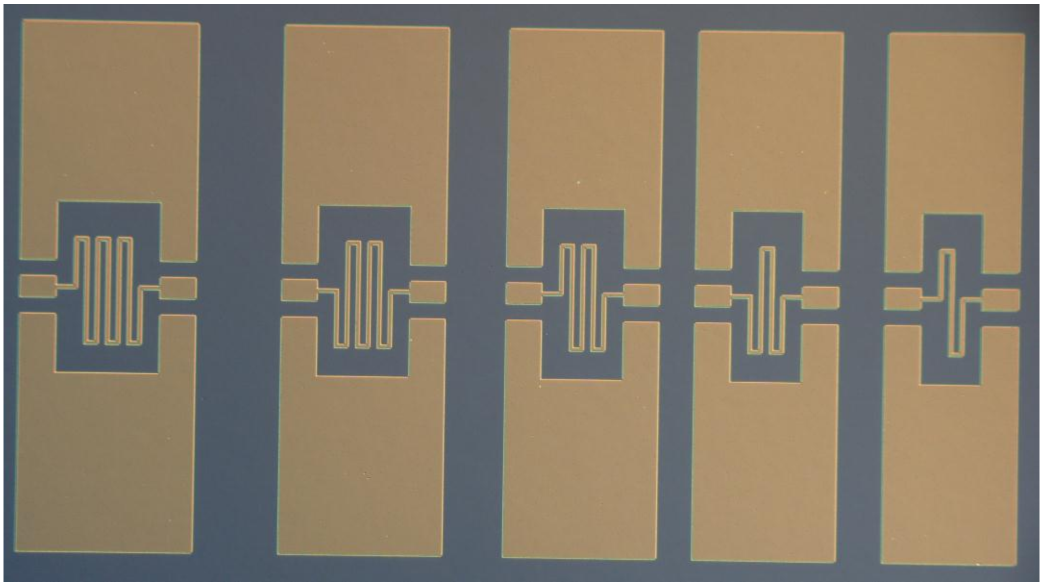

Figure 5.13: Meander line inductor with various turns.

Measured FMR frequency is 4.51GHz without the application of any external magnetic field. This has enabled the inductor application in the practical circuit boards where the large external magnet is unavailable. Inductance tunability of the implemented inductor is demonstrated by applying a DC current along the line. Applied DC current creates a magnetic field along the hard axis which changes the magnetic moment of the thin film and thus decreases the inductance of the line. Measured results show that the inductance density of the inductor can be varied 5% by applying 300mA DC current, larger inductance tunable is achievable by increasing the thickness of Permalloy film.

5.4.1 FABRICATION AND EXPERIMENT: MEANDER LINE INDUCTOR

The tunable meander line inductors with various turns were fabricated on top of high resistivity Si substrate as shown in Figure 5.13. The thickness of the metal was measured to be around 1µm. The width and the gap of the inductor trace was 10µm each.

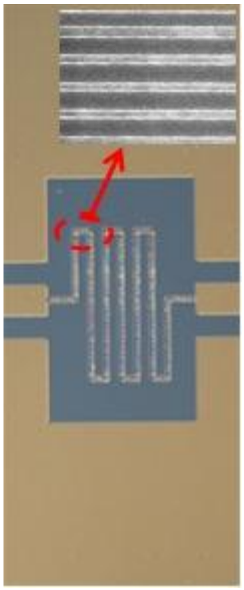

Figure 5.14: Meander line inductor with patterned Py.

The meander line inductor is kept in between the coplanar wave guide structure. This set up was made to characterize the devices with the help of the GSG probes.

The ferromagnetic thin film Permalloy was deposited on top of the meander line Inductors. Then the thin film was patterned to make it workable at very high frequency as

Table 5.6: Inductance, Capacitance, Impedance and Quarter Wave length of different meander line inductors

Structure	Inductance (nH/m)	Capacitance (pF/m)	Impedance (Ohm)	λ/4 @ 2.5GHz (mm)
Line 1	2565	.326	88.70	3.46
Line 2	2888	.323	94.55	3.27
Line 3	3090	.310	99.83	3.23
Line 4	3255	.300	104.16	3.20
Line 5	3396	.292	107.84	3.17

shown in Figure 5.14. The dimension of the Py bar is 10µm × 440nm while the thickness was 60nm. After the fabrication, the meander line inductors were characterized with the help of vector network analyzer, ZVA 67. The bias tee was used to apply DC current to change the value of the inductance. The same measurement set up has been used as the Py tunable slow wave structure in Chapter 3. At first, the S-parameters were measured for different meander line Inductor and the inductance value is extracted using the equations.

5.4.2 RESULTS AND DISCUSSIONS: MEANDER LINE INDUCTOR

The inductance value for various inductors with different turns is summarized in Table 5.6. It shows that when there was only one turn, the inductance per unit length was 2565nH/m which increased to 2888nH/m, 3090nH/m, 3255nH/m and 3396nH/m with the increase of the no. of turns. However, the change of the capacitance per unit length is very low due to the increase of turns. The value of characteristics impedance increased and the equivalent quarter wavelength decreased with the no. of turns as per transmission

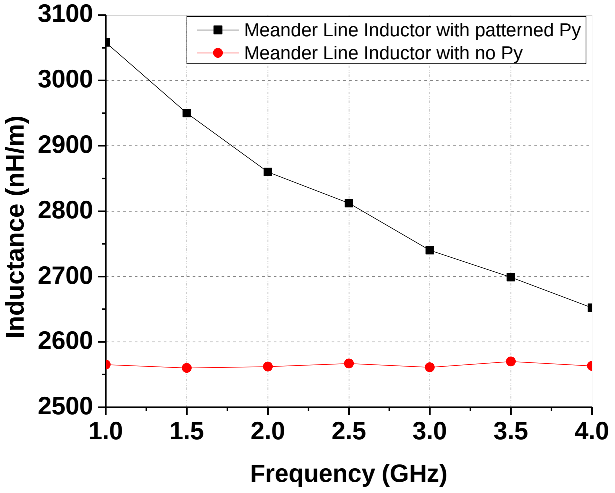

Figure 5.15: Measured inductance of meander line with and without Permalloy.

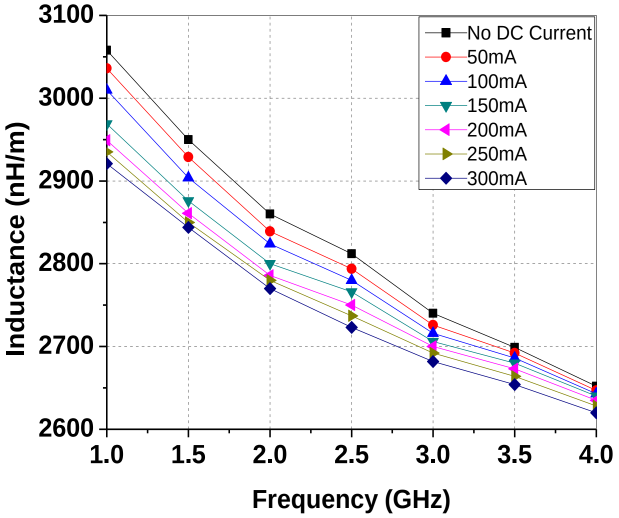

Figure 5.16: Measured inductance for different DC Current application.

line theory. Figure 5.15 shows the change of inductance value for different frequency which shows the inductance value increment from 2565nH/m to 3055nH/m at 1GHz for the introduction of patterned Py. As the FMR frequency was observed to be around 4.9GHz, the inductance value will be higher than 2565nH/m before that frequency. Figure 5.16 shows the change of the inductance for the application of different DC current. The DC current has two different effects: external magnetic field along the hard axis and Joule heating effect. Among them external magnetic field effect is dominant as the temperature increment is very low for this meander line. The anisotropy field is decreased as the magnetic moments deviates from the easy axis for external magnetic field. As the anisotropy field decreases, the inductance value and the FMR frequency is decreased as it is evident from the Figure 5.16.

5.4.3 CONCLUSIONS: MEANDER LINE INDUCTOR

A meander line Inductor using different turns has been designed, fabricated and characterized. It shows the increment of the inductance value with the no. of turns. The ferromagnetic thin film, Py has been deposited and patterned on top Inductors to increase the inductance value until the FMR frequency which was measured to be 4.9GHz. The inductors were tuned by DC current to achieve the desired inductance value.

5.5 SUMMARY

In this chapter, the ferro-magnetic thin film has been utilized for different radio frequency passive components. At first, the ferromagnetic resonance has been used to suppress the noise at very high frequency. The effect of the Py thin film patterning on inductance and FMR frequency has been analyzed to apply in radio frequency components. A tunable band pass filter and meander line inductor using patterned Py have been designed, fabricated and characterized. The loss due to the introduction of the thin film was less than 0.3dB for all the applications.

CHAPTER 6

CONCLUSIONS

6.1 SUMMARY OF CONTRIBUTIONS

Tunable slow wave structures have been designed, fabricated and characterized to demonstrate their promise applications on developing compact and multiband RF passive components for next generation wireless communication systems. A comparative and comprehensive study on the optimization of slow wave structures using microwave theory and techniques have been reported. Novel techniques using defected ground structure and different section length have been implemented along with the existed methods to reduce the size of a quarter wavelength transmission line by 43.47% and 37.54% with minimum loss.

For the first time, Permalloy has been successfully integrated to increase and electrical tune the inductance density value i.e. higher and tunable slow wave effect is achieved. Applications of ferro-magnetic thin film in radio frequency applications are restricted by the low ferro-magnetic resonance frequency and high eddy current loss, strategy by introducing shape anisotropy adopted in this dissertation has successfully addressed the issues. The nano-patterned Permalloy thin film has allowed the operation until 6.3GHz, increased the inductance density by 9.32% at 4GHz and demonstrated the frequency tuning of 4.75% (3.81GHz to 4GHz). The micro-patterned, 200nm thick Permalloy thin film has increased the inductance per unit length by 13% at 2GHz and shifted the center frequency up to 10% (1.80GHz to 2GHz). The application of the patterned Permalloy thin film kept the increment of insertion loss less than 0.3dB by reducing the eddy current through it.

The ferro-electric thin film, PZT has also been integrated with slow wave structures for large and electrical tunable capacitance density in the research. Py was grown with standard sol-gel method and selectively etched to demonstrate tunable slow wave structure. The integration of the ferro-electric thin film with coplanar waveguide slow wave structure had the difficulties of very low electric field linkage and lack of suitable non-conducting underneath the layer of PZT. The issues were solved by using interdigitated capacitor (IDC) structure while choosing SiO_2 as an intermediate layer. The PZT tunable slow wave structure increased the capacitance per unit length by 36% with the frequency tenability of 15% (1.75GHz to 2GHz).

In order to improve the slow wave effect further and to demonstrate the wider frequency tunability, both ferro-magnetic and ferro-electric thin films have been integrated simultaneously for the first time. The final tunable slow wave structure decreased the quarter wavelength size from 14.86mm to 3.98mm at 2GHz while the characteristics impedance was kept almost the same. The implemented structure can provide 90° phase shift for center frequency between 1.5GHz to 2GHz (i.e. 25% tunability) with suitable selection of DC current and voltage, this provides the most convenient and feasible tuning solution in a practical circuit board.

Various RF passive components have been developed with the slow wave structures integrated with ferro-magnetic (Py) and ferro-electric (PZT) thin films s. DC current tunable noise suppressor has been first developed which suppress electromagnetic noise from 4GHz to 6GHz. The suppression peak frequency is tunable with different dimensions of Py patterns and/or external DC current. A detailed experimental study on the inductance density and ferro-magnetic resonance frequency of Permalloy has been performed to evaluate its potential in radio frequency applications. A frequency agile bandpass filter has also been developed to investigate RF applications of the developed smart slow wave structures. The center frequency of the band pass filter has been tuned from 4GHz to 4.02GHz with 400mA DC current. Furthermore, a meander line inductor has been implemented with a tunable inductance per unit length from 2565nH/m to 3060nH/m with DC current.

All the concepts of the slow wave structures demonstrated in this dissertation are compatible with the other techniques available to reduce the size and multiband operations which opens the door of further improvement by efficient integration of different techniques. A smart unit cell (tunable slow wave structure) presented in this dissertation can be replicated in many passive components to solve the major concerns for upcoming wireless communication systems. Moreover, the application of the ferro-magnetic and ferro-electric thin film at high frequencies can be a breakthrough solution to next generation multiband, multifunctional applications.

6.2 FUTURE WORKS

Future work can be categorized as two ways: improvement of the existing methods and extension of the work into further diverse directions. For efficient operation of the slow wave structure, micro-electro-mechanical systems (MEMS) structures can be used to reduce the loss [147] while a thicker metal can reduce the conductor loss. The inductance tuning achieved by the ferro-magnetic thin film can be improved by two ways: to increase the FMR frequency and inductance density. The increase of net magnetic anisotropy can provide a solution to address both the issues which can be achieved by increasing the thickness of the ferro-magnetic material but eddy current loss will be increased. Several methods including the use of patterned thin film [117, 118, and 119] and multilayer thin film [96] can be used to decrease the eddy current loss as well as to increase FMR frequency. In case of the multilayer ferro-magnetic thin film, a thin non-conducting layer (for example: AlN) can be used to stop the flow of current from one layer to another. This multilayer thin film will also orient the magnetic moments along the axis of magnetization which will increase the magnetic anisotropy. The annealing of the film in presence of an external magnetic field can increase the magnetic anisotropy by orienting the magnetic moments along the easy axis [61]. Ni-Fe nanowires with small cross section areas can increase the natural FMR frequency [120, 121] also. As the saturation magnetization (M_s) value depends on the ferromagnetic material, researchers are now using different materials like CoNbZr, CoZrO, CoPdAlO, CoFeAlO, Fe [61, 57 and 122] etc. The CoFe can be a good candidate for ferromagnetic material as it has higher saturation magnetization than Permalloy. All the above mentioned methods like better material, annealing in presence of an external magnet during thin film growth, thicker material, multi-layer material with a thin non-conducting intermediate layer in between them and patterning with high aspect ratio can be used together to achieve a very high FMR frequency with wider frequency tuning range.

The thickness of the ferro-electric thin film will have to be increased to demonstrate the wider frequency tuning. A thicker layer of PZT could not be used in this dissertation due to the possibility of forming cracks as the sol-gel method used SiO_2 as an intermediate layer. The thickness of the PZT can be made much higher if it is grown by sputtering or molecular beam epitaxy (MBE) method. The PZT crystal formed by sol-gel method in this dissertation is polycrystalline with a preferred orientation. One of the main reasons of that crystal orientation is the lattice mismatching with the intermediate layer, SiO_2 which is amorphous by nature. An intermediate layer whose lattice structures closely matches with that of the PZT and which is close to single crystal can be used to address the issue: MgO can be a potential candidate for this purpose. Thus using a better method, a better intermediate layer and a thick ferro-magnetic material layer can result in a very high capacitance value as well as wider tuning range.

The tunable slow wave structures using both the ferro-magnetic and the ferro-electric thin film can be used as a unit cell in many passive components like branchline coupler, rat race coupler, filters, impedance matching networks, phase shifters etc. Simultaneous use of the ferro-magnetic and ferro-electric material can provide three advantages: fixed characteristics impedance, further reduced size and larger frequency tuning range. Tunable slow wave structure enabled passive components can be integrated in novel transceiver architectures [3-6] to further decrease the total size of the board area in next generation communication systems.

REFERENCES

[1] H. Tilmans, W. D. Raedt, and E. Beyne, “MEMS for Wireless Communica-tions: from RF MEMS Components to RF MEMS SIP,” *J. Micromech. Microeng.*, vol. 13, no. 4, June 2003.

[2] Nick. Pulsford, “Passive integration technology: Targeting small, accurate RF parts,” *RF design* 25.11, pp. 40-48, Nov 2002.

[3] G. Van De Walle, “Integration of passive components: An introduction,” *Philips j. of research*, vol. 51, no. 3, pp. 353–361, 1998.

[4] S. K. Bhattacharya and R. R. Tummala, “Integral passives for next generation of electronic packaging: application of epoxy/ceramic nanocomposites as integral capacitors,” *Microelectronics J.*, vol. 32, no. 1, pp 11-19, Jan 2001.

[5] Gray, Paul R., and Robert G. Meyer., “Future directions in silicon ICs for RF personal communications,” *IEEE Custom Integrated Circuits Conf.* Santa Clara, CA, pp 83–90, 1995.

[6] CT-C. Nguyen, “Transceiver front-end architectures using vibrating micromechanical signal processors,” *IEEE Topical Meeting on Silicon Monolithic Integrated Circuits in RF Systems*, pp. 23-32, 2001.

[7] G. Wang, W. Woods, H. Ding, and E. Mina, “Novel on-chip high performance slow wave structure using discontinuous microstrip lines and multi-layer ground

for compact millimeter wave applications," pp. 1606 – 1611, *59th Elec. Comp. Tech. Conf.*, 2009.

[8] W. Heinrich, J. Gerdes, F. J. Schmuckle, C. Rheinfelder, and K. Strohm, "Coplanar Passive Elements on Si Substrate for Frequencies up to 110 GHz," *IEEE Trans. Microwave Theory Tech.*, vol. 46, no. 5, May 1998.

[9] I-Hsiang Lin, C. Caloz, T. Itoh, "A branch-line coupler with two arbitrary operating frequencies using left-handed transmission lines," *Int. Microwave Symp. Digest*, 2003.

[10] Kwok-Keung M. Cheng, Member, and Fai-Leung Wong, "A Novel Approach to the Design and Implementation of Dual-Band Compact Planar 90° Branch-Line Coupler," *IEEE Trans. Microwave Theory Tech.*, vol. 52, no. 11, Nov. 2004.

[11] Ching-Wen Tang, Ming-Guang Chen, "Synthesizing Microstrip Branch-Line Couplers With Predetermined Compact Size and Bandwidth," *IEEE Trans. Microwave Theory Tech.*, vol. 55, no. 9, Sept. 2007.

[12] Kuo-Sheng Chin, Ken-Min Lin, Yen-Hsiu Wei, Tzu-Hao Tseng, and Yu-Jie Yang, "Compact Dual-Band Branch-Line and Rat-Race Couplers with Stepped-Impedance-Stub Lines," *IEEE Trans. Microwave Theory Tech.*, vol. 58, no. 5, May 2010.

[13] Jae-Ryong Lee, Jeong-Hoon Cho, and Sang-Won Yun, "New Compact Bandpass Filter Using Microstrip $\lambda/4$ Resonators with Open Stub Inverter," *IEEE Microw. Guided Wave Lett.*, vol. 10, no. 12, Dec. 2000.

[14] Jun-Seok Park, Jun-Sik Yun, and Dal Ahn, “A Design of the Novel Coupled-Line Bandpass Filter Using Defected Ground Structure With Wide Stopband Performance,” *IEEE Trans. Microwave Theory Tech*., vol. 50, no. 9, Sept. 2002.

[15] Min-Hang Weng, Hung-Wei Wu, and Yan-Kuin Su, “Compact and Low Loss Dual-Band Bandpass Filter Using Pseudo-Interdigital Stepped Impedance Resonators for WLANs,” *IEEE Microw. Compon. Lett.*, vol. 17, no. 03, Mar. 2007.

[16] Yue Ping Zhang and Mei Sun, “Dual-Band Microstrip Bandpass Filter Using Stepped-Impedance Resonators With New Coupling Schemes,” *IEEE Trans. Microwave Theory Tech*., vol. 54, no. 10, Oct. 2006.

[17] Xiu Yin Zhang, Jian-Xin Chen, Quan Xue, and Si-Min Li, “Dual-Band Bandpass Filters Using Stub-Loaded Resonators”, *IEEE Microw. Compon. Lett.*, vol. 17, no. 08, Aug. 2007.

[18] Girdhari Chaudhary, Yongchae Jeong, and Jongsik Lim, “Microstrip Line Negative Group Delay Filters for Microwave Circuits,” *IEEE Trans. Microwave Theory Tech*., vol. 62, no. 2, Feb. 2014.

[19] Y. J. Sung, C. S. Ahn, and Y.-S. Kim, “Size Reduction and Harmonic Suppression of Rat-Race Hybrid Coupler Using Defected Ground Structure,” *IEEE Microw. Compon. Lett.*, vol. 14, no. 01, Jan. 2004.

[20] Kwok-Keung M. Cheng, and Fai-Leung Wong, “A Novel Rat Race Coupler Design for Dual-Band Applications,” *IEEE Microw. Compon. Lett.*, vol. 15, no. 08, Aug 2005.

[21] Jianzhong Gu, and Xiaowei Sun, “Miniaturization and Harmonic Suppression Rat-Race Coupler Using C-SCMRC Resonators With Distributive Equivalent Circuit”, *IEEE Microw. Compon. Lett.*, vol. 15, no. 12, Dec. 2005.

[22] Chao-Hsiung Tseng, and Hsiang-Ju Chen, “Compact Rat-Race Coupler Using Shunt-Stub-Based Artificial Transmission Lines,” *IEEE Microw. Compon. Lett.*, vol. 18, no. 11, Nov. 2008.

[23] K.-K.M. Cheng and F.-L. Wong, “Dual-band rat-race coupler design using tri-section branch-line,” *Electron. Lett.*, vol. 43, no. 6, Mar. 2007.

[24] Raghu K. Settaluri, Senior Member, IEEE, G. Sundberg, A. Weisshaar, Senior Member, IEEE, and V. K. Tripathi, “Compact Folded Line Rat-Race Hybrid Couplers,” *IEEE Microw. Guided Wave Lett.*, vol. 10, no. 02, Feb. 2000.

[25] G. Wang, W. Woods, H. Ding, and E. Mina, “Novel low-cost on-chip CPW slow-wave structure for compact RF components and mm-wave applications,” *58th Elec. Comp. Tech. Conf.*, pp. 186 – 190, 2008.

[26] G. Wang, W. Woods, J. Xue, and E. Mina, “On-chip High Performance Slow Wave Transmission Lines using 3D Steps for Compact Millimeter Wave Applications,” *61st Elec. Comp. Tech. Conf.*, pp 1047 - 1051, 2011.

[27] S. Seki and H. Hasegawa, “Cross-tie slow-wave coplanar waveguide on semi-insulating GaAs substrate,” *Electron. Lett.*, vol. 17, no. 25, pp. 940-941, Dec. 1981.

[28] K. Wu and R. Vahldieck, “Hybrid-mode analysis of homogeneously and inhomogeneously doped low-loss slow-wave coplanar transmission line,” *IEEE Trans. Microwave Theory Tech.*, vol. 39, no. 8, pp. 1348-1360, 1991.

[29] James Sor, Yongxi Qian and Tatsuo Itoh, “A novel low loss slow-wave CPW periodic structure for filter applications,” *Int. Microwave Symp. Digest*, Phoenix, AZ, 2001.

[30] Kae-Oh Sun, Sung-Jin Ho, Chih-Chuan Yen, and Daniel van der Weide, “A compact branch-line coupler using discontinuous microstrip lines,” *IEEE Microw. Compon. Lett.*, vol. 15, no. 8, pp. 519-520, Aug. 2005.

[31] Kaixue Ma, Jianguo Ma, Manh Anh Do and Kiat Seng Yeo, “Experimentally investigating slow-wave transmission lines and filters based on conductor-backed CPW periodic cells,” *Int. Microwave Symp. Digest*, Long Beach, CA, June 2005.

[32] Vishnu Srivastava, Richard G. Carter, Member, IEEE, B. Ravinder, A. K. Sinha, and S. N. Joshi, “Design of Helix Slow-Wave Structures for High Efficiency TWTs,” *IEEE Trans. Electron Devices*, vol. 47, no. 12, Dec. 2000

[33] B. M. Farid Rahman, Ralu Divan, Hanqiao Zhang, Daniel Rosenmann, Yujia Peng, Xuehe Wang, and Guoan Wang, “High performance tunable slow wave elements enabled with nano-patterned permalloy thin film for compact radio frequency applications”, *J. of Appl. Physics*, vol. 115, no. 17A508, Jan. 2014.

[34] N. Q. Bolton, “Mobile Device RF Front-End TAM Analysis and Forecast,” *CS Mantech Conf.*, Indian Wells, CA, May 2011.

[35] 3GPP Standard TS 25.101 release 10, Available online: http://www.3gpp.org/ftp/specs/html-info/25101.htm.

[36] K. Sahota, “RF Front End Requirements for 3G and Beyond,” *IEEE Ultrasonics Symp.*, pp. 86-90, Oct. 11-14, 2010.

[37] K. Walsh and J. Johnson, “3G/4G Multimode Cellular Front End Challenges,” *RFMD White Paper*, 2009.

[38] Nick Cheng, and James P. Young, “Challenges and Requirements of Multimode Multiband Power Amplifiers for Mobile Applications,” *IEEE Comp. Semiconductor Integ. Circuit Symp.*, 2011.

[39] Bird Technology, RF Component Productcs, Parts no. 80-05-14, Available online: http://www.birdrf.com/Products/Components/Couplers/Multiband-Couplers/80-05-14_Multiband-Coupler.aspx#.U98aX_ldV8E

[40] The PCTEL's Medallion multiband antenna. Available online: http://www.rfwel.com/shop/Low-Profile-Multi-Band-Cellular-PCS-WiFi-WiMax-GPS-Antenna-RCVR.html

[41] F. F. He, K. Wu, W. Hong, L. Han, and X. Chen, “A low phasenoise VCO using an electronically tunable substrate integrated waveguide resonator,” *IEEE Trans. Microwave Theory Tech.*, vol. 58, no. 12, pp. 3452-3458, Oct. 2010.

[42] R. Brown and G. M. Rebeiz, “ A varactor-tuned RF filter,” *IEEE Trans. Microwave Theory Tech.*, vol. 48, no. 7, pp. 1157-1160, July 2000.

[43] W. Kim and S. W. Yun, “Varactor-tuned combline bandpass filter using step-impedance microstrip lines,” *IEEE Trans. Microw. Theory Techn.*, vol. 52, no. 4, pp. 1279-1283, Apr. 2004

[44] J. Nath, D. Ghosh, J. P. Maria, A. I. Kingon, W. Fathelbab, P. D. Franzon, and M. B. Steer, “An electronically tunable microstrip band-pass using thin-film barium-strontium-titanate(BST) varactors,” *IEEE Trans. Microw. Theory Techn.*, vol. 53, no. 9, pp. 2707-2712, Sept. 2005.

[45] Tombak, J. P. Maria, F. Ayguavives, J. Zhang, G. T. Stauf, A. I. Kingon, A. Mortazawi, “Tunable Barium Strontium Titanate Thin Film Capacitors for RF and Microwave Applications,” *IEEE Microw. Compon. Lett.*, vol. 12, no. 1, pp. 3-5, 2002.

[46] Y. Chun, J. S. Hong, P. Bao, T. J. Jackson, M. J. Lancaster, “BST-Varactor Tunable Dual-Mode Filter Using Variable Zc Transmission Line,” *IEEE Microw. Compon. Lett.*, vol. 18, no. 3, pp. 167-169, 2008.

[47] J. C. M. Hwang, and C. L. Goldsmith, “Robust RF MEMS switches and phase shifters for aerospace applications,” *Proc. IEEE Int. Symp. Radio-Frequency.*, pp. 245-248, Dec. 2009.

[48] G. M. Rebeiz, G. L. Tan, and J. S. Hayden, “RF MEMS Phase Shifters: Design and Applications,” *IEEE Microw. Mag.*, vol. 3, no. 2, pp. 72-81, June 2002.

[49] H. Garcia-Miquel, J. Carbonell, and J. Sanchez-DEhesa, “Left handed material based on amorphous ferromagnetic microwires by tunable DC current,” *Appl. Physics Lett.*, vol. 97, no. 09, Sept. 2010.

[50] L. V. Panina, M. Ipatov, V. Zhukova, A. Zhukov and J. Gonzalez, “Magnetic Field Effects in artificial dielectrics with arrays of magnetic wires at microwaves,” *J. Appl. Physics*, vol. 109, no. 05, Mar. 2011.

[51] M. Ipatov, V. Zhukov and J. Gonzalez, “Magnetoimpedance sensitive to dc bias current in amorphous microwires,” *Appl. Physics Lett.*, vol. 97, no. 25, Dec. 2010.

[52] S. Adhikari, Y. J. Ban, and K. Wu, “Magnetically tunable ferrite loaded substrate integrated waveguide cavity resonator,” *IEEE Microw. Compon. Lett.*, vol. 21, pp. 139-141, Mar. 2011.

[53] C. E. Fay, “Ferrite tuned resonant cavities,” *Proc. of IRE,* vol. 44, no. 10, pp. 1446-1449, Oct. 1956.

[54] H. Zhang, A. Hoffmann, R. Divan, and P. Wang, “Direct Current Effects on High-Frequency Properties of Patterned Permalloy Thin Films,” *IEEE Trans. Magn.,* vol. 45, no. 12, pp. 5296-5230, Nov. 2009.

[55] G. Wang, F. Rahman, T. Xia and H. Zhang, “Patterned Permalloy and Barium Strontium Titanate Thin Film Enabled Tunable Slow Wave Elements for Compact Multi-band RF Applications,” *IEEE Trans. Magn.*, vol. 49, no. 7, pp. 1-4, July 2013.

[56] M. Yamaguchi, M. Baba, K. Suezawa, T. Moizumi, K. Arai, A. Yaga, Y. Shimada, S. Tanabe, K. Itoh, “Improved RF Integrated Magnetic thin film Inductors by means of Micro Slits and Surface Palanarization Techniques,” *IEEE Trans. Magn.,* vol. 36, no. 5, Sept. 2000.

[57] J. Sohn , S. H. Han, M. Yamaguchi, S. H. Lim, “Tunable electromagnetic noise suppressor integrated with a magnetic thin film,” *Appl. Phys. Lett.,* vol. 89, no. 10, Sept. 2006.

[58] B. K. Kuanr, R. Marson, S. R. Mishra, A. V. Kuanr, R. E. Camley, and Z. J. Celinski, “Gigahertz frequency tunable noise suppressor using nickel nanorod arrays and Permalloy films,” *J. Appl. Phys.*, vol. 105, no. 07, 2009.

[59] M. Yamaguchi, Ki. H. Kim, T. Kuribara, and K. I. Arai, “Thin-Film RF Noise Suppressor Integrated in a Transmission Line,” *IEEE Trans. Magn.*, vol. 38, no. 5, Sept. 2002.

[60] K. H. Kim, S. Ohnuma, and M. Yamaguchi, “RF Integrated Noise Suppressor Using Soft Magnetic Films,” *IEEE Trans. Magn.*, vol. 40, no. 4, July 2004.

[61] K. H Kim, M. Yamaguchi, and K. I. Arai, “Effect of radio-frequency noise suppression on the coplanar transmission line using soft magnetic thin films,” J. Appl. Phys., vol. 93, no. 10, May 2003.

[62] K. H. Kim, H. Orikasa, T. Kyotani, and M. Yamaguchi, “RF Noise Suppression Using Carbon-Coated Permalloy Nanorod Arrays,” *IEEE Trans. Magn.,* vol. 41, no. 10, Oct 2005.

[63] K.H. Kim, J. Yu, S. B. Lee, S. K. Lee, Y. H. Choa, S. T. O, and J. Kim, “RF Conduction In-Line Noise Suppression Effects for Fe and NiFe Magnetic Nanocomposite,” *IEEE Trans. Magn.*, vol. 44, no. 11, Nov. 2008.

[64] James Salvia, James A. Bain, and C. Patrick Yue, “Tunable on-chip inductors up to 5 GHz using patterned permalloy laminations,” *IEEE Int. Elec. Device Meet.,* Dec 2005.

[65] Yan Zhuang, B. Rejaei, E. Boellaard, M. Vroubel, and J. N. Burghartz, “Integrated Solenoid Inductors With Patterned, Sputter-Deposited Cr/Fe10Co90/Cr Ferromagnetic Cores,” *IEEE Elec. Device Lett.*, vol. 24, no. 4, April 2003.

[66] Luca Daniel, Charles R. Sullivan, and Seth R. Sanders, “Design of Microfabricated Inductors,” *IEEE Trans on Power Elec.*, vol. 14, no. 4, July 1999.

[67] Marina Vroubel, Yan Zhuang, Behzad Rejaei, and Joachim N. Burghartz, “Integrated Tunable Magnetic RF Inductor,” *IEEE Elec. Device Lett.,* vol. 25, no. 12, Dec 2004.

[68] E. Salahun, France Brest, G. Tanne, P. Queffelec, P. Gelin, “Ferromagnetic composite-based and magnetically-tunable microwave devices,” *Int. Microwave Symp. Digest*, June 2002.

[69] A. B. Ustinov, V. S. Tiberkevich, G. Srinivasan, A. N. Slavin, A. A. Semenov, S. F. Karmanenko, B. A. Kalinikos, J. V. Mantese, and R. Ramer, “Electric field tunable ferrite-ferroelectric hybrid wave microwave resonators: Experiment and theory,” *J. Appl. Phys.*, vol. 100, no. 09, 2006.

[70] Guoan Wang, Farid Rahman, Tian Xia, and Hanqiao Zhang, “Patterned Permalloy and Barium Strontium Titanate Thin Film Enabled Tunable Slow Wave Elements for Compact Multi-Band RF Applications,” *IEEE Trans. Magn.*, vol. 49, no. 7, July 2013.

[71] R. D. Gomez, T. V. Luu, and A. O. Pak, K. J. Kirk and J. N. Chapman, “Domain conFigureurations of nanostructured Permalloy elements,” *J. Appl. Phys.*, vol 85, no 8, April 1999.

[72] Xiaobin Zhu, P. Grutter, V. Metlushko, “Magnetic force microscopy study of electron-beam-patterned soft permalloy particles: Technique and magnetization behavior”, *Physical Review B*, 66, 024423, July 2002.

[73] G. Gubbiotti, L. Albini, G. Carlotti, M. De Crescenzi, E. Di Fabrizio, A. Gerardino, O. Donzelli F. Nizzoli, H. Koo and R. D. Gomez, “Finite size effects in patterned magnetic permalloy films,” J. Appl. Phys., vol. 87, no. 9, May 2000.

[74] K. Entesari, G. M. Rebeiz, “A differential 4-bit 6.5-10-GHz RF MEMS tunable filter,” *IEEE Trans. Microwave Theory Tech*., vol.53, no.3, pp.1103-1110, March 2005

[75] Yang Guo-Min, Wu Jing, Lou Jing, Liu Ming, N.X. Sun, "Low-Loss Magnetically Tunable Bandpass Filters With YIG Films," *IEEE Trans. Magn.*, vol. 49, no. 9, pp. 5063-5068, Sept. 2013.

[76] Chaudhary, G.; Yongchae Jeong; Jongsik Lim, "Dual-Band Bandpass Filter With Independently Tunable Center Frequencies and Bandwidths," *IEEE Trans. Microwave Theory Tech*., vol.61, no.1, pp.107-116, Jan. 2013

[77] Byung-Wook Kim; Sang-Won Yun, "Varactor-tuned combline bandpass filter using step-impedance microstrip lines," *IEEE Trans. Microwave Theory Tech*., vol. 52, no. 4, pp.1279-1283, April 2004

[78] J. Nath, D. Ghosh, JP. Maria, "An electronically tunable microstrip bandpass filter using thin-film Barium-Strontium-Titanate (BST) varactors," *IEEE Trans. Microwave Theory Tech.* , vol. 53, no. 9, pp.2707-2712, Sept. 2005

[79] Tae-Yeoul Yun, Kai Chang, "Piezoelectric-transducer-controlled tunable microwave circuits," *IEEE Trans. Microwave Theory Tech*., vol.50, no.5, pp.1303-1310, May 2002

[80] B. Liu, F. Wei, X. Shi, "Reconfigurable bandpass filter based on net-type stepped-impedance resonator," *Electron. Lett.* , vol.46, no.22, pp.1506-1507, Oct. 2010.

[81] Chong H. Ahn, and Mark G. Allen, "Micro machined Planar Inductors on Silicon Wafers for MEMS Applications," *IEEE Trans. Ind. Electr.*, vol. 45, no. 6, Dec 1998.

[82] David Redinger, Steve Molesa, Shong Yin, Rouin Farschi, and Vivek Subramanian, “An Ink-Jet-Deposited Passive Component Process for RFID”, *IEEE Trans. Electron Devices*, vol. 51, no. 12, Dec 2004.

[83] A. C. Reyes, S. M. El-Ghazaly, S. J. Dorn, M. Dydyk, D. K. Schroder, and H. Patterson, “Coplanar waveguides and microwave inductors on silicon substrates,” *IEEE Trans. Microwave Theory Tech*., vol. 43, pp. 2016–2022, Sept. 1995.

[84] D. Lovelace, N. Camilleri, and G. Kannell, “Silicon MMIC inductor modeling for high volume, low cost applications,” *Microwave J.*, pp. 60–68, Aug. 1994.

[85] M. Hirano, Y. Imai, I. Toyoda, K. Nishikawa, M. Tokumitsu, and K. Asai, “Three-dimensional passive elements for compact GaAs MMIC’s,” *IEICE Trans. Electron.*, vol. E76-c, no. 6, pp. 961–967, 1993.

[86] O. Oshiro, H. Tsujimoto, and K. Shirae, “High frequency characteristics of a planar inductor and a magnetic coupling control device,” IEEE Transl. J. Magn. Japan, vol. 6, no. 5, pp. 436–442, Mar. 1993.

[87] M. Yamaguchi, M. Matsumoto, H. Ohzeki, and K. I. Arai, “Analysis of the inductance and the stray capacitance of the dry-etched micro inductors,” *IEEE Trans. Magn.*, vol. 27, pp. 5274–5276, Nov. 1991.

[88] Yong-Jun Kim and Mark G. Allen, “Surface Micromachined Solenoid Inductors for High Frequency Applications”, *IEEE Trans. Components, Packaging, Manf. Tech.*, Part C, vol. 21, no. 1, Jan 1998.

[89] David M. Pozar, *Microwave Engineering*, 3rd Edition, John Wiley & Sons, Inc.

[90] Rainee N Simons, *Coplanar Waveguide Circuits, Components, and Systems*, John Wiley & Sons, Inc.

[91] William R. Eisenstadt, and Yungseon Eo, “S-Parameter-Based IC Interconnect Transmission Line Characterization,” *IEEE Trans on Compnt., Hybrids, and Manf. Tech.*, vol 15, no 4, Aug 1992.

[92] Bruce M. Moskowitz, *Hitchhiker's Guide to Magnetism*, Environmental Magnetism Workshop, Institute for Rock Magnetism, University of Minnesota; June 1991. Available on-line: http://www.irm.umn.edu/hg2m/hg2m_index.html

[93] L. Tauxe, S.K. Banerjee, R.F. Butler, and van der Voo, *Essentials of Paleomagnetism*, 2nd Web Edition, 2012, Available online: http://magician.ucsd.edu/essentials/WebBook.html

[94] Tawab Dastagir, Wei Xu, Saurabh Sinha, Hao Wu, Yu Cao, and Hongbin Yua, “Tuning the permeability of permalloy films for on-chip inductor applications,” Appl. Phys. Lett. vol. 97, no. 16, 2010.

[95] G.W. Elmen, H. D. Arnold, “Permalloy, A New Magnetic Material of Very High Permeability,” *Bell System Tech. J.*, pp 101–111, July 1923.

[96] B. Kuanr, R. E. Camley, and Z. Celinski, “Narrowing of the frequency-linewidth in structured magnetic strips: Experiment and theory”, *Appl. Phys. Lett*, vol 87, no. 01, 2005.

[97] Amikam Aharoni, “Demagnetizing factors for rectangular ferromagnetic prisms,” J. Appl. Phys., vol 83, no 6, March 1998.

[98] T. Korn, M. Kerekes, U. Ebels, D. Stanescu, and P. Xavier, “Pumping-Field-Induced Dynamic Effects in Micron-Sized Permalloy Lines and Their Influence on HF Filter applications,” *IEEE Trans. Magn.*, vol. 41, no. 10, Oct. 2005.

[99] T. J. Silva, C. S. Lee, T. M. Crawford, and C. T. Rogers, “Inductive measurement of ultrafast magnetization dynamics in thin-film Permalloy,” *J. Appl. Phys.*, vol. 85, pp. 7849–7862, Jun. 1999.

[100] A. Yamaguchi and K. Motoi, “Broadband ferromagnetic resonance of $Ni_{81}Fe_{19}$ wires using a rectifying effect” , *Phys. Rev. B 78, 104401,* Sept. 2008.

[101] K. Kim, J. Lee, S. Choe, and K. Shin, “Joule heating in ferromagnetic nanowires: Prediction and observation,” *Appl. Phys. Lett.*, vol. 92, p.192509, May 2008.

[102] R. H. Koch, G. Grinstein, G. A. Keefe, Y. Lu, P. L. Trouilloud, W. J. Gallagher, and S. S. P. Parkin, “Thermally assisted magnetization reversal in submicron-sized magnetic thin films,” *Phys. Rev. Lett.*, vol. 84, pp. 5419–5422, June 2000.

[103] D. Ilgaz, M. Kläui, L. Heyne, O. Boulle, F. Zinser, S. Krzyk, M. Fonin, U. Rüdiger, D. Backes, and L. J. Heyderman, “Selective domain wall depinning by localized oersted fields and Joule heating,” *Appl. Phys. Lett.*, vol. 93, p. 132503, Oct. 2008.

[104] Werner Känzig, *Ferroelectrics and Antiferroelectrics*, Academic Press. p. 5. ISBN 0-12-607704-5.

[105] M. Lines, A. Glass, *Principles and applications of ferroelectrics and related materials*, Clarendon Press, Oxford. ISBN 0-19-851286-4.

[106] Adnan Mousharraf and Rubayyat Mahbub Turjo, “The World of Ferroelectric Ceramics”, August 2012. Available online:

http://www.ceramicindustry.com/articles/92711-the-world-of-ferroelectric-ceramics

[107] J. Rouquette, J. Haines, V. Bornand, M. Pintard, M, Papet, “Pressure tuning of the morphotropic phase boundary in piezoelectric lead zirconate titanate.” *Physical Review B 70 (1): 014108.*

[108] Weiguo Liu, Bin Jiang, and Weiguang Zhu, “Self-biased dielectric bolometer from epitaxially grown PbZrTiO3 and lanthanum-doped PbZrTiO3 multilayered thin films”, Appl. Phys. Lett. vol. 77, no. 7, Aug 2000.

[109] B. T. Liu, J. W. Zhao, X. H. Li, Y. Zhou, F. Bian, X. Y. Wang, Q. X. Zhao, Y. L. Wang, Q. L. Guo, L. X. Wang, and X. Y. Zhang, “Enhanced dielectric constant and fatigue-resistance of PbZr0.4Ti0.6O3 capacitor with magnetic intermetallic FePt top electrode,” *Appl. Phys. Lett., vol.* 96, no. 25, 2010.

[110] F. Calamea_ and P. Muralt, “Growth and properties of gradient free sol-gel lead zirconate Titanate thin films,” *Appl. Phys. Lett.*, vol. 90, no. 06, 2007.

[111] Chang Jung Kim, Dae Sung Yoon, Zhong Tao Jiang, Kwangsoo No, “Investigation of the drying temperature dependence of the orientation in sol–gel processed PZT thin films”, *J. of Mat. Science*, vol. 32, pp. 1213-1219, 1997.

[112] Kelu Zheng, Jian Lu and Jiaru Chu, “A Novel Wet Etching Process of Pb(Zr,Ti)O3 Thin Films for Applications in Microelectromechanical System”, *Japanese J. Appl. Phys.,* vol. 43, no. 6B, pp. 3934–3937, 2004.

[113] K. H. Kim, M. Yamaguchi, S. Ikeda, and K. I. Arai, “Modeling for RF Noise Suppressor Using a Magnetic Film on Coplanar Transmission Line,” *IEEE Trans. Magn.*, vol. 39, no. 5, Sep. 2003.

[114] Shau-Gang Mao; Ming-Yi Chen, “Propagation Characteristics of Finite-Width Conductor-Backed Coplanar Waveguides With Periodic Electromagnetic Bandgap Cells,” *IEEE Trans. Microwave Theory Tech*., vol.50, no.11, pp. 2624-2628, Nov 2002.

[115] Shau-Gang Mao; Yu-Zhi Chueh, “Coplanar Waveguide Bandpass Filters With Compact Size and Wide Spurious-Free Stopband Using Electromagnetic Bandgap Resonators,” *IEEE Microw. Compon. Lett.*, vol.17, no.3, pp.181-183, March 2007.

[116] J. K A Everard, K.-K.M. Cheng, “A new technique for the quasi-TEM analysis of conductor-backed coplanar waveguide structures,” *IEEE Trans. Microwave Theory Tech*. vol.41, no.9, pp.1568-1573, Sept. 1993.

[117] Y. Khivintsev, B. Kuanr, I. Harward, R. E. Camley, and Z. Celinski, “Iron-based microstrip band-stop filters at higher microwave frequency range: Design optimization using shape anisotropy,” *J. Appl. Phys.*, vol. 99, p. 08P512, 2006.

[118] M. Vroubel, Y. Zhuang, B. Rejaei, J. Burghartz, A. Crawford, and S. X. Wang, “Calculation of Shape Anisotropy for Micropatterned Thin Fe–Ni Films for On-Chip RF Applications”, *IEEE Trans. Magn.,* vol 40, no. 4, pp. 2835–2837, Jul. 2004.

[119] B. Kuanr, R. Camley, and Z. Celinski, “Relaxation in epitaxial Fe films measured by ferromagnetic resonance”, *IEEE Trans. Magn.*, vol. 40, no. 4, pp. 2841–2843, Jul. 2004.

[120] A. Saib, M. Darques, L. Piraux, D. Janvier, and I. Huynen," An Unbiased Integrated Microstrip Circulator Based on Magnetic Nanowired Substrate", *IEEE Trans. Microwave Theory Tech*., vol. 53, no. 6, pp. 2043–2049, 2005.

[121] G. Goglio, S. Pignard, A. Radulescu, L. Piraux, I. Huynen, and A. Vorst, "Microwave properties of metallic nanowires," *Appl. Phys. Lett.*, vol. 75, no. 12, pp. 1769–1771, 1999.

[122] Y. W. Zhao, X. K. Zhang, J. Q. Xiao, "Submicrometer Laminated Fe/SiO2 Soft Magnetic Composites—An Effective Route to Materials for High-Frequency Applications," *Advanced Materials*, vol. 17, no. 7, pages 915–918, April 2005.

[123] DVDO, 60 GHz HDMI 1.4a compatible, 1080p, 3D and 7.1 high-resolution audio streams and CEC supported. Available online: http://www.portablehifi.com/dvdo-air-wireless-hd-connection-

[124] Bosch to launch 77GHz rear end radar. Available online: http://www.automotiveworld.com/analysis/96757-germany-bosch-to-launch-77ghz-rear-end-radar/

[125] SUMATRA – millimeter wave SAR for UAV-based surveillance. Available online: http://www.fhr.fraunhofer.de/en/businessunits/Air-and-space-based-radar-systems/SUMATRA-millimeter-wave-SAR-for-UAV-based-surveillance.html

[126] GigaBeam E-beam wireless point-to-point communications. Available online: http://web.mst.edu/~mobildat/E-band%20Frequencies/index.html

[127] Agile-Link, High Speed Wireless Data Acquisition SystemWireless sensor. Available online: http://liftcells.com.au/cgi-

bin/search.cgi?count=5&next=true&category=MICROSTRAIN&sub_category=Sensors

[128] Advanced Extreme High Frequency Team. Available online: http://www.lockheedmartin.com/us/products/advanced-extremely-high-frequency--aehf-.html

[129] Micro-pipe direct 2.4GHz transceiver board. Available online: http://www.microchipdirect.com/productsearch.aspx?Keywords=explorer+16

[130] Hitchhiker's Guide To Magnetism. Available online: http://www.irm.umn.edu/hg2m/hg2m_index.html

[131] Girdhari Chaudhary, Heungjae Choi, Yongchae Jeong, Jongsik Lim, , Dongsu Kim, and Jun-Chul Kim , "Design of Dual-Band Bandpass Filter Using DGS With Controllable Second Passband," IEEE Microw. Compon. Lett., vol. 21, no. 11, Nov. 2011.

[132] J A Souza and R F Jardim, "Electrical transport in disordered and ordered magnetic domains under pressures and magnetic fields*," J. Physics D.* vol. 42 , no. 3, Feb 2009.

[133] Magnetic permeability and the B/H curve. Available online: http://www.expertsmind.com/questions/magnetic-permeability-and-the-bh-curve-3019581.aspx.

[134] D. S. Gardner, A. M. Crawford, and S. X. Wang, "High frequency (GHz) and low resistance integrated inductors using magnetic materials," *Proc. IEEE Int. Interconnect Tech. Conf.*, pp. 101–103, 2001.

[135] B. Viala, S. Couderc, A. S. Royet, P. Ancey, and G. Bouche, “Bidirectional ferromagnetic spiral inductors using single deposition,” *IEEE Trans. Magn.*, vol. 41, pp. 3544–3549, 2005.

[136] A. M. Crawford, D. Gardner, and S. X. Wang, “High-frequency microinductors with amorphous magnetic ground planes,” *IEEE Trans. Magn.*, vol. 38, pp. 3168–3170, 2002.

[137] M. Yamaguchi, K. Suezawa, K. I. Arai, Y. Takahashi, S. Kikuchi, Y. Shimada, W. D. Li, S. Tanabe, and K. Ito, “Microfabrication and characteristics of magnetic thin-film inductors in the ultrahigh frequency region,” *J.Appl. Phys.*, vol. 85, pp. 7919–7922, 1999.

[138] M.Yamaguchi, M. Baba, and K. I. Arai, “Sandwich-type ferromagnetic RF integrated inductor,” *IEEE Trans. Microw. Theory Tech.*, vol. 49, pp. 2331–2335, 2001.

[139] D. S. Gardner, G. Schrom, P. Hazucha, F. Paillet, T. Karnik, S. Borkar, R. Hallstein, T. Dambrauskas, C. Hill, C. Linde, W. Worwag, R. Baresel, and S. Muthukumar, “Integrated on-chip inductors using magnetic material (invited),” *J. Appl. Phys.*, vol. 103, no. 04, pp. 07E927-1–07E927-6, 2008.

[140] D. S. Gardner, G. Schrom, P. Hazucha, F. Paillet, T. Karnik, S. Borkar, J. Saulters, J. Owens, and J.Wetzel, “Integrated on-chip inductors with magnetic films,” *Int. Electron Devices Meeting*, pp. 1–4, 2006.

[141] D. S. Gardner, G. Schrom, P. Hazucha, F. Paillet, T. Karnik, and S. Borkar, “Integrated on-chip inductors with magnetic films,” *IEEE Trans. Magn.*, vol. 43, no. 6, pp. 2615–2617, June 2007.

[142] Charles Sullivan, Seth R. Sanders, “Design of microfabricated transformers and inductors for High Frequency Power Conversion,” *IEEE Trans. Power Electro.*, vol. 11, no. 2, March 1996.

[143] James M. Daughton, Jack S. T. Huang, “Magnetoresistive memory including thin film storage cells having tapered ends,” *Patent No. US4731757 A*, March 1988.

[144] Jiin-Chuan Wu, Henry L. Stadler, Romney R. Katti, “High speed magneto-resistive random access memory,” *Patent No. US5173873 A*, Dec 1982.

[145] N. Setter, D. Damjanovic, L. Eng, G. Fox, S. Gevorgian, S. Hong, A. Kingon, H. Kohlstedt, N. Y. Park, G. B. Stephenson, I. Stolitchnov, A. K. Taganstev, D. V. Taylor, T. Yamada, and S. Streiffer, “Ferroelectric thin films: Review of materials, properties, and applications,” J. Appl. Phys., vol. 100, no. 05, 2006.

[146] Z. Popovic, and B. Popovic, *Introductory Electromagnetics*, Prentice-Hall, 1999.

[147] Hong-Teuk, Jae-Hyoung Park, Yong-Kweon Kim, and Youngwoo Kwon, “V-band low-loss and low-voltage distributed MEMS digital phase shifter using metal-air-metal capacitors,” Int. Microw. Symp., vol. 1, pp. 341-344. IEEE, 2002.